Technische Universität München

Max-Planck-Institut für Quantenoptik

Entanglement and Correlations in Cold Atomic Systems

Markus Popp

Vollständiger Abdruck der von der Fakultät für Physik
der Technischen Universität München
zur Erlangung des akademischen Grades eines

Doktors der Naturwissenschaften (Dr. rer. nat.)

genehmigten Dissertation.

Vorsitzender : Univ.-Prof. Dr. Dr. h.c. A. Laubereau

Prüfer der Dissertation : 1. Hon.-Prof. I. Cirac, Ph. D.
2. Univ.-Prof. Dr. M. Kleber

Die Dissertation wurde am 18.07.2006 bei der
Technischen Universität München eingereicht und
durch die Fakultät für Physik am 19.09.2006 angenommen.

Abstract

This thesis is devoted to the theoretical characterization and generation of strongly correlated many-body states from the perspective of quantum information theory. We first study the entanglement properties of general many-body states and define a new measure for multipartite entanglement, the "Localizable Entanglement (LE)". It quantifies the maximal entanglement that can be localized, on average, between two parties by performing local measurements on the other parties. This measure provides knowledge of the "entanglement length", which is of particular importance in the context of quantum repeaters for long-distance quantum communication. We prove upper and lower bounds on LE in terms of two-body correlation functions and develop a method for the numerical computation of LE in one-dimensional spin systems. We analyze the localizable entanglement in various spin systems and observe characteristic features for a quantum phase transition such as a diverging entanglement length.

In the second part of the thesis we focus on a specific many-body system: ultra-cold atoms in an optical lattice. This system is a promising candidate for the first physical realization of a "quantum simulator", but the temperature in current experiments is still too high. We propose, analyze and compare several schemes to cool the atoms close to the ground state of the strong interaction regime. In particular, we devise an algorithmic cooling protocol that combines occupation number filtering with spin-dependent lattice shifts. In addition, we propose two different physical realizations of filtering and also design protocols that generate an ensemble of quantum registers for quantum computation.

In the third part we propose how to create entanglement in small atomic clouds by deforming and rotating the harmonic trapping potential. The resulting states are entangled in their motional degrees of freedom and can be identified with strongly correlated fractional quantum Hall states. For the case of two, three and four atoms we show how to adiabatically transform the unentangled ground state into the desired entangled state. We further discuss characteristic features of these states and propose how to create and detect them experimentally using an optical lattice setup.

Contents

Chapter 1

Introduction

Entanglement is one of the deepest departures of quantum mechanics from classical physics. It plays a key role for quantum information tasks, such as teleportation [1], quantum communication [2] and quantum computation [3]. In recent years major achievements in the experimental generation of entanglement have been made. For instance, in quantum optical systems entanglement of up to eight ions [4, 5] or five photons [6] has been demonstrated. Of special importance are also strongly correlated many-body states. First of all they provide a natural resource for entanglement. Secondly, highly entangled many-body states can be used to perform measurement based quantum computation [7, 8]. Thirdly, the study of many-body entanglement can provide significant physical insight in strong correlation effects such as quantum phase transitions. Hence, it is of central interest to get a better understanding of multipartite entanglement. In this thesis we define a novel measure of multipartite entanglement, the "Localizable entanglement (LE)". It allows one to deduce a characteristic distance, the "entanglement length", up to which bipartite entanglement can be extracted from the system by local operations. Knowledge of this length scale is of particular importance in the context of quantum repeaters for long-distance quantum communication.

We further consider a very important many-body system in the field of quantum information theory: ultra cold atoms in optical lattices. This system is a promising candidate for the first physical realization of a "quantum simulator" that simulates the quantum dynamics of other many-body systems [9]. With just 40 atoms in an optical lattice one could perform quantum simulations that are impossible with ordinary computers. In contrast, the efficient solution of other practical problems on a quantum computer (such as the factorization problem) would require on the order of 10,000 atoms to beat a classical computer. The major obstacle that hinders the implementation of a quantum simulator in current experiments is temperature. In this thesis we propose, analyze and compare several cooling schemes for atoms in optical lattices. Our theory predicts that we can cool the system close to the ground state of the strong interaction regime.

We also propose how to generate a novel class of entangled states in atomic systems, in which the atoms are entangled in their motional degrees of freedom. These states are equivalent to strongly correlated fractional quantum Hall (FQH) states. FQH states may exhibit anyons, which are neither bosons nor fermions but show fractional quantum statistics. Non-abelian anyons are especially interesting from the perspective of topological quantum computation [10].

In the following we describe the different parts of this thesis in more detail. The first part is devoted to the entanglement properties of general many-body systems. The usual approach is to characterize multipartite entanglement in terms of bipartite entanglement. One possibility is to study the entanglement between two separate particles after tracing out the rest of the system. This can formally be done by computing the entanglement of formation [11, 12] of the reduced density matrix, which quantifies the entanglement cost to produce this bipartite state. For spin systems it has been shown that this quantity can exhibit characteristic features at a quantum phase transition and also that the entanglement decays very rapidly with the distance of the two spins [13, 14]. Another possibility is to study the von-Neumann entropy of a subsystem, which for pure states quantifies the entanglement with the rest of the system. The entropy in one-dimensional spin systems has been studied extensively in recent years. It is now believed that the entropy diverges logarithmically with the block size if the system is critical, and that the entanglement growth is connected to the universality class of the underlying theory [15, 16].
However, both approaches are not very well suited for defining an "entanglement length", up to which bipartite entanglement can be extracted from the system. This length scale could serve as a figure of merit for a "quantum repeater" [17], which is a way of distributing entanglement over long distances by applying local operations at the nodes of a quantum network.

Motivated by the quantum repeater concept we propose a novel measure for multi-particle entanglement, which we have termed "Localizable Entanglement" (LE). It is defined as the maximum entanglement that can be localized, on average, between two particles by performing local measurements on all other particles. This definition naturally leads to notions like "entanglement length" and "entanglement fluctuations". We further prove for pure qubit and qutrit states that the LE is lower bounded by the maximum (connected) two-point correlation function. With a study of ground state entanglement in various spin-1/2 models we demonstrate that this bound is typically tight. We also develop a numerical method that allows us to compute the LE in ground states, thermal states and time-evolved states in one-dimensional spin systems with large number of spins. Applying this method to ground states we find that the entanglement fluctuations (as defined by LE) as well as LE itself exhibit characteristic features at a quantum phase transition. For instance, one observes a discontinuity in the first derivative of LE at a Kosterlitz-Thouless transition [18]. For the ground state of the spin-1 Heisenberg antiferromagnet one obtains a very counter-intuitive result: the entanglement length is infinite but the two-body correlation length is finite.

After the study of entanglement in rather general many-body systems, we focus in the remainder of this thesis on a specific system: ultra cold atoms in an optical lattice. With the realization of Bose-Einstein condensation (BEC) in 1995 atomic research in atomic physics has reached a new dimension. Many of the early experiments on BECs can be well explained with mean field theory, in which all atoms behave exactly the same. The new challenge is the strong-interaction regime. The interactions between atoms can be enhanced by tuning the magnetic field through a Feshbach resonance, at which the scattering length diverges. In a series of remarkable experiments with fermionic atoms this method has been used to observe the crossover from a BEC of molecules to the BCS regime, in which Cooper pairs are formed [19, 20, 21, 22, 23]. An alternative way to reach the strong-interaction regime is to load and trap cold atoms in an optical lattice potential[1]. By increasing the intensity of the lattice laser beams one can decrease the kinetic energy of the atoms until the interactions dominate the dynamics. The systems then undergoes a quantum phase transition from a superfluid to a Mott insulator. This phenomenon was first observed by Greiner et al. [24] in 2002. In the past years several groups managed to load bosonic or fermionic atoms in optical lattices and reach the strong interaction regime [24, 25, 26, 27, 28, 29, 30, 31, 32]. This system constitutes one of the very few quantum systems that can be controlled and manipulated on the single quantum level, while at the same time avoiding unwanted interaction with the environment causing decoherence. In addition, it provides an unprecedented degree of flexibility. The interaction can be tuned from repulsive to attractive, one can generate lattices with different geometries, use several internal states of

---

[1] The optical lattice is formed by three orthogonal pairs of counterpropagating laser fields that are not resonant with an atomic transition. Due to the ac-Stark shift the atoms are trapped in the minima of the three-dimensional lattice potential.

the atoms, and mix fermions with bosons. Therefore it has been proposed to use atoms in optical lattices in order to simulate the quantum dynamics of various kinds of Hubbard Hamiltonians [33, 34, 35, 36, 37, 38, 39, 40, 41, 42]. This may help to understand strong correlation effects that have been observed or predicted in solid-state systems. For instance, the study of fermions with repulsive interactions in two dimensions might shed some light on the origin of high temperature superconductivity. Also the physical implementation of a "Feynman quantum simulator" has been put forward [9]. This has to be distinguished from the "analogue" quantum simulator that is provided naturally by the Hubbard Hamiltonian. It is rather a precursor of a universal quantum computer that can simulate the dynamics of general quantum systems.

In the case of atoms the temperature to observe strongly correlated behavior is nine orders of magnitude lower than for electrons. The reason is the rather weak atomic interaction as compared to the Coulomb interaction. Although the temperature in present experiments is already close to absolute zero, the system is still far away from being in the ground state [25, 26, 43]. In the second part of this thesis we propose several schemes to cool the system to its many-body ground state, once the lattice potential has been raised. One class of protocols operates solely in the no-tunnelling regime and hence does not rely on equilibration. Since the required operations resemble the ones for ensemble quantum computation in optical lattices [44], we refer to it as "algorithmic cooling". We further show that algorithmic protocols can be used to generate an ensemble of defect-free quantum registers for quantum computation. The second class of cooling schemes permits quantum tunnelling and is based on the repeated application of occupation number filtering. The idea of filtering has been first proposed by Rabl et al. [45]. It aims at reducing lattice site occupation numbers to some desired values. The original proposal is based on a laser driven adiabatic transfer of atoms between two internal states. Here, we propose two alternative physical realizations of filtering. The first one relies on optimal coherent laser control and is optimized in speed. The second proposal can be implemented rather easily and operates continuously. We further provide a complete theoretical and numerical description of all our cooling schemes.

The third part of this thesis is devoted to the generation of a special class of entanglement in atomic systems, in which the atoms are entangled in real space. Typically atoms are entangled in internal space. For instance, one can use atomic interactions to entangle the internal states of atoms located at different lattice sites in a dynamical way [46, 47]. When applied to all atoms this procedure will generate the highly entangled cluster state [7], which forms the basis of the one-way quantum computer proposed in [8]. The motional entangled states considered here are a sequence of FQH states, analogous to the ones that appear in the context of the fractional quantum Hall effect in electronic systems [48]. The possibility of creating FQH atomic states as the Laughlin state [49] by rapidly rotating the trap confining the atoms has been discussed in several theoretical works [50, 51, 52, 53, 54, 55, 56, 57, 58]. However, experiments dealing with typically large number of particles have not yet succeeded in reaching these states. Here, we fully address the case of a small number of particles and design a realistic way of entangling them into FQH states. The central idea is to use a deep optical lattice as an amplifier of the experimental signal by providing multiple copies of a small atomic sample. We further discuss how to detect these entangled states by measuring different properties as their density profile, angular momentum or correlation functions. The possibility of creating and manipulating FQH states in a controlled way has attracted considerable interest in recent years. Apart from its importance for topological quantum computation it also promises to create individual anyons and to probe their fractional quantum statistics directly by exchanging two (quasi)particles [57].

This thesis is organized as follows. Chapter 2 is devoted to Localizable Entanglement in many-body systems. We begin with reviewing algebraically computable entanglement measures for bipartite systems. Then we give a formal definition of LE and derive quantities like entanglement length and entanglement fluctuations. We further connect the concept of LE with the idea of quantum repeaters. It follows a derivation of a lower bound on LE in terms of connected correlation functions. Details of the proof are presented in Appendix A. Next, we present a numerical method to compute the LE in large spin chains. This method is applied to ground states of various standard spin-1/2 chains. Afterwards we study gapped spin-1 models and compute the LE both for ground and thermal states. Furthermore, a possible connection between long range entanglement and hidden order is discussed. In this context we refer also to Appendix B, where it is shown how to compute the string order parameter and the LE analytically for matrix-product states (MPS) with qubit bonds.

In chapter 3 we propose and analyze several cooling schemes for atoms which are trapped in an optical lattice. We start with a discussion of the Bose-Hubbard model and properties of the initial state, such as temperature and entropy. To this end we have developed a fermionization procedure, which is discussed in detail in Appendix C. It follows a summary of the basic tools and figures of merit which underlie our cooling schemes. Afterwards a detailed analytical analysis of the cooling efficiency of occupation number filtering is presented. We further determine the optimal regimes for tunable experimental parameters and propose two physical realizations of filtering. We then propose, analyze and compare two ground state cooling schemes: sequential filtering and algorithmic cooling. We compare our analytical findings with exact numerical calculations. The underlying numerical method is presented in Appendix D. It follows a discussion of alternative cooling schemes. Finally, we propose two algorithmic protocols that are not very well suited for cooling but are optimized for creating defect-free quantum registers for ensemble quantum computation.

In chapter 4 we propose how to create and detect motional entangled states of a small number of atoms being trapped in a rotating harmonic potential. We first identify the entangled states with strongly correlated FQH states and study characteristic properties such as their density profile. Based on numerical calculations of the energy spectrum we design adiabatic paths in parameter space in order to reach these states. After analyzing the experimental feasibility of our proposal we discuss several detection schemes, which explicitly take the lattice setup into account. In Appendix E we address the problem of two interacting atoms in a three-dimensional harmonic trap analytically and explore the range of validity of the pseudo-potential approximation. To this end the zero range pseudo-potential is replaced by a finite range well potential.

The results presented in chapters 2 to 4 are published in [59, 60, 61, 62, 63, 64, 65] and [66], respectively.

Chapter 2

Localizable Entanglement

2.1 Introduction

The creation and distribution of entangled states plays a central role in quantum information theory, because it is the key ingredient for performing certain quantum information tasks, like teleportation [1] or quantum computation. In this respect, multiparticle quantum states can be considered as entanglement resources, naturally appearing in many physical systems. On the other hand, it is believed that the study of multipartite entanglement might prove fruitful in other fields of physics, like condensed matter, e.g. for understanding the complex physics of strongly correlated states [67, 68]. In particular it has been shown [13, 14, 15, 69, 70, 71] that the ground state entanglement of various spin systems may exhibit characteristic features at a quantum phase transition. Hence, it is desirable to find ways of characterizing and quantifying entanglement in multipartite systems.

In this chapter we define a measure for multipartite entanglement, which we have termed *Localizable Entanglement* (LE). It quantifies the bipartite entanglement contained in a multipartite state. To be more specific, LE is defined as the maximum entanglement that can be localized, on average, between two parties of a multipartite system, by performing local measurements on the other parties. Hence, LE is defined in an operational way and has a clear physical meaning. For instance, it can be used as a figure of merit to characterize the performance of quantum repeaters [17, 72]. It also allows one to define the notion of entanglement length, which characterizes the typical distance up to which bipartite entanglement can be localized in the system.

Note that, in the context of LE, particles are not traced out but measured. This is in contrast to earlier approaches, where the concurrence of the reduced density operator of two separated spins in a spin chain has been calculated (see e.g. [13, 14]). Although the concurrence exhibited characteristic features at a quantum phase transition, it does not detect long range quantum correlations.

The fundamental difference between tracing and measuring can be illustrated with two simple examples: For both the GHZ state [73] and the cluster state [7] it can readily be checked that the reduced density operator of any two qubits contains no entanglement at all. On the other hand one can find a local measurement basis, such that the LE is maximal. We further note that in the case of the GHZ-state the entanglement properties could also have been revealed by studying the connected version of the two-point correlation function. Indeed, the GHZ-state is one of many examples [59], for which correlations can be identified with quantum correlations, i.e. entanglement. However, this intimate connection does not hold true for all pure quantum states (as shown in [74]). For instance, in the case of the cluster state the LE is maximal, whereas the connected correlations are all zero. The results of this chapter can be summarized as follows:

(i) We give a formal definition of LE, introduce several variants and establish basic relations between them. Based on this definition we give a meaning to the notions *entanglement length* and *entanglement fluctuations*.

(ii) We prove for general pure qubit and qutrit states that LE can be lower bounded by connected two-particle correlation functions. This implies that quantum phase transitions, characterized by a diverging correlation length, are equivalently detected by a diverging entanglement length.

(iii) We present a numerical method that computes the LE in ground states, time-evolved states and thermal states of one-dimensional spin systems. It works efficiently for chains with up to 100 sites and is based on matrix-product states [75, 76] and the Monte Carlo method [77].

(iv) We study the LE in ground states of various spin-1/2 models. We find that the lower bound is typically tight. Moreover, the LE as well as the entanglement fluctuations exhibit characteristic features at a quantum phase transition. For instance, we observe a discontinuity in the first derivative of LE at a Kosterlitz-Thouless transition [18].

(v) We study the LE in gapped spin-1 systems. For the ground state of the Heisenberg antiferromagnet we observe that the lower bound is not tight. To be more precise, the entanglement length is infinite but the correlation length is finite. In this context we also comment on a possible connection between hidden order and long range entanglement. In particular, we present examples showing that, in general, such a connection does not exist. As a second example we study the LE of thermal states in the AKLT model [78].

We find that the entanglement length increases exponentially with the inverse temperature.

We note that the concept of LE has already been adopted by several groups in order to study the entanglement properties of multipartite spin systems [59, 61, 74, 79, 80, 81, 82, 83].

2.2 Entanglement of bipartite systems

In this section we briefly review the entanglement of bipartite systems of finite dimension. Physical states of such systems are described by density matrices ρ ($\rho = \rho^\dagger, \rho > 0, \mathrm{tr}\rho = 1$) acting in the Hilbert space of the composite system $\mathcal{H} = \mathcal{H}_A \otimes \mathcal{H}_B$. A state ρ is defined as *separable* if and only if it can be decomposed as a convex combination of product states:

$$\rho = \sum_i p_i \; \rho_i^A \otimes \rho_i^B, \tag{2.1}$$

with $\sum_i p_i = 1$ and $p_i > 0$. Inversely, a state ρ is called *entangled* if and only if such a decomposition does not exist. Often it is also desirable to quantify the *degree* of entanglement. For pure states ($\mathrm{tr}\rho^2 = 1$) a widely accepted entanglement measure exists, which can, in principle, be calculated for any Hilbert space dimension. In the case of mixed states ($\mathrm{tr}\rho^2 < 1$), however, closed expressions for the entanglement of a state ρ can typically be found only for low dimensional systems. In the following we give a summery of algebraically computable entanglement measures, which are used in this article.

2.2.1 Pure states

Any pure state of a bipartite system can be written in the Schmidt decomposition:

$$|\,\psi\rangle = \sum_{i=1}^{n} \lambda_i \; |\,\phi_i^A\rangle \otimes |\,\phi_i^B\rangle, \qquad (\lambda_i > 0) \tag{2.2}$$

where $\{|\,\phi_i^A\rangle\}$ and $\{|\,\phi_i^B\rangle\}$ are sets of orthonormal states for subsystems A and B. The Schmidt coefficients λ_i represent the features of the state $|\,\psi\rangle$, which are invariant under local unitary operations on the subsystems. By definition, the entanglement of a state cannot be increased by local operations and classical communication (LOCC). This characteristic distinguishes quantum correlations from classical correlations. As a consequence, any entanglement measure must be invariant under local unitary operations and thus should depend solely on the Schmidt coefficients λ_i. In this context it is useful to consider the reduced density operators $\rho_A = \mathrm{tr}_B |\,\psi\rangle\langle\psi\,|$ and $\rho_B = \mathrm{tr}_A |\,\psi\rangle\langle\psi\,|$ of subsystem A and subsystem B, respectively. The degree of mixing of ρ_A and ρ_B is directly related to the entanglement of $|\,\psi\rangle$. Hence, the *entropy of entanglement* [84] has been adopted as the standard measure of entanglement for pure states. It is defined as:

$$E_E(\psi) := S(\rho_A) = S(\rho_B) = -\sum_{i=1}^{n} \lambda_i^2 \log_2 \lambda_i^2. \tag{2.3}$$

Here, $S(\rho) = -\mathrm{tr}(\rho \log_2 \rho)$ denotes the von-Neumann entropy. This entanglement measure has been inspired by the observation that entanglement decreases our knowledge of local properties of the state. Another justification for this measure arises from the fact that a maximally entangled state and LOCC can be used to produce an arbitrary state $|\,\phi\rangle$. In this sense, the entropy of entanglement of $|\,\phi\rangle$ measures the "entanglement cost" of creating this state. To be more precise, one needs about $n \times E_E(|\,\phi\rangle)$ copies of the singlet state, $|\,\psi^-\rangle = (|\,01\rangle - |\,10\rangle)/\sqrt{2}$, for producing n copies of an arbitrary two qubit state $|\,\phi\rangle$.

The definition of entropy of entanglement holds for any dimension. In the special case of a 2×2 system an alternative entanglement measure is widely used, namely the *concurrence* [85]. For a pure state $|\,\psi\rangle$ it is defined as

$$C(\psi) = |\langle\psi^*\,|\sigma_y \otimes \sigma_y|\,\psi\rangle|, \tag{2.4}$$

where the complex conjugation is performed in the standard basis $\{|\,00\rangle, |\,01\rangle, |\,10\rangle, |\,11\rangle\}$ and σ_y is a Pauli matrix.

For qubits it can be shown that the entropy of entanglement is a convex, monotonously increasing function, $E_E = f(C)$, of the concurrence, with

$$f(C) := H\left(\frac{1+\sqrt{1-C^2}}{2}\right), \tag{2.5}$$

$$H(x) := -x \log_2 x - (1-x)\log_2(1-x), \tag{2.6}$$

and $H(x)$ being the Shannon entropy. In this article we will typically use the concurrence to measure the entanglement of a pure two qubit state $|\,\psi\rangle$, because it can most easily be related to the maximum connected correlation function of this state [Appendix A].

2.2.2 Mixed States

Any mixed state can be expressed as a convex sum over pure states:

$$\rho = \sum_i p_i \mid \psi_i \rangle \langle \psi_i \mid, \tag{2.7}$$

with $p_i > 0$ and $\sum_i p_i = 1$. Unfortunately, this pure state decomposition is not unique. This means that the entanglement of ρ is not simply given by the weighted sum over the pure state entanglement. Instead, one has to take the infimum with respect to all pure state decompositions. Using this convex roof construction the *entanglement of formation* [11, 12] of a mixed state ρ is defined as:

$$F(\rho) = \inf_{\{p_i, \psi_i\}} \sum_i \; p_i \; E_E(\psi_i). \tag{2.8}$$

In higher dimensions the underlying optimization problem is unsolved for general states. Only for 2×2 systems an algebraic solution exists. In the convex roof (2.8) one replaces E_E by the concurrence C (see Eq. (2.4)). This leads to the closed expression [85]:

$$C(\rho) = \max\{0, r_1 - r_2 - r_3 - r_4\}, \tag{2.9}$$

where the $r_i's$ are the square roots of the eigenvalues of the matrix $\rho\tilde{\rho}$ in descending order. Here the spin flipped matrix $\tilde{\rho}$ is defined as:

$$\tilde{\rho} = (\sigma_y \otimes \sigma_y)\rho^*(\sigma_y \otimes \sigma_y), \tag{2.10}$$

with the complex conjugation again taken in the standard basis. Making use of Eq. (2.5), it has been shown that the entanglement of formation in 2×2 systems can be expressed by the concurrence: $F(\rho) = f(C(\rho))$ [85].

For higher dimensional systems one can use the *negativity* [86] as entanglement measure. Its definition relies on the NPPT criterion for entanglement [87, 88]: if the partial transpose ρ^{T_A} has at least one negative eigenvalue, then the state ρ is entangled. If we express ρ in an orthonormal product basis,

$$\rho = \sum_{i,j} \sum_{k,l} \langle i, k \,|\rho|\, j, l \rangle \; \mid i \rangle_A \langle j \mid \otimes \mid k \rangle_B \langle l \mid, \tag{2.11}$$

then, the partial transpose with respect to system A is given by:

$$\rho^{T_A} = \sum_{i,j} \sum_{k,l} \langle i, k \,|\rho|\, j, l \rangle \; \mid j \rangle_A \langle i \mid \otimes \mid k \rangle_B \langle l \mid. \tag{2.12}$$

We define the negativity $\mathcal{N}$ of a state ρ as

$$\mathcal{N}(\rho) = ||\rho^{T_A}||_1 - 1, \tag{2.13}$$

where $||.||_1$ is the 1-norm, given by the sum of the moduli of the eigenvalues. Since transposition is trace preserving, $\mathcal{N}(\rho)$ is given by two times the sum of the moduli of the negative eigenvalues of ρ^{T_A}. With this definition, the negativity of the singlet state is one. The negativity has the big advantage that it can be calculated algebraically in any dimension. However, for systems larger than 2×3 it vanishes for some entangled states [89, 90] and thus it is not an entanglement measure in the strict sense. But since it is non-increasing under LOCC , it is an entanglement monotone [86].

2.3 Localizable Entanglement of multipartite systems: Definition and basic properties

We consider a multipartite system composed of N particles. With each particle we associate a finite dimensional Hilbert space. For simplicity we refer in the following to the particles as spins.

2.3.1 Definition

The Localizable Entanglement (LE) of a multi-spin state ρ is defined as the maximal amount of entanglement that can be created (i.e. localized), on average, between two spins at positions i and j by performing local measurements on the other spins. More specifically, every measurement $\mathcal{M}$ specifies a state ensemble $\mathcal{E}_{\mathcal{M}} := \{p_s, \rho_s^{ij}\}$. Here p_s denotes the probability to obtain the (normalized) two-spin state ρ_s^{ij} for the outcome s of the measurements on the $N-2$ remaining spins. The average entanglement for a specific $\mathcal{M}$ is then given by:

$$\overline{L}_{i,j}^{\mathcal{M},E}(\rho) := \sum_s p_s \; E(\rho_s^{ij}), \tag{2.14}$$

where $E(\rho_s^{ij})$ is the entanglement of ρ_s^{ij}. The Localizable Entanglement is defined as the largest possible average entanglement:

$$L_{i,j}^{\mathcal{C},E}(\rho) := \sup_{\mathcal{M}\in\mathcal{C}} \sum_s p_s \; E(\rho_s^{ij}), \tag{2.15}$$

with $\mathcal{C}$ denoting the class of allowed measurements. We call the measurement $\mathcal{M}$ which maximizes the average entanglement the *optimal basis*. It is important to note that the only restriction on $\mathcal{M}$ is that the measurements are performed locally i.e. on individual spins. Apart from that, the measurement basis is arbitrary and can also vary from site to site. We distinguish three classes $\mathcal{C}$ of measurements: projective von-Neumann measurements

(PM), those corresponding to positive operator-valued measures (POVM), and general local measurements that allow also for classical communication of measurement results (LOCC). In terms of LE the following relationship between these classes holds [1]:

$$L_{i,j}^{\mathrm{PM},E}(\rho) \leq L_{i,j}^{\mathrm{POVM},E}(\rho) \leq L_{i,j}^{\mathrm{LOCC},E}(\rho). \tag{2.16}$$

In this thesis we will be mainly concerned with projective measurements. To simplify the notation we omit in this case the superscript PM.

The definition (2.15) still leaves open the choice of the entanglement measure E for the states $\{\rho_s^{ij}\}$. In the previous section we have listed algebraically computable entanglement measures for small dimensional systems. In the case of a *pure* multipartite state ρ, the states $\{\rho_s^{ij}\}$ after the measurements are also pure. Hence, in any dimension we can use the entropy of entanglement E_E (2.3) as entanglement measure. For pure qubit states we typically choose the concurrence C (2.4). Due to the convexity of the function f (2.5) one can find the following relation for the LE as measured by these two quantities:

$$f\left(L_{ij}^{C}\right) \leq L_{ij}^{E_E} \leq L_{ij}^{C}. \tag{2.17}$$

Therefore the qualitative behavior of these two variants of LE will be very similar.

In the case of *mixed* qubit states we make use of the closed expression for the concurrence (2.9). For higher dimensional mixed states we refer to the negativity $\mathcal{N}$ (2.13).

2.3.2 Entanglement length and fluctuations

In the field of strongly correlated systems and more specifically in the study of quantum phase transitions, the correlation length, ξ_C, is of great importance. The concept of LE readily lends itself to define the related *entanglement length*, ξ_E, which characterizes the typical distance up to which bipartite entanglement can be localized in the system:

$$\xi_E^{-1} := \lim_{n\to\infty}\left(\frac{-\ln L_{i,i+n}^{E}}{n}\right). \tag{2.18}$$

---

[1] For pure four qubit states it has been shown in [91], that in the case of projective measurements the LE cannot be increased by classical communication. In addition, numerical studies for the same system indicated that POVM measurements lead only to a very small increase of LE, compared to projective measurements.

The entanglement length is finite if and only if $L^E_{i,i+n} \rightarrow \exp(-n/\xi_E)$ for $n \rightarrow \infty$, and the entanglement length ξ_E is defined as the constant in the exponent in the limit of an infinite system (see also Aharonov [92]).

Let us now have a closer look at the statistical nature of LE, as it is defined as an average over all possible measurement outcomes (see (2.15)). For practical purposes one can only control the measurement basis but not a specific outcome. Therefore it would be useful to have an estimate of how much the entanglement of a particular measurement outcome deviates from the mean value as given by the LE. This information is contained in the variance of the entanglement remaining after measurements. We can thus define the notion of *entanglement fluctuations*:

$$(\delta L^{\mathcal{M},E}_{i,j})^2 := \left(\sum_s p_s \; E(\rho_s^{ij})^2\right) - L^{\mathcal{M},E^2}_{i,j}. \tag{2.19}$$

The entanglement fluctuations can be defined for any measurement $\mathcal{M}$. Typically we choose for $\mathcal{M}$ the optimal basis, which maximizes the average entanglement. In this case we drop the index $\mathcal{M}$ in (2.19).

The study of both the entanglement length and the entanglement fluctuations could provide further inside in the complex physics of quantum phase transitions by revealing characteristic features at the quantum critical point. Examples for this are presented in Sect. 2.6.

2.3.3 Connection to quantum repeaters

So far we have given a purely mathematical definition of LE (2.15). However, it is evident that the LE is defined in an operational way that can directly be implemented on certain physical systems. In addition the concept of LE may also play an essential role in some interesting applications of quantum information theory. To be more precise, LE can serve as a figure of merit for the "performance" of certain kinds of quantum repeaters (QR).

Many tasks in quantum information processing require long-distance quantum communication. This means quantum states have to be transmitted with high communication fidelity via a quantum channel between two distant parties, Alice and Bob. Since quantum transport is also possible via teleportation [1] this problem is equivalent to establishing nearly perfect entanglement between two distant nodes. All realistic schemes for quantum communication are presently based on the use of photonic channels. However, the degree of entanglement generated between distant sites typically decreases exponentially with the length of the connecting physical channel, due to light absorption and other channel noise. To overcome this obstacle the concept of quantum repeaters has been introduced [17, 72]. The central idea is to divide the channel into segments and to include additional nodes. Entanglement between adjacent nodes can be extended to larger distances using entanglement swapping followed by purification. After several rounds one obtains a pair of almost maximally entangled nodes, shared by Alice and Bob, that can be used for perfect quantum transport via teleportation. A possible physical realization of the QR using trapped atoms is sketched in Fig. 2.1 [93, 94, 95].

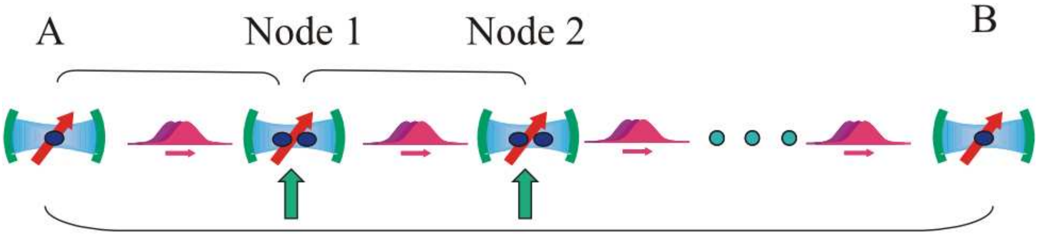

Figure 2.1: Illustration of the quantum repeater scheme for trapped atoms connected by optical fibres. Qubits are represented by the internal states of the atoms. Applying laser beams the internal states of atoms in adjacent cavities become entangled via the transmission of photonic states. Collective measurements on the nodes (indicated by arrows) followed by purification lead to the generation of a nearly perfectly entangled pair of qubits between the outermost cavities A and B.

Let us now discuss how a QR setup can be characterized by the LE. First of all, let us identify the particles sitting at different nodes by spins. It is important to note that, by combining several spins to a larger Hilbert space of dimension d, the operations required for purification and entanglement swapping on this set of spins can be interpreted as local operations on a single spin of dimension d. Thus the QR can be treated as a system of interacting spins being in a state ρ. In order to assess and quantify the usefulness of such a setup as a QR one has to compute the following figure of merit: What is the maximum amount of entanglement that can be generated between the two end spins by performing local operations on the intermediate spins? But this number is nothing else than the LE. The question, which variant of LE (2.16) should be used, depends on the class of available local operations (PM, POVM or LOCC). Typically classical communication is allowed so that L_{ij}^{LOCC} has to be taken as figure of merit. However, not every measurement might be physically realizable. Therefore the LE will in general give an upper bound for the performance of a given QR setup.

2.4 Bounds on LE

Due to its variational definition, the LE is very difficult to calculate in general. Moreover, typically one does not have an explicit parameterization of the state under interest, but just information about the classical one- and two-particle correlation functions (which allows one to parameterize completely the two-spin reduced density operator ρ_{ij}). It would therefore be interesting to derive tight upper and lower bounds to the LE solely based on this information.

2.4.1 Upper bound

The upper bound can readily be obtained using the concept of entanglement of assistance (EoA) [96], which can be defined for bipartite mixed states ρ_{AB} of any (finite) dimension. We identify ρ_{AB} with the reduced density operator ρ_{ij} for spins i and j. The EoA is then defined as:

$$A_{ij}^{E}(\rho_{ij}) := \sup_{\mathcal{E}} \sum_{s} p_s \; E(\psi_s^{ij}). \tag{2.20}$$

Here the supremum is taken over all pure state decompositions $\mathcal{E} = \{p_s, |\psi_s^{ij}\rangle\}$, with $\rho_{ij} = \sum_s p_s |\psi_s^{ij}\rangle\langle\psi_s^{ij}|$, and E is a suitable entanglement measure for pure states. If ρ_{ij} is the reduced density matrix of a *pure* N-partite spin state ψ_N, then EoA can be interpreted as follows. It is the maximum average entanglement that can be created between spins i and j by performing *joint* measurements on the remaining $N-2$ spins. Hence, EoA is trivially an upper bound of LE, because local measurements are a subclass of joint measurements. If ρ_{ij} represents a pair of qubits, one can derive an explicit formula for EoA [91]. Given ρ_{ij} and a square root X, $\rho_{ij} = XX^\dagger$, then the EoA as measured by the concurrence reads:

$$A_{i,j}^{C}(\rho_{ij}) := \mathrm{tr}|X^T(\sigma_y^i \otimes \sigma_y^j)X| \;, \tag{2.21}$$

with $|B| = \sqrt{B^\dagger B}$. Hence $A_{i,j}^{C}(\rho_{ij}) = \sum_{k=1}^{4} \sigma_k$, where σ_k are the singular values of the matrix $X^T(\sigma_y^i \otimes \sigma_y^j)X$. Note that for pure four qubit states a variant of EoA with local measurements was considered in [91].

2.4.2 Lower bound

First, from the definition of LE (2.15) it follows that any specific measurement, e.g. in the computational basis, trivially provides a lower bound on the LE. More interestingly, we will now prove for general *pure* spin-1/2 and spin-1 states that the LE is lower bounded by connected correlation functions.

Spin-1/2 systems

The basic idea is to establish a connection between the LE and connected correlation functions of the form:

$$Q_{AB}^{ij} = \mathrm{tr}[\rho(\ S_A^i \otimes S_B^j)] - \mathrm{tr}[\rho(\ S_A^i \otimes \mathbb{1})]\mathrm{tr}[\rho(\mathbb{1} \otimes S_B^j)]. \tag{2.22}$$

For qubits the operators S_A, S_B can be parameterized by directions $\vec{a}, \vec{b}$, representing unit vectors in a 3D real space: $S_A = \vec{a} \cdot \vec{\sigma}, S_B = \vec{b} \cdot \vec{\sigma}$ with $\vec{\sigma} = (\sigma_x, \sigma_y, \sigma_z)$ being the vector of the Pauli matrices.
Let us start out with stating the central theorem of this section:
(1.i) Given a (pure or mixed) state of N qubits with connected correlation function Q_{AB}^{ij} between the spins i and j and directions $\vec{a}, \vec{b}$, then there always exists a basis in which one can locally measure the other spins such that this correlation does not decrease, on average.
The proof, which is rather technical but constructive, is presented in Appendix A. There we also show that this result can be generalized to a setup, where the spins i and j can be of any dimension, but the remaining spins (on which the measurements are performed) are still qubits. In a spin-1/2 system such a situation can arise, for example, when considering correlations between two blocks of spins.

Next, we relate correlations with entanglement. We note that after the measurement process and for an initially pure state we end up with a pure state of two qubits. For such a state we have proven the following result [Appendix A]:
(1.ii) The entanglement of a pure two qubit state $|\psi_{ij}\rangle$ as measured by the concurrence is equal to the maximal connected correlation function:

$$C(\psi_{ij}) = \max_{\vec{a},\vec{b}} |\ Q_{AB}^{ij}(\psi_{ij})|. \tag{2.23}$$

Combining *(1.i)* and *(1.ii)* we know that for a given pure multi qubit state $|\psi\rangle$ and directions $\vec{a}, \vec{b}$ there always exists a measurement $\mathcal{M}$ such that:

$$Q_{AB}^{ij}(\psi) \leq \sum_s p_s Q_{AB}^{ij}(\psi_s) \leq \sum_s p_s C(\psi_s). \tag{2.24}$$

The term on the very right is equal to the average entanglement as measured by the concurrence $L_{ij}^{\mathcal{M},C}$, which trivially is a lower bound to the LE as defined by L_{ij}^C. Since the directions $\vec{a}, \vec{b}$ can be chosen arbitrarily, relation (2.24) holds in particular for directions maximizing $Q_{AB}^{ij}(\psi)$. Hence we can establish the desired lower bound on LE:
(1.iii) Given a pure state $|\psi\rangle$ of N qubits, then the LE as measured by the

concurrence is larger or equal than the maximal connected correlation function:

$$L^C_{i,j}(\psi) \geq \max_{\vec{a},\vec{b}} |Q^{ij}_{AB}(\psi)|. \tag{2.25}$$

Making use of the basic properties of LE, presented in the previous section, we can immediately derive analogous bounds for some other variants of LE; for example,

$$\begin{aligned} L^{E_E}_{i,j}(\psi) &\geq f(\max_{\vec{a},\vec{b}} |Q^{ij}_{AB}(\psi)|), & (2.26)\\ L^{\mathrm{POVM,E_E}}_{i,j}(\psi) &\geq f(\max_{\vec{a},\vec{b}} |Q^{ij}_{AB}(\psi)|), & (2.27)\end{aligned}$$

with f being the convex function defined in (2.5). We will see below that relation (2.27) can be generalized to spin-1 systems.

Higher dimensional spin systems

We now try to extend the previous findings beyond spin-1/2 systems. First, we look for a generalized version of statement *(1.i)*. Unfortunately the techniques used in the proof for qubits seem to fail already for qutrits. Nevertheless, a generalization is still possible by changing a little bit the perspective. For this we embed a spin-S in a higher dimensional Hilbert space, being composed of $n \geq \log_2(2S+1)$ *virtual* qubits. Let us denote the $(2S+1)\times 2^n$ matrix governing this transformation by P.

In the case $2S+1 = 2^n$ the embedding is trivial and the situation becomes equivalent to the qubit case. Thus the result *(1.i)* can immediately be generalized, because local measurements on the virtual qubit systems can be chosen such that *(1.i)* holds.

In the case $2S+1 < 2^n$ a similar argument applies if we allow for POVM measurements on the spin-S system. To be more precise, let us consider a mixed state ρ of three spin-S particles. The spin on which the measurement is performed (let us denote it with the index 3) is embedded in a 2^n dimensional system. The embedded state is then given by the transformation: $\rho' = (\mathbb{1}_{12} \otimes P_3^\dagger)\rho(\mathbb{1}_{12} \otimes P_3)$. In the Hilbert space of the n virtual qubits one always finds local projective measurements $\{M_{\alpha_1\ldots\alpha_n}\} = \{|\alpha_1\rangle\langle\alpha_1| \otimes \ldots \otimes |\alpha_n\rangle\langle\alpha_n|\}$ such that (the generalized version of) *(1.i)* holds for the state ρ'. In terms of the original state ρ this measurement in the 2^n dimensional space corresponds to a POVM measurement $\{PM_{\alpha_1\ldots\alpha_n}P^\dagger\}$ on a spin-S system, because: $\sum_{\alpha_1\ldots\alpha_n} PM_{\alpha_1\ldots\alpha_n}P^\dagger = P\mathbb{1}_{2^n\times 2^n}P^\dagger = \mathbb{1}_{(2S+1)\times(2S+1)}$.

Thus one can generalize the result *(1.i)* to arbitrary spin dimensions in the following way:

(2.i) Given an arbitrary multi-spin state with connected correlation function Q^{ij}_{AB} *between spins* i *and* j *for arbitrary operators* S_A, S_B*, then there always exists a local POVM measurement on the other spins such that this correlation does not decrease, on average.*

We note that the lower bound in *(2.i)* can already be reached by applying *local* measurements on the virtual qubit system. Performing joint measurements (e.g. Bell measurements on pairs of qubits as shown in [74]) can lead to a considerable enhancement of the average correlations. If in addition $2^n - (2S+1)$ joint measurements can be chosen such that they are orthogonal to the projector P, the resulting measurement on the spin-S system corresponds to a projective von-Neumann measurement.

The most difficult part is to establish a connection between correlations and entanglement for pure two spin states in analogy of *(1.ii)*. In the case of qubits we made explicitly use of the fact that the group $SU(2)$ is the covering group of $SO(3)$. Moreover the concurrence served as an entanglement measure, which was easy to handle. For higher spin dimensions we refer to the entropy of entanglement E_E (2.3) as a suitable entanglement measure for pure bipartite states. In the special case of qutrits we were able to show the following relation [Appendix A]:

(2.ii) The entanglement of a pure two qutrit state $|\psi_{ij}\rangle$ *as measured by the entropy of entanglement can be lower bounded by:*

$$E_E(\psi_{ij}) \geq f(\max_{A,B} |\, Q^{ij}_{AB}(\psi_{ij})|), \tag{2.28}$$

where f is the convex function (2.5) and S_A, S_B in Q^{ij}_{AB} (2.22) are operators, whose eigenvalues lie in the interval $[-1; 1]$. Combining again *(2.i)* and *(2.ii)* we can formulate a bound on LE for spin-1 systems:

(2.iii) Given a pure state $|\psi\rangle$ *of* N *qutrits, then the LE as measured by the entropy of entanglement and which allows for* POVM's*, is lower bounded by the maximum connected correlation function in the following way:*

$$L^{\mathrm{POVM,E_E}}_{ij}(\psi) \geq f(\max_{A,B} |Q^{ij}_{AB}(\psi)|). \tag{2.29}$$

In summary, we have shown for pure qubit and qutrit states that connected correlation functions provide a lower bound on LE. This bound allows for two intriguing limiting case: (i) Entanglement and correlations may exhibit similar behavior. (ii) Spins may be maximally entangled although they are uncorrelated in the classical sense. In the forthcoming sections we will present examples for both scenarios.

2.5 Numerical computation of LE

In this section we develop a numerical method that allows us to compute the LE in ground states, thermal states and time-evolved states in one-dimensional spin systems with large number of spins. We first consider pure states and show how for a given measurement basis the average entanglement can be computed efficiently. To this end we represent the many body state in terms of a matrix-product state and make use of the Monte Carlo method [77]. Then we discuss several ways of determining the optimal measurement basis. Finally, we develop an algorithm based on matrix-product states that computes the ground state of a spin chain with periodic boundary condition. In the second part we generalize our numerical method to mixed states.

2.5.1 Pure states

We consider pure quantum states of a chain of N interacting spins of dimension $d = 2S + 1$. These states can be ground or excited states of a given Hamiltonian, or states resulting from time evolution of pure states. The number of parameters for the characterization of a N-body quantum state increases exponentially with N. Hence, the exact numerical treatment of the problem is typically limited to very small system sizes. For larger systems one has to refer to approximative methods.

Here, we represent pure states in terms of the the so-called matrix product states (MPS) [75, 76]:

$$|\psi_{\mathrm{MP}}\rangle = \sum_{s_1,\ldots,s_N=1}^{d} \mathrm{Tr}(A_1^{s_1}\ldots A_N^{s_N})|s_1,\ldots,s_N\rangle. \tag{2.30}$$

The state is described by N matrices $A_i^{s_i}$ of maximal dimension D. We note that the MPS (2.30) is written in the computational basis and accounts for periodic boundary conditions (PBC). It has been shown [76, 97] that MPS appear naturally in the context of the density-matrix renormalization group (DMRG) method [98]. Below we will also discuss alternative methods to obtain ground states or time-evolved states using the MPS representation. Note that starting from these states, it is possible to calculate expectation values of products of local observables $\{O_i\}$ very efficiently [76, 97, 75]:

$$\langle\Psi|O_1\ldots O_N|\Psi\rangle = \mathrm{Tr}\left(E_{O_1}^{[1]}\ldots E_{O_N}^{[N]}\right), \tag{2.31}$$

where

$$E_O^{[k]} = \sum_{s,s'=1}^{d} \langle s|O_k|s'\rangle A_k^s \otimes \left(A_k^{s'}\right)^*. \tag{2.32}$$

Given an MPS of the form (2.30), let us now present a scheme to compute the LE from that. For translation invariant systems it is sufficient to consider the LE between the spins 1 and $j = 1 + n$. We perform projective measurements in the local basis of (2.30). The (pure) state of the two spins of interest after the measurements is conditioned on the measurement outcomes, denoted by the (N-2)-tuple $\{s\} := \{s_2 \dots s_{j-1} s_{j+1} \dots s_N\}$, and proportional to

$$|\phi_{\{s\}}\rangle = \langle\{s\}|\psi_{\mathrm{MP}}\rangle = \sum_{s_1, s_j = 1}^{d} \mathrm{Tr}(A_1^{s_1} \dots A_N^{s_N})|s_1\rangle|s_j\rangle. \tag{2.33}$$

Without loss of generality we can assume that the computational basis is the optimal one for LE [2]. The LE is then given by:

$$L_{ij}^{E}(\psi_{\mathrm{MP}}) = \sum_{\{s\}} p_{\{s\}} E(\tilde{\phi}_{\{s\}}) \ , \tag{2.34}$$

where $p_{\{s\}} = \langle\phi_{\{s\}}|\phi_{\{s\}}\rangle / \langle\psi_{\mathrm{MP}}|\psi_{\mathrm{MP}}\rangle$ is the probability for obtaining the normalized state $|\tilde{\phi}_{\{s\}}\rangle = |\phi_{\{s\}}\rangle / \langle\phi_{\{s\}}|\phi_{\{s\}}\rangle^{1/2}$. The MPS representation allows us to compute the probabilities $p_{\{s\}}$ and the states $|\phi_{\{s\}}\rangle$ efficiently, because it simply amounts to the multiplication of N matrices. However, we still face the problem that the sum (2.34) involves an exponential number of terms (d^{N-2}). In order to obtain a good approximation of this sum we propose a scheme based on the Monte Carlo (MC) method, which will be now explained in more detail.

Monte Carlo method

The Monte Carlo method provides an efficient way of selecting M states $|\phi_\mu\rangle$ sequentially from the (given) probability distribution $\{p_{\{s\}}\}$ of the measurement results. The LE can thus be approximated by:

$$L_{(MC),ij}^{E}(\psi_{\mathrm{MP}}) \approx \frac{1}{M} \sum_{\mu=1}^{M} E(\tilde{\phi}_\mu) \ \pm \ \frac{1}{\sqrt{M}} \, \delta L_{ij}^{E}(\psi_{\mathrm{MP}}). \tag{2.35}$$

Note that the accuracy of the MC method depends on the entanglement fluctuations δL_{ij}^{E}, which can be computed within the MC scheme as well.

---

[2] Otherwise we can make a change of basis in (2.30), defined by unitary operators $\{U_i\}$. For each site i this amounts to transforming the corresponding MPS matrix: $A_i^s \rightarrow \tilde{A}_i^s = \sum_{s'} U_i^{ss'} A_i^{s'}$. Hence, the following discussion can immediately be generalized to an arbitrary basis by replacing the matrices $\{A_i^{s_i}\}$ by the transformed ones $\{\tilde{A}_i^{s_i}\}$.

For selecting the states $|\phi_\mu\rangle$ we follow the Metropolis algorithm [77] and use single-spin-flip dynamics. We start with an initial state $|\phi_\mu\rangle$ corresponding to a specific measurement outcome $\{s\}$. From this we create a trial state $|\phi_\nu\rangle$ by randomly picking a site i and changing the state of this spin with equal probability according to $s_i \to \mathrm{mod(s_i \pm 1, d)}$ for $s_i = 0, 1, \ldots d-1$. For a spin-1/2 this simply amounts to a spin flip. The trial state is accepted with probability:

$$P(\mu \to \nu) = \begin{cases} \frac{p_\nu}{p_\mu} & \text{if } \mathrm{p}_\nu < \mathrm{p}_\mu \ , \\ 1 & \text{else} \ . \end{cases} \tag{2.36}$$

If the trial state is accepted it serves as a starting point for creating a new trial state. After $N-2$ steps, defining one MC sweep, the entanglement of the current state is calculated [3]. After M sweeps the algorithm stops and the average (2.35) is performed.

Computational Effort

Let us now discuss the computational effort with respect to computation time. Given a MPS of form (2.30) we estimate the number of operations that have to be performed for the calculation of LE. At each step of the MC algorithm a trial state has to be computed. According to Eq. (2.33) this involves the multiplication of N matrices $A_i^{s_i}$. Given that these matrices have a maximal dimension D, one has to perform $\mathcal{O}(ND^3)$ operations. This can be improved to $\mathcal{O}(\log_2(N) D^3)$ by taking into account that only a single spin has to be flipped for the calculation of the trial state. Note that this result refers to PBC. In the case of OBC the trace in Eq. (2.33) is replaced by a scalar product, meaning that the first and the last matrix represent vectors (see also [61]). This reduces the computational effort for the calculation of the trial state to $\mathcal{O}(ND^2)$ operations. For M MC sweeps we obtain in total $\mathcal{O}(MN\log_2(N)D^3)$ operations for PBC and $\mathcal{O}(MN^2D^2)$ operations for OBC. Exploiting single-spin flip dynamics in the case of OBC yields the computational effort of PBC. Hence, this is only favorably, if $N > \log_2 ND$.

Finding the optimal measurement basis

The definition of LE (2.15) requires an optimization over all possible measurement strategies. A good guess for the optimal basis can typically by found using exact diagonalization for small system sizes, followed by numerical maximization of the average entanglement. Alternatively, the optimal

---

[3] Note that with this definition the number of sweeps M is independent of the system size N.

basis can also be extracted directly from the MPS matrices A_i in (2.33). Using a generalization of the concurrence for pure bipartite $D \times D$ states, it has been shown in [74] (for an open chain with D-dimensional spins at the ends), that the optimal basis is the same basis, that maximizes the expression $\sum_{s_i} |\det(A_i^{s_i})|^{2/D}$ [see Appendix B for details]. This result can be interpreted in the following way. We can consider the matrices A_i as (unnormalized) pure $D \times D \times d$ states, for which we want to calculate the LE with respect to the $D \times D$ system. Since we measure only on a single site this problem is equivalent to calculating the EoA of the reduced ($D^2 \times D^2$) density matrix, which can easily be done numerically. In the special case of qubit bonds ($D = 2$) it can even be solved analytically (see [74] and Appendix B). Remember that this argumentation has been derived based on the generalized concurrence, which, unfortunately, is not always a good entanglement measure for $D > 2$. The question arises whether it also holds for other entanglement measures, such as the entropy of entanglement. To this end we have computed numerically the LE of the tripartite states defined by the matrices A_i for different entanglement measures and for different spin models. We find that the optimal basis for this problem indeed coincides with the one for our original problem, which we deduce from exact diagonalization of a small chain. As a further numerical result we find that the optimal basis appears to be independent of the system size. Hence, we find it most convenient to determine the optimal basis for small systems using exact diagonalization and then extrapolate the result to larger systems. Also, this approach turns out to be more reliable with respect to the occurrence of local maxima in the optimization problem.

Analytically, the determination of the optimal measurement strategy remains a hard problem. So far it has been proven that an extremal basis can be inferred from certain symmetries of the Hamiltonian, like parity symmetry [99]. It remains to be proven that this basis yields indeed the global maximum for LE. However, our numerical findings give strong indications that this connection holds.

Numerical Calculation of ground states based on the MPS formalism

It has been mentioned already that the DMRG method of White [98] for the calculation of many-body ground states yields a state in MPS form. This method is very well suited both for finite and infinite systems with OBC. Recently, it has been shown that it can be much more rewarding to work directly with the MPS representation. E.g. in [100] it has been demonstrated that this variational approach yields much better results for the computation of ground states in systems with PBC. Furthermore, it can applied to the simulation of time evolution of quantum states [101, 102] and the computation of excited states [103]. Using the picture of projected-entangled-pair states this approach can even be generalized to two and higher dimensions [44].

In the following we will propose an alternative numerical method for computing ground states in 1D systems with PBC. It is based on the following idea: We use the DMRG algorithm for an infinite chain to extract a site-independent set of matrices A^s, defining a translationally invariant MPS (2.30) for infinite N. We then us the same set A^s to construct a MPS with PBC for arbitrary N. It is obvious that this method is very efficient, particularly for large N, because we have to run the DMRG only once to obtain the MPS representation for any system size. One might expect that this increase in efficiency happens at the cost of precision. However, an optimum in accuracy on the part of the MPS is not crucial for the numerical calculation of the LE, since the limiting factor for the accuracy is typically the MC method.

We start out with briefly reviewing the variant of DMRG, represented by $B \bullet B$ [97], for an infinite 1D chain. At some particular step the chain is split into two blocks and one spin in between. The left block (L) contains spins $1, \ldots, M-1$, and the right one (R) spins $M+1, \ldots, N$. Then a set of $D \times D$ matrices $\tilde{A}^{s_M}$ is determined such that the state

$$|\Psi\rangle = \sum_{s=1}^{d} \sum_{\alpha,\beta=1}^{D} \tilde{A}^{s_M}_{\alpha,\beta} |\alpha\rangle_L \otimes |s\rangle_M \otimes |\beta\rangle_R, \tag{2.37}$$

minimizes the energy. The states $|\alpha\rangle_{L,R}$ are orthonormal, and have been obtained in previous steps. They can be constructed using the recurrence relations

$$|\alpha\rangle_L = \sum_{\alpha'=1}^{D} \sum_{s=1}^{d} U^{[M-1],s}_{\alpha,\alpha'} |s\rangle_{M-1} \otimes |\alpha'\rangle_{L'}, \tag{2.38}$$

where the block L' contains the spins $1, \ldots, M-2$.

Numerically we find that the matrices $U^{[k],s}$ can be chosen in such a way that they converge to (site independent) matrices U^s at the fix point of the DMRG algorithm. Applying an appropriate transformation R, these matrices U^s can be used to construct a translationally invariant MPS (2.30) with $A^s = RU^sR^{-1} = R\tilde{A}^sR^T$ [4].

---

[4] We note that for antiferromagnetic systems only every second matrix $U^{[k],s}$ converges, resulting in an alternating MPS structure $A^{s_1}B^{s_2}A^{s_3}\ldots B^{s_N}$. One can show that the translationally invariant state which minimizes the energy is then given by the linear superposition $A^{s_1}B^{s_2}A^{s_3}\ldots B^{s_N} + B^{s_1}A^{s_2}B^{s_3}\ldots A^{s_N}$.

As a first test of our method we have calculated the energy per site of an infinite chain, using the translationally invariant MPS. We have confirmed that the result is as accurate as the one obtained directly from DMRG. We then applied it to construct ground states for finite chains with PBC and to compute ground state expectation values according to (2.31). Our numerical analysis of various 1D systems shows that both the energy and the two-body correlation functions can be computed rather accurately. The achieved accuracy is several orders of magnitude higher than finite size effects, but also several orders of magnitude lower compared to the variational method [100]. These findings hold for system sizes as low as $N \approx 10$. This is rather surprising, because the MPS is constructed from an infinite chain. We further checked that also the long range behavior of correlations and entanglement is reproduced correctly by our translationally invariant MPS.

To sum up, our numerical results indicate that translationally invariant states can be sufficiently well approximated by a single set of MPS matrices A^s for almost arbitrary system size N. This observation, together with the findings in [74], might shed some light on our previous numerical finding that the optimal measurement basis for LE is typically both site-and size-independent.

2.5.2 Mixed states

Let us now consider the case of multipartite mixed states. Note that the definition of LE (2.15) already includes the possibility of having a mixed state ρ. This implies that the states $\rho_{\{s\}} = \langle\{s\}|\rho|\{s\}\rangle$ after the measurements are also mixed. Hence, we typically refer in the following to the LE as measured by the negativity: L^N_{ij}. Only in the special case of $\rho_{\{s\}}$ being a two qubit state, we resort to the concurrence and thus L^C_{ij}.

Numerical method

Our method for the numerical computation of LE in pure states can be generalized to mixed states in the following way. The key point is to find a representation of a mixed state in terms of low dimensional matrices A_k, analogous to the MPS (2.30). This problem has been considered recently in [102, 104]. There the concept of MPS is generalized to matrix product density operators (MPDO), which are defined as

$$\rho = \sum_{s_1,s'_1,\ldots,s_N,s'_N=1}^{d} \mathrm{Tr}(M_1^{s_1,s'_1}\ldots M_N^{s_N,s'_N}) \times|s_1,\ldots,s_N\rangle\langle s'_1,\ldots,s'_N|, \tag{2.39}$$

where $M_k^{s_k,s'_k}$ are $D_k^2 \times D_{k+1}^2$ matrices. They can be decomposed as

$$M_k^{s,s'} = \sum_{a=1}^{d_k} A_k^{s,a} \otimes (A_k^{s',a})^*. \tag{2.40}$$

The state ρ can be purified into a MPS by including ancilla states $\{|a_k\rangle\}$ of dimension d_k:

$$|\Psi\rangle = \sum_{s_1,\dots,s_N} \sum_{a_1,\dots,a_N} \mathrm{Tr}\left(\prod_{k=1}^{N} A_k^{s_k,a_k}\right) |s_1 a_1, \dots, s_N a_N\rangle. \tag{2.41}$$

This means that thermal states of the form $\rho \propto e^{-\beta H} = e^{-\beta/2H} \mathbb{1} e^{-\beta/2H}$ can be calculated by imaginary time evolution of the purification of the identity. At each time step the dimension of the matrices A_k increases [105]. In [101, 102, 104] it is shown how to truncate the matrices to a maximal dimension D in an optimal way. Note that this approach can also be used to simulate real time evolution given by a generic Master equation.

Once a mixed state of the form (2.39) has been found one can calculate the LE along the same lines as for pure states.

Computational effort

The numerical computation of LE for mixed states is much more time consuming than for pure stats. The reason is that the matrices M_k in (2.39) have dimension $D^2 \times D^2$, compared to the $D \times D$ matrices A_k for pure states. Note that the calculation of the trial state can be optimized by changing the order in the contraction of tensor indices. One can show that in the case of PBC the computation time is of the order $\mathcal{O}(MN \log_2(N) dD^5)$ and for OBC it scales as $\mathcal{O}(MN^2 dD^3)$. Here, d denotes the dimension of the physical spin. Typically, one has $\log_2(N) D^2 \gg N$ and thus the choice of OBC is preferable. Note also that the algorithm for the calculation of thermal states using MPDO's is much faster with OBC than with PBC.

2.6 LE in spin-$1/2$ chains

In this section we apply the concept of LE to quantify the localizable ground state entanglement of various spin-1/2 models. After some general considerations we compute the LE as measured by the concurrence $L^C_{i,j}$ numerically for two specific examples.

2.6.1 General considerations

We consider spin-1/2 Hamiltonians of the form

$$H = -\sum_{i,j} \sum_{\alpha=x,y,z} \gamma_\alpha^{ij} \sigma_\alpha^i \sigma_\alpha^j - \sum_i \gamma^i \sigma_z, \tag{2.42}$$

with parity symmetry, $[H, \Pi_z] = 0$ and $\Pi_z := \otimes_{i=1}^N \sigma_z^i$. Extensive numerical calculations on systems of up to 20 qubits showed that our lower bound (2.25) is always close to the LE as measured by concurrence $L_{i,j}^C$, and typically is exactly equal to it: this is surprising and highlights the tightness of the given lower bound. Note also that whenever parity symmetry is present, the upper and lower bound can be specified as follows:

$$\begin{aligned} \max\left(|Q_{xx}^{ij}|, |Q_{yy}^{ij}|, |Q_{zz}^{ij}|\right) \;&\leq\; L_{i,j}^C \leq \frac{\sqrt{s_+^{ij}} + \sqrt{s_-^{ij}}}{2}, \\ s_\pm^{ij} = \left(1 \pm \langle \sigma_z^i \sigma_z^j \rangle\right)^2 \;&-\; \left(\langle \sigma_z^i \rangle \pm \langle \sigma_z^j \rangle\right)^2 . \end{aligned} \tag{2.43}$$

The fact, that the lower bound is usually tight, can also be derived from the numerical observation that for Hamiltonians of the form (2.42) measurements in the (standard) σ_z-basis ($\mathcal{M} = \mathcal{Z}$) yield in most cases the optimal result. Expanding the ground state in that basis, $|\psi\rangle_0 = \sum c_{i_1 \dots i_N} |i_1 \dots i_N\rangle$, it is straightforward to show that under certain assumptions for the coupling coefficients γ_x and γ_y the ground state energy is minimized if all expansion coefficients $c_{i_1 \dots i_N}$ have the same sign. This guarantees, together with the parity symmetry, that the average entanglement $L_{i,j}^{\mathcal{Z},C}$ for measurements in the standard basis is equal to either the $x - x$ or $y - y$ correlation. To be more precise we distinguish the following cases:

$$(\gamma_x^{ij} - \gamma_y^{ij})(\gamma_x^{ij} + \gamma_y^{ij}) \geq 0 : \quad L_{i,j}^{\mathcal{Z},C} = |\langle \sigma_x^i \sigma_x^j \rangle|, \tag{2.44a}$$

$$(\gamma_x^{ij} - \gamma_y^{ij})(\gamma_x^{ij} + \gamma_y^{ij}) \leq 0 : \quad L_{i,j}^{\mathcal{Z},C} = |\langle \sigma_y^i \sigma_y^j \rangle|, \tag{2.44b}$$

where the conditions refer to all sites i and j of the chain. Most of the prominent spin Hamiltonians studied in literature, like the Heisenberg, XY or XXZ model etc., trivially fulfill one of the conditions (2.44), because their coupling coefficients are site-independent. Hence, measurements in the standard basis would yield localizable quantum correlations that are completely determined by classical correlations.

2.6.2 Ising model

As an illustration, let us now discuss the LE of the Ising model in a transverse magnetic field ($\gamma_\alpha^{ij} = \lambda \delta_{\alpha,x} \delta_{j,i+1}; \gamma^i = 1$ in (2.42)), which has been solved exactly [106] and exhibits a quantum phase transition at $\lambda = 1$. In this case,

the maximal connected correlation function is always given by $Q_{xx}^{i,j}$, which thus yields the best lower bound on LE. Numerical optimization for a finite chain indicates that the standard basis is indeed the optimal one and thus the lower bound is equal to $L_{i,j}^{C}$. We checked analytically, using perturbation theory, that for an infinite chain this numerical result is indeed true. However, for a spin distance $n = |i - j|$ one has to go to n-th order perturbation theory, limiting this analytical treatment to rather small n.
Consequently, we can use exact results for the connected correlation function $Q_{xx}^{i,j}$ [106] to completely characterize the behavior of the LE in the Ising chain. According to (2.43) we can also compute the upper bound $A_{i,i+n}^{C}$ (2.21) exactly.

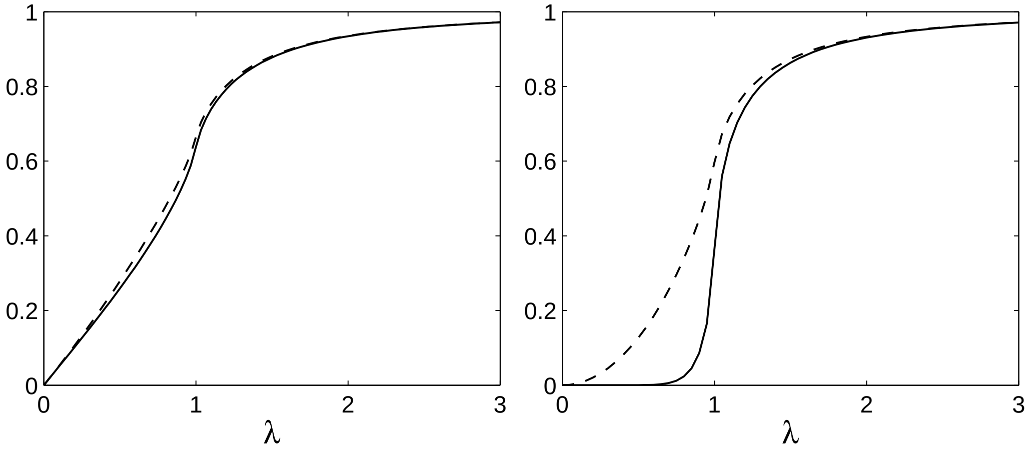

Figure 2.2: Localizable Entanglement L_{ij}^{C} and Correlation function Q_{xx}^{ij} (both solid) and upper bound (2.21) (dashed) as a function of the coupling parameter λ for the infinite Ising chain with spin distance $n = 1$ (left) and $n = 10$ (right).

In Fig. 2.2 we plot the lower bound $Q_{xx}^{i,i+n}$ and the upper bound $A_{i,i+n}^{C}$ as a function of the coupling strength λ for two different distances n. Both bounds are monotonously increasing functions of λ. The difference between them increases with increasing spin distance n. In the region $\lambda < 1$ one finds that the upper bound saturates at a finite value for $n \to \infty$. The reason is that joint measurements can be understood as entanglement swapping that transfers nearest neighbor entanglement to arbitrary distances. For $\lambda > 1$ the lower bound approaches $Q_{xx}^{i,i+n} \to (1 - \lambda^{-2})^{1/4}$ for large n, which implies a diverging entanglement length ξ_E. In the limit $\lambda \to \infty$ the ground state becomes a GHZ-state and the localizable entanglement is maximal. We further note that the first derivative with respect to λ of both bounds (and

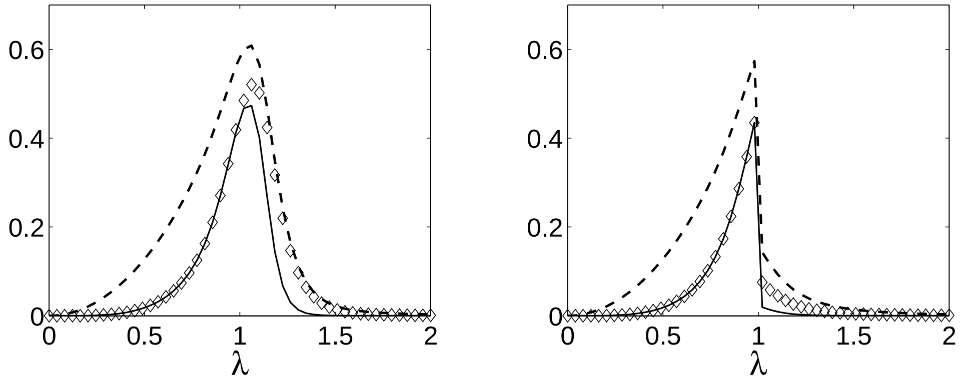

Figure 2.3: Localizable Entanglement $L^C_{i,i+4}$ (diamonds), lower bound $Q^{i,i+4}_{xx}$ (solid) and upper bound $A^C_{i,i+4}$(dashed) as a function of the coupling parameter λ for the ground state of the Ising chain with broken parity symmetry. Left: Parity symmetry is broken by a perturbing magnetic field in the x-direction of strength $h_x = 10^{-3}$. Right: We mimic the behavior in the thermodynamic limit with a finite chain by taking a symmetric superposition of ground and first excited state for $\lambda \geq 1$. Numerics are based on exact diagonalization of a chain with $N = 16$ spins and periodic boundary conditions. Measurements are performed in the σ_z-basis.

hence of LE) diverges at the quantum critical point $\lambda = 1$ for an infinite chain. Following the analysis in [13], we can confirm that not only the concurrence exhibits finite size scaling behavior in the vicinity of the transition point, but also the localizable entanglement and the entanglement of assistance $A^C_{i,i+n}$.

We have also considered a more realistic setup, in which the parity symmetry of the Ising Hamiltonian is broken. This can be done, for instance, by including a perturbing magnetic field in the x direction. Alternatively, we can define a new ground state for the region $\lambda > 1$, by taking a symmetric superposition of the ground and first excited state. This is well justified for long chains $N \gg 1$, because the energy gap vanishes like $1/N^2$ for $\lambda > 1$ [107]. Numerically, we are however restricted to rather small systems ($N = 16$). Nevertheless we use this approach because it provides insight in the behavior in the thermodynamic limit. The results for the LE and its bounds are depicted in Fig. 2.3. We see that the entanglement is now maximal in the vicinity of the quantum critical point $\lambda = 1$. Numerics confirm that the location of the maximum approaches the critical point when the chain length is increased [5]. In the thermodynamic limit and with the perturbing field going

---

[5] Note that the maximum of the concurrence of the reduced density operator as studied in [13, 14] is never exactly at the critical point, not even in the thermodynamic limit.

to zero we again expect non-analytical behavior at the critical point.

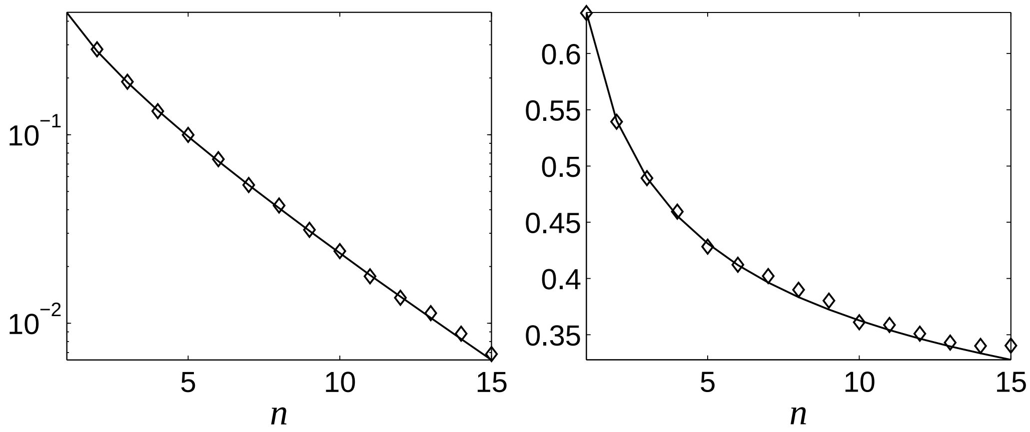

Figure 2.4: Numerical calculation of $L^C_{i,i+n}$(diamonds) for the ground state of the Ising chain in a transverse field ($\gamma^{ij}_\alpha = \lambda\delta_{\alpha,x}\delta_{j,i+1}; \gamma^i = 1$ in (2.42)) as a function of the spin distance n. For comparison we plot the exact result [106] for the correlation function $Q^{i,i+n}_{xx}$. Left: $\lambda = 0.8$, exponential decrease; Right: critical point $\lambda = 1$, power law decrease ($\sim n^{-1/4}$); Numerical parameters (see Sect. IV): $N = 80$, $D = 16$, MC sweeps $M = 20,000$.

Characteristic features of a quantum phase transition can also be found when studying the behavior of LE as a function of the spin distance for fixed λ. This is also a good opportunity to test the numerical method outlined in Sect. IV. In Fig. 2.4 we plot $L^C_{i,i+n}$ and $Q^{i,i+n}_{xx}$ as a function of the spin distance n for a chain with $N = 80$ sites. For $\lambda < 1$, the LE decreases exponentially with n, and the entanglement length is finite. At the quantum critical point $\lambda = 1$, the behavior of the LE changes drastically, because it suddenly decreases as a power law, $L^C_{i,i+n} \sim n^{-1/4}$, thus leading to a diverging entanglement length ξ_E. In Fig. 2.4 we observe that the MC method becomes less accurate at the critical point. As we will see later, one reason is that the statistical error due to entanglement fluctuations becomes rather large at the critical point (see Fig. 2.5). Another (systematic) error might be induced by the single-spin-flip dynamics used to create the trial state. Better results for the critical region could possibly be achieved by applying the Wolff algorithm [108]. Here, a cluster of spins depending on their spin orientation is flipped, which accounts for the formation of domains.

Let us now study whether characteristic features of a quantum phases transition can also be found in the entanglement fluctuations $\delta L^C_{i,i+n}$ (2.19). In Fig. 2.5 we plot $\delta L^C_{i,j}$ for different distances n and chain lengths N as

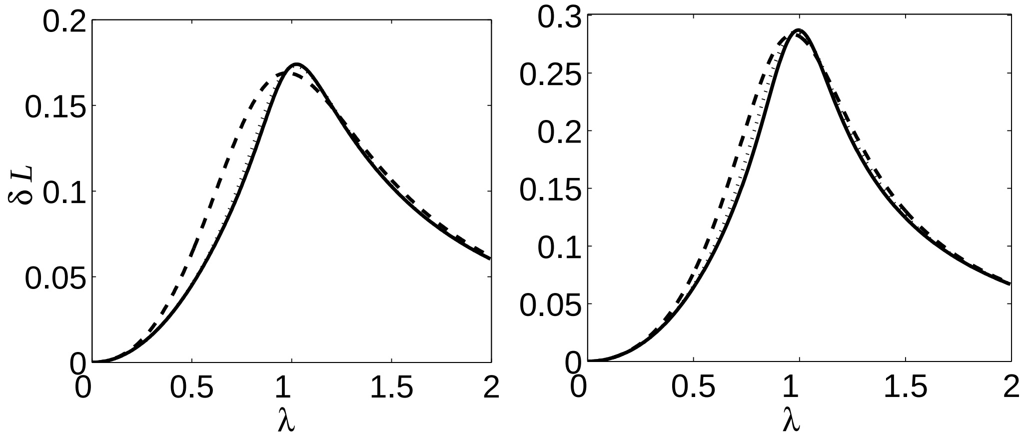

Figure 2.5: Exact calculation of entanglement fluctuations $\delta L^C_{i,i+n}$ (2.19) as a function of the coupling parameter λ for a finite Ising chain in a transverse magnetic field with PBC. Left: distance $n = 1$, $N = 6$ (dashed), $N = 12$ (dotted), $N = 16$ (solid); Right: distance $n = 4$, $N = 9$ (dashed), $N = 12$ (dotted), $N = 16$ (solid).

a function of the coupling λ. The maximum of the fluctuations is always located in the vicinity of the critical point $\lambda = 1$ and gets shifted to larger λ values with increasing N. Thus the increasing entanglement fluctuations reflect very well the increasing complexity of the wavefunction close to the critical region. The location of the maximum λ_m in the thermodynamic limit ($N \longrightarrow \infty$) apparently depends on the distance n of the two spins. For nearest neighbors ($n = 1$) we observe that the maximum of $\delta L^C_{i,i+1}$ is somewhat shifted to the right of the critical point ($\lambda_m \approx 1.025$). For all distances $n > 1$, however, our numerical calculations show that the maximum is positioned at $\lambda < 1$ but becomes asymptotically close to the critical point with increasing n (for $n = 4$ see Fig. 2.5). Furthermore, in Fig. 2.5 we see that the absolute value of the maximum increases with n and becomes comparable with L^C_{ij} itself [6]. The strong fluctuations inherent to the Ising model lead to large statistical errors in the numerical calculation of LE using Monte Carlo (see (2.35)). The errors become even more pronounced for the calculation of the fluctuations. This is the main reason, why we have restricted ourselves here to exact calculations for a small system with PBC. However, we confirmed that the data for $N = 16$ represents the behavior in the large N limit reasonably well and no qualitative changes occur.

---

[6] We note that for $\lambda < 1$ the ratio $\delta L^C_{i,j}/L^C_{i,j}$ can be much larger than one.

2.6.3 XXZ model

Let us now turn to the discussion of another exactly solvable 1D spin system, the so called XXZ model [109]. This model not only appears in condensed matter physics in the context of ferro- or antiferromagnetic materials. Recently it has been shown that it can also effectively describe the physics of ultra cold atoms in a deep optical lattice [36]. The Hamiltonian can be written as

$$H_{\mathrm{XXZ}} = -\sum_i \,[\sigma_x^i\ \sigma_x^{i+1} + \sigma_y^i\ \sigma_y^{i+1} + \Delta\ \sigma_z^i\ \sigma_z^{i+1} + \frac{h}{J}\sigma_z^i\ ], \tag{2.45}$$

where we have introduced two dimensionless parameters, which can be varied independently: the anisotropy Δ and the magnetic field h/J in units of the exchange coupling. The phase diagram of the XXZ model as a function of these two parameters [109] is depicted in Fig. 2.6.

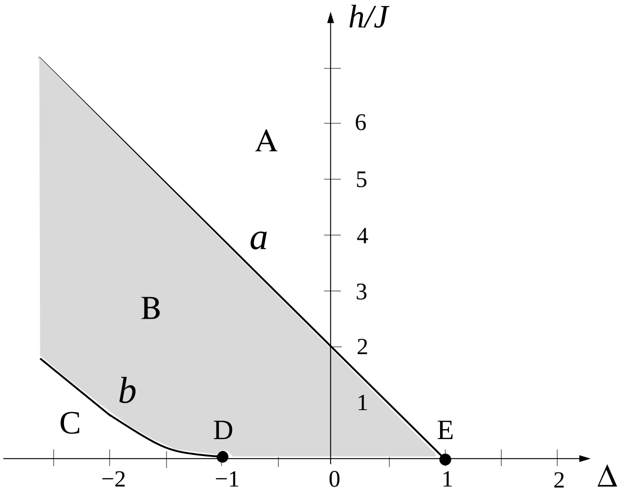

Figure 2.6: Schematic drawing of the phase diagram of the XXZ model (Eq. (2.45)) as a function of the anisotropy Δ and the magnetic field h/J [109]. In regions A and C the ground state has an energy gap, whereas in region B the system becomes gapless (critical). Point E is the ferromagnetic XXX point and point D corresponds to the antiferromagnetic XXX point.

The XXZ model can be solved exactly using the Bethe ansatz [110]. Unfortunately analytical expressions for the correlation functions, which would yield lower bounds for LE, have only been worked out in special cases. E.g. for the antiferromagnetic XXX model in a magnetic field (line of constant $\Delta = -1$ in Fig. 2.6) analytical solutions for the correlations are summarized in [79]. Numerics on a finite chain of up to 14 spins show that again measurements in the σ_z-basis appear to be optimal. Using the result (2.44a) this implies that $L^C_{i,i+n} = \langle\sigma^i_x\sigma^{i+n}_x\rangle$. Hence the bounds given in [79] are tight. In particular this means that the entanglement length is zero for $h/J > 4$, and infinite for $h/J \leq 4$.

Let us now explore other regions of the phasediagram in more detail. In particular, we are interested in finding characteristic features in the LE at the quantum phase transitions indicated by the lines a and b in Fig. 2.6. For this purpose we calculate in the following the LE (for fixed n) numerically, using exact diagonalization, as a function of the two parameters Δ and h/J.

LE as a function of the magnetic field h/J

In Fig. 2.7 we plot the nearest-neighbor entanglement $L^C_{i,i+1}$ and the lower bounds $Q^{i,i+1}_{xx}$ and $Q^{i,i+1}_{zz}$ as a function of the field h/J for fixed $\Delta = 0.5$. We find that $L^C_{i,i+n} = \langle\sigma^i_x\sigma^{i+n}_x\rangle$. This result follows from Eq. (2.44a) and our numerical observation, that the σ_z-basis appears to be optimal in the entire half space $\Delta \geq -1$. At the critical point the LE becomes zero, because the ground state is given by a product state. Note that this phase transition (indicated by line a in Fig. 2.6) is sharp even for finite systems, since it is due to level crossing [109].

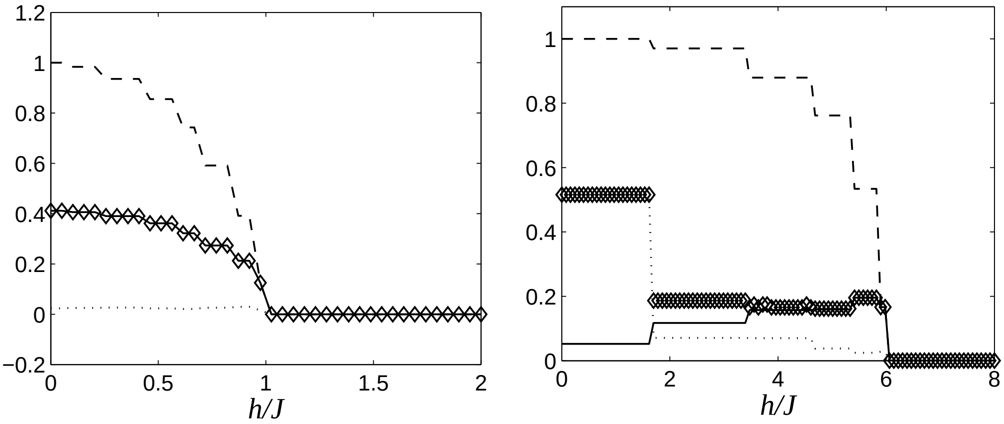

Figure 2.7: Calculation of the localizable entanglement $L^C_{i,i+n}$ (diamonds), the upper bound given by the EoA (2.21) (dashed) and the lower bounds Q^{ii+n}_{xx} (solid) and Q^{ii+n}_{zz} (dotted) as a function of the field h/J for the ground state of the XXZ model (2.45). The numerical calculation is performed using exact diagonalization of a chain with $N = 16$ sites and PBC. The distance of the two spins is $n = 4$ sites; Up: $\Delta = 0.5$; Down: $\Delta = -2$;

We now investigate the region $\Delta < -1$, which contains a second quantum phase transition (indicated by line b in Fig. 2.6). The dependence of the LE and its bounds on the magnetic field for fixed $\Delta = -2$ is depicted in Fig. 2.7. We again observe a sharp phase transition at $h/J \approx 6$, when the system enters the unentangled phase A (Fig. 2.6). At $h/J \approx 1.6$ the LE experiences a sudden drop-off. However, it remains to be checked, whether this step is due to finite size effects or a characteristic feature of a quantum phase transition. Note that for $h/J \lesssim 1.6$ we obtain that $L^C_{i,j} = Q^{ij}_{zz}$. This feature can be understood by considering the limiting case of zero field and $\Delta \to -\infty$. There, the Hamiltonian H_{XXZ} commutes with the parity operator in x-direction, $\Pi_x = \bigotimes_{i=1}^N \sigma^i_x$, and the (doubly degenerate) ground state for even N is given by $|\psi\rangle = 1/\sqrt{2}\,(|0101...01\rangle \pm |1010...10\rangle)$. After suitable projective measurements in the x-direction these states reduce to maximally entangled Bell states $|\Psi^\pm\rangle = 1/\sqrt{2}\,(|01\rangle \pm |10\rangle)$. Hence in this limit $L^C_{i,j} = Q^{ij}_{zz} \to 1$ and the σ_x-basis turns out to be the optimal one. This line of reasoning strictly holds only in the limit $\Delta \to -\infty$, but can qualitatively be extended to the whole region C (Fig. 2.6).
For $h/J \gtrsim 1.6$ we find the interesting feature that the LE is not exactly equal to the maximum correlation function [Fig. 2.7]. Note also that in this region the maximum correlation function changes from Q^{ij}_{zz} to Q^{ij}_{xx}. When approaching the critical point $h/J \approx 6$ the standard basis becomes close to optimal again and $L^C_{i,j} \approx Q^{ij}_{xx}$.
In the following we have a closer look on the phase transition between the regions B and C in Fig. 2.6.

LE as a function of the anisotropy Δ

We consider the case of zero magnetic field and study the LE as a function of Δ in the vicinity of the antiferromagnetic XXX point. At the critical point $\Delta = -1$ the ground state undergoes a Kosterlitz-Thouless [18] quantum phase transition. In Fig. 2.8 we have calculated numerically the localizable entanglement $L^C_{i,i+1}$ for nearest neighbors and the corresponding lower bounds $Q^{i,i+1}_{xx}$ and $Q^{i,i+1}_{zz}$.

One sees that $L^C_{i,i+1}$ is equal to the maximum correlation function. However, at the critical point the maximum correlation function changes, due to the crossing of $Q^{i,i+1}_{xx}$ and $Q^{i,i+1}_{zz}$, thus leading to a cusp in the LE. Hence the quantum phase transition is characterized by a discontinuity in the first derivative of $L^C_{i,i+1}$. This result is remarkable, because for this Kosterlitz-Thouless transtion the ground state energy (i.e nearest neighbor correlation functions) and all of its derivatives are continuous [111]. Also the concurrence of the reduced density matrix $\rho_{i,i+1}$ and its derivatives are continuous

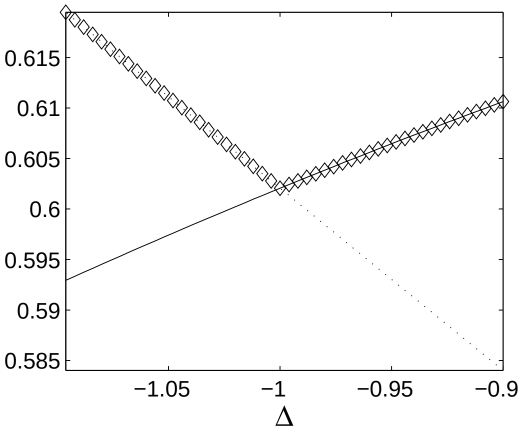

Figure 2.8: Calculation of $L^C_{i,i+1}$ (diamonds) and the lower bounds $Q^{i,i+1}_{xx}$ (solid) and $Q^{i,i+1}_{zz}$ (dotted) as a function of the anisotropy Δ for the XXZ model (2.45) with zero field h/J. At the critical point $\Delta = -1$ the LE exhibits a cusp, in contrast to the monotonic behavior of the correlation functions. The calculation is performed using exact diagonalization and numerical optimization for a chain of length $N = 10$ with periodic boundary conditions.

[112, 113], which is not very surprising, because the concurrence is a function of one-particle and two-particle correlation functions. We further note that, according to our numerical analysis the reason for the cusp in $L^C_{i,i+1}$ is that the optimal measurement basis changes at the critical point abruptly from the σ_z- to the σ_x-basis.

So far this is a purely numerical finding for a finite dimensional system. However, given that the average entanglement can be maximized by applying the same unitary transformation on all spins, one can rigorously show that indeed a cusp in the LE must occur exactly at the critical point and independently of the size N. The argument goes as follows: At the antiferromagnetic XXX point the Hamiltonian (2.45) possesses $SU(2)$ symmetry. This means that any measurement basis yields the same LE. In particular, we know from (2.44a) that for measurements in the standard basis the LE is equal to the correlation function $Q^{i,i+1}_{xx}$. At the critical point we thus have: $L^C_{i,i+1} = Q^{i,i+1}_{zz} = Q^{i,i+1}_{xx}$. Since connected correlation functions yield a lower bound to $L^C_{i,i+1}$ (see Sect. III) the localizable entanglement $L^C_{i,i+1}$ must exhibit a cusp at the critical point, where $Q^{i,i+1}_{zz}$ and $Q^{i,i+1}_{xx}$ cross.

In summary our discussion of the LE in ground states of various spin-1/2 models has shown in which parameter regimes these systems can be used for e.g. localizing long-range entanglement as indicated by the entanglement length. We have further seen that the study of LE provides a valuable tool for detecting and characterizing quantum phase transitions. To be more specific we find the following features in the LE at the quantum critical point: (i) divergence of the first (or second) derivative of LE with respect to the critical coupling parameter; (ii) divergence of the entanglement length; (iii) maximum of the entanglement fluctuations. In addition our numerical results indicate that the localizable ground state entanglement of spin-1/2 Hamiltonians with two-spin nearest neighbor interactions is typically very well described by the maximum correlation function. We will now see that this observation is not necessarily true for spin-1 systems.

2.7 LE in gapped spin-1 chains

We study the ground state entanglement of the (generalized) spin-1 antiferromagnetic Heisenberg chain:

$$H_{AF} = \sum_{i=1}^{N-1} \left[\vec{S}_i \cdot \vec{S}_{i+1} - \beta (\vec{S}_i \cdot \vec{S}_{i+1})^2 \right], \tag{2.46}$$

which includes a biquadratic term. In a recent work [38] it has been demonstrated that quantum Hamiltonians of this kind can be implemented with ultra cold atoms trapped in an optical lattice potential.

2.7.1 General considerations

In the Haldane phase ($-1 < \beta < 1$) and in the dimerized phase ($\beta > 1$) the energy spectrum of (2.46) is gapped. Thus both phases are characterized by a finite correlation length. The structure of the dimerized states indicates that the entanglement length in this phase is finite as well. In contrast, at the AKLT [78] point ($\beta = -1/3$), which is in the Haldane phase, the entanglement length diverges [74]. This is one of the intriguing examples, which show that quantum correlations and classical correlations can exhibit completely different scaling behavior. In this context the question arises, whether the complete Haldane phase is characterized by a diverging entanglement length and thus could be clearly distinguished from the dimerized phase? To this end we will study the LE of a further prominent example in the Haldane phase, which exhibits the most natural spin interaction, namely the Heisenberg antiferromagnet (AF) ($\beta = 0$).

The spin-1 Heisenberg AF is interesting also from a different point of view. It has been shown by Haldane [114] that in the case of half-integer spins the spectrum of this model is gapless in the thermodynamic limit, and thus the correlation length of the ground state is infinite. For integer spins, however, an energy gap emerges, resulting in a finite correlation length. It is interesting to study whether a similar connection holds true for the LE and the corresponding entanglement length. In this context the lower bound (2.25) provides already some insight. The predicted infinite correlation length in spin-1/2 systems (with integer $\log_2(2S+1)$) automatically implies a diverging entanglement length. However, in the case of integer spins the correlation length is finite. Hence, the lower bound (2.26) for spin-1 systems leaves the possibility of an infinite entanglement length, which motivates the calculation of LE in this model.

2.7.2 Heisenberg Antiferromagnet

In the case of the spin-1 Heisenberg AF we cannot resort to an analytical solution as for the AKLT, and thus have to rely on numerical methods.
We start our analysis by performing exact diagonalizations for an open chain of up to 10 sites. At the endpoints we couple to $S = 1/2$ spins thus making sure that the system is in the singlet ground state. We are interested in the LE between the endpoints of the chain. Since the end spins are represented by qubits we can still refer to the LE as measured by the concurrence: $L^C_{1,N}$. Our numerical analysis shows that the optimal measurement basis is given by the same local unitary transformation:

$$U = \frac{1}{\sqrt{2}} \begin{bmatrix} 1 & 0 & 1 \\ 0 & \sqrt{2} & 0 \\ -1 & 0 & 1 \end{bmatrix} , \qquad (2.47)$$

as for the AKLT. This strategy produces a maximally entangled state between the end spins ($L^C_{1,N} = 1$). This numerical finding has later been confirmed analytically by Venuti and Roncaglia [99] using symmetry considerations. This surprising result can be understood from the analytical study of the AKLT model in [74]. In a singlet valence bond picture measurements in the basis (2.47) can be interpreted as Bell measurements in the symmetric subspace of two (virtual) qubits, which leads to entanglement swapping.

Let us now investigate, whether this effect is just a numerical artifact due to the coupling to qubits at the endpoints [7]. For this purpose we apply our numerical method outlined earlier. The LE in its variant $L^{E_E}_{ij}$ (see (2.3))

---

[7] The coupling to qubits at the chain ends can indeed have significant impact on the structure of the ground state wavefunction. For instance, it has been predicted that for such a system the dimerized phase would exhibit a diverging entanglement length [99]

is computed for a chain with PBC and a large number of sites ($N = 80$). We have chosen PBC in order to lift the degeneracy of the ground state

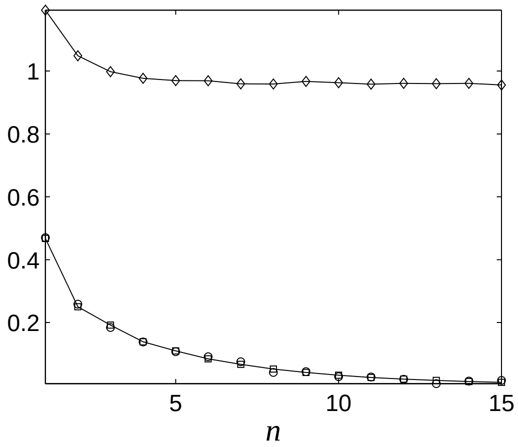

Figure 2.9: Calculation of $L^{E_E}_{i,i+n}$ (diamonds) for the ground state of the antiferromagnetic spin-1 Heisenberg chain with $N = 80$ sites as a function of the spin distance n. For comparison we plot the correlation function $Q^{i,i+n}_{xx}$ computed directly from the MPS (squares) and using Monte Carlo (circles). Numerical parameters: Dimension of MPS matrices $D = 16$, MC sweeps $M = 20,000$.

in the thermodynamic limit. In Fig. 2.9 we see that the LE saturates at a finite value $L^{E_E}_{i,i+n} \rightarrow 0.960 \pm 0.003$ for large n, whereas the correlations decrease exponentially. This demonstrates that the ground state of the antiferromagnetic spin-1 Heisenberg chain could be used to distribute EPR-like entanglement over arbitrary distances by performing local operations on the intermediate spins. As mentioned earlier this result might be particularly interesting in the context of quantum repeaters.

Let us now come back to Haldane's result for the Heisenberg AF stated in the beginning of this section. Our numerical study of the spin-1 case might give a first indication that, unlike the correlation length, the entanglement length is infinite for both half-integer and integer spins.

2.7.3 Connection of LE to hidden order and many-body correlation functions

At this point it is appropriate to comment on a possible connection between LE and many-body correlation functions, which might detect the presence of (hidden) long range order in the system. Our numerical results show that the ground state of the spin-1 Heisenberg AF exhibits long range order in terms of the localizable entanglement, which is not reflected by two-body correlation functions. However, one can define a multi-particle correlation function, the so called *string order correlation function* [115], which detects this *hidden order* in the ground state. The string order correlation function has been argued to be of topological nature and is defined as

$$Q_{so}^{i,i+n} = \langle S_z^i \left[\otimes_{k=i+1}^{i+n-1} R_k \right] \otimes S_z^{i+n} \rangle, \tag{2.48}$$

with $R_k = \exp\left(i\pi S_z^k\right)$. A non-vanishing *string order parameter*, $\xi_{so} := \lim_{n\to\infty} Q_{so}^{i,i+n}$, indicates the presence of long range (hidden) order. As an obvious generalization of the string order correlation function to arbitrary models, let us define a connected version in a variational way. Consider the set of all observables $\{\hat{O}\}$ with bounded spectrum $-\mathbb{1} \leq \hat{O} \leq \mathbb{1}$. We define the *connected string order correlation function* $Q_{cso}^{i,i+n}$ (and the related parameter ξ_{cso}) for a given translational invariant state as

$$Q_{cso}^{i,i+n} = \max_{-\mathbb{1} \leq \hat{O}_1, \hat{O}_2 \leq \mathbb{1}} \langle \hat{O}_1^i \left[\otimes_{k=i+1}^{i+n-1} \hat{O}_2^k \right] \hat{O}_1^{i+n} \rangle_c. \tag{2.49}$$

Here $\langle A_1 A_2 \ldots A_n \rangle_c$ denotes the connected n-point correlation function, which can be defined in a recursive way:

$$\begin{aligned}
\langle A_1 \rangle &= \langle A_1 \rangle_c, && (2.50)\\
\langle A_1 A_2 \rangle &= \langle A_1 \rangle_c \langle A_2 \rangle_c + \langle A_1 A_2 \rangle_c, && (2.51)\\
\langle A_1 A_2 A_3 \rangle &= \langle A_1 \rangle_c \langle A_2 \rangle_c \langle A_3 \rangle_c + \langle A_1 \rangle_c \langle A_2 A_3 \rangle_c && (2.52)\\
&+ \langle A_2 \rangle_c \langle A_1 A_3 \rangle_c + \langle A_3 \rangle_c \langle A_1 A_2 \rangle_c \\
&+ \langle A_1 A_2 A_3 \rangle_c, \\
&\vdots
\end{aligned}$$

Note that the connected part assures that $Q_{cso}^{i,i+n}$ measures a nonlocal correlation, and that the string order parameter of the AKLT-ground state is indeed recovered by this definition.

It has been verified numerically that ξ_{so} is finite for the ground state of the spin-1 Heisenberg AF. This fact can rigorously be proven for the related AKLT-ground state [78]. For this state it was further shown that the LE saturates as well with the spin distance n [74]. Hence one might expect a connection between the existence of long range order in the entanglement and long range order indicated by the string order parameter. However, one can find examples for which this connection does not hold.

For instance, in [74] it has been shown that already an infinitesimal deformation of the AKLT model leads to an exponentially decreasing LE, whereas

ξ_{cso} stays finite. On the other hand, ground states exist that exhibit a diverging entanglement length but vanishing ξ_{cso}. A simple example can be found in the class of MPS (2.30) defined on qubits ($d = 2$) and with qubit bonds ($D = 2$). Note that all these MPS are guaranteed to be ground states of some local Hamiltonians. Furthermore, for MPS with qubit bonds the string order parameter and the LE can easily be computed analytically (see [74] and Appendix B). In particular, let us study the translationally invariant MPS defined by the matrices

$$A^1 = \sigma_z + \sigma_y \qquad A^2 = \sigma_z - i\mathbb{1}. \tag{2.53}$$

The entanglement length can easily be proven to be infinite. A necessary condition for ξ_{cso} to be nonzero is that there exists a unitary operator $\hat{O}_2$ for which the largest eigenvalue of $E_{\hat{O}_2}$ has the same magnitude as the maximal eigenvalue of $E_{\mathbb{1}}$ (Appendix B). For the example given, this is impossible, hence providing an example of a ground state with a diverging entanglement length but no long range hidden order.

This discussion shows that in general long range order in LE is not directly related to string-order. However, it is important to note that for real pure (qubit) states (e.g. ground states of real Hamiltonians) the LE as measured by the concurrence, $L^C_{i,j}$, can always be written as a complicated multi-partite correlation function (see also [99]). Out of an exponential number of possibilities LE determines the maximum correlation function, which, in addition, has a clear meaning in terms of an entanglement measure. In this sense the definition of LE determines the correlation function, which detects the sort of long range order, that is suitable for localization of entanglement.

2.7.4 AKLT model: Study of thermal state entanglement

Next we are interested in the entanglement properties of the Heisenberg AF at finite temperature. For numerical reasons we have to choose the AKLT model instead, because it can be approximated more efficiently in terms of MPS. We expect that our findings are also representative for the Heisenberg AF. In order to decrease computation time even further we are using OBC (see 2.5.2).

Let us first discuss the optimal measurement strategy for LE. We point out, that with OBC the ground state of the AKLT is four-fold degenerate [8]. Thus for $T \to 0$ the density matrix is an equal mixture of these four states,

---

[8] We note that the degeneracy in the case of OBC could be lifted by placing $S = 1/2$ spins at the ends. For technical reasons we do not consider this situation.

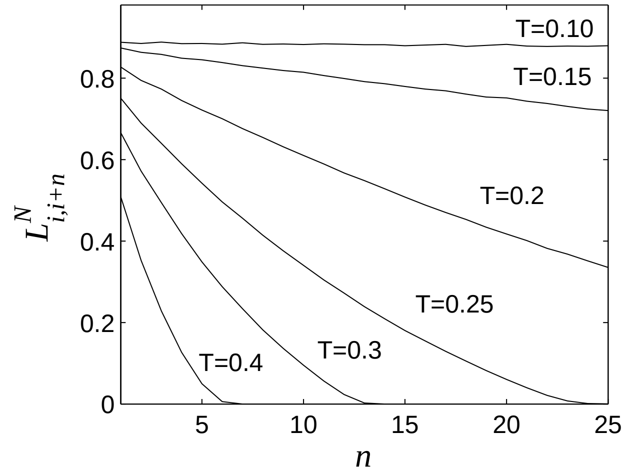

Figure 2.10: Calculation of the LE as given by $L^N_{i,i+n}$ for thermal states of the AKLT model as a function of the spin distance n and for various temperatures T. We have chosen a chain with OBC and $N = 50$ sites. We note that almost identical data can be obtained for $N = 20$, indicating that our results are already close to the thermodynamic limit. The thermal states are computed numerically based on the MPS method [102] with maximum bond size $D = 10$. For the computation of LE we perform $M = 5,000$ Monte Carlo sweeps.

which strongly reduces the LE compared to e.g. the singlet ground state studied in [74]. On the other hand it is known that the degeneracy results only from the end spins of the chain. Thus, one can strongly reduce this boundary effect by choosing the two spins, i and $i + n$, to be far away from the boundaries. For this situation we found that the optimal measurement scheme for LE is given by measurements in the U-basis (2.47) on the spins between sites i and $i + n$, and in the standard basis everywhere else. This result is not very surprising in terms of the valence bond picture in [74]. Entanglement swapping is only needed between the two spins of interest, whereas the effect of the degeneracy can be minimized by measuring the outer spins in the standard basis. Using this strategy we plot in Fig. 2.10 the LE, as given by $L^N_{i,i+n}$, depending on the spin distance n for various temperatures T. The temperatures are chosen to be of the order of the energy gap [116].

The data indicates an exponential increase of the entanglement length $\xi_E \sim e^{\alpha/T}$ with $\alpha \approx 0.8$, thus leading smoothly to an infinite entanglement length at zero temperature. This behavior is not unexpected for a 1D system from the perspective of the Mermin-Wagner theorem [117]. However, it is not clear whether this theorem is really applicable to phase transitions in terms of LE. It is more inspiring to treat this problem on the basis of *projected entangled-pair states* [44]. In this picture a finite temperature phase transition for LE could possibly occur for two or more dimensions. We note that recently such a transition has been shown to exist for 3D cluster states [83]. Finally we would like to point out that, although the entanglement length of the AKLT model is finite for $T > 0$, it can still be considerably large for sufficiently low temperatures $T \lesssim 0.2$. Thus for practical purposes this system might still be useful, e.g. for quantum repeater setups.

Chapter 3

Cooling of atoms in optical lattices

Ultra cold atoms stored in optical lattices can be controlled and manipulated with a very high degree of precision and flexibility. This places them among the most promising candidates for implementing quantum computations [46, 118, 119, 47, 44] and quantum simulations of certain classes of quantum many–body systems [33, 34, 35, 36, 37, 38, 39, 40, 41, 42]. Quantum simulation would allow us to understand physical properties of certain materials at low temperatures that so far have eluded a theoretical description or numerical simulation. However, both quantum simulation and quantum computation with this system face a crucial problem: the temperature in current experiments is too high. In this chapter we propose and analyze several methods to decrease the temperature of atoms in optical lattices and thus to reach the interesting regimes in quantum simulations, as well as to prepare defect–free registers for quantum computation.

So far, several experimental groups have been able to load bosonic or fermionic atoms in optical lattices and reach the strong interaction regime [24, 25, 26, 27, 28, 29, 30, 31, 32]. The analysis of experiments in the Tonks gas regime indicates a temperature of the order of the width of the lowest Bloch band [25], and for a Mott Insulator (MI) a temperature of the order of the on-site interaction energy has been reported [43, 26]. For fermions one observes temperatures of the order of the Fermi energy [120, 121, 122]. Those temperatures severely restrict the physical phenomena that can be observed and the quantum information tasks that can be carried out with these lattices.

One may think of several ways of cooling atoms in optical lattices. Since the process of loading atoms into the lattice may lead to additional heating [123] we focus here on methods that operate once the lattice potential has been raised. For example, one may sympathetically cool the atoms in the lattice using a second Bose–Einstein condensate [35, 124]. A completely different approach is the *filtering* scheme of Rabl *et al.* [45]. It operates in the no-tunnelling regime, transferring atoms between optical lattices so as to create a configuration with one atom per site. Such a loading scheme can, however, originate holes due to imperfections in the original cloud. In this thesis we propose several cooling schemes, which overcome the limitations of filtering. The main results of this chapter can be summarized as follows:

(i) We discuss realistic values for temperature and entropy in current experimental setups.

(ii) We develop a fermionization procedure for the Bose-Hubbard model, which maps one species of interacting bosons into two species of non-interacting fermions. This approach is valid for a deep optical lattice and thermal states at low temperatures. It allows us to compute important observables, such as entropy or density, analytically.

(iii) We define appropriate figures of merit based on the entropy of thermal states in order to quantify the cooling performance of our schemes.

(iv) We analyze the cooling efficiency of the original filtering scheme [45] in the presence of a harmonic trap. We show that the residual defects (holes) are preferably located at the borders of the cloud and result in a considerable amount of entropy [64].

(v) In order to overcome the limitations of filtering we propose, analyze and compare novel cooling schemes which aim at cooling atoms to the ground state of a deep optical lattice. The first set of schemes uses discrete operations to make atoms in different sites interact, thus concentrating the entropy on some atoms which are then expelled from the lattice. Due to the similarity with quantum information processing, we term this kind of methods *algorithmic cooling* [1]. The second set of cooling methods combines filtering with either particle hopping or evaporative cooling techniques. We provide a complete analytical and numerical description of our protocols. Attainable temperatures are predicted to be low enough for practical purposes. We note that our cooling protocols do not require single–site addressing and consider the residual harmonic confinement present in current experiments. Although we will be mostly analyzing their effects on bosonic atoms, they can also be trivially generalized to fermions.

---

[1] Note that our concept of *algorithmic cooling of atoms* has to be clearly distinguished from *algorithmic cooling of spins* which is a novel technique that allows to create highly polarized ensembles of spins in the context of NMR experiments, see e.g. P. O. Boykin, T. Mor, V. Roychowdhury, F. Vatan, and R. Vrijen, Proc. Natl. Acad. Sci. USA **99**, 3388 (2002).

(vi) We design algorithmic protocols that very efficiently remove all residual defects after filtering, thus producing an ensemble of perfect registers for quantum computing [44]. We also propose how to create pointer atoms at the endpoints of these registers and show how these pointers can be used to tailor the register to a specific length.

(v) Since filtering is an important ingredient of all our protocols, we propose two new physical realizations of filtering. The first one is much faster than previous proposals [45, 125]. The second one can be implemented rather easily and operates in a continuous way.

In Appendix D we present a detailed description of the numerical method that we use in order to simulate classically correlated many-body states.

3.1 Physical system

3.1.1 Bose-Hubbard model

We consider a gas of ultra-cold bosonic atoms which have been loaded into a three dimensional (3D) optical lattice. This lattice is created by six laser beams of wave vector $k = 2\pi/\lambda$ propagating along three orthogonal directions. If the laser light is off-resonant with any atomic transition, the AC Stark effect induces a periodic potential on the atoms of the form:

$$V(x, y, z) = V_{0x}\sin^2(2kx) + V_{0y}\sin^2(2ky) + V_{0z}\sin^2(2kz), \tag{3.1}$$

with a strength or "lattice depth" V_0 proportional to the dynamic atomic polarizability and the laser intensity. The Gaussian intensity profile of the laser beams creates an additional harmonic confinement, which is typically much stronger than any magnetic confinement [24].

In the following we will mostly be concerned with one-dimensional (1D) lattices. In other words we will assume that the lattice potential is so strong along two directions, $V_{0y}, V_{0z} \gg V_{0x}$ that tunnelling is only allowed along the third one. We will also assume that the confinement along all directions is still much stronger than the atomic interaction strength. Under these conditions, the atoms can be described using a 1D single-band Bose-Hubbard model (BHM) [126], which for a lattice of length L reads

$$H_{\rm BH} = \sum_{k=-L/2}^{L/2-1} \left[-J(a_k^\dagger a_{k+1} + h.c.) + \frac{U}{2} n_k(n_k - 1) + bk^2 n_k \right]. \tag{3.2}$$

The parameter J denotes the hopping matrix element between two adjacent sites, U is the on-site interaction energy between two atoms and the energy b

accounts for the strength of the harmonic confinement. Second quantization operators $a_k^\dagger$ and a_k create and annihilate, respectively, a particle on site k, and $n_k = a_k^\dagger a_k$ is the occupation number operator. Since the tunnelling rate decreases exponentially with the trapping strength, V_0, while the on-site interaction U remains almost constant [126], we have adopted this last value as the unit of energy for our work. By increasing the intensity of the lattice laser beams one can decrease the hopping rate J until the interaction energy U dominates the dynamics. At $U/zJ \approx 5.8$, with z being the number of nearest neighbors, the system undergoes a quantum phase transition from a superfluid (SF) to a Mott insulator (MI) [126]. This phenomenon was first observed by Greiner et al. [24] in 2002. In the SF regime particles are delocalized over all lattice sites. In 1D without harmonic trap the SF ground state reads:

$$|\psi_0\rangle_{\mathrm{SF}} \propto \left(\sum_{k=-L/2}^{L/2-1} a_k^\dagger \right)^{\otimes N} |0\rangle, \tag{3.3}$$

where N is the particle number. In the MI regime particles are localized at individual lattice sites:

$$|\psi_0\rangle_{\mathrm{MI}} \propto \bigotimes_{k=-L/2}^{L/2-1} \left(a_k^\dagger \right)^{\nu} |0\rangle. \tag{3.4}$$

The parameter $\nu = N/L$ is called the filling factor of the lattice. For very shallow harmonic traps, negligible tunnelling $J/U \ll 1$ and $N < L$ the ground state is a MI with $\nu = 1$, which is centered around the bottom of the trap. In the Fock basis this MI state can be written as:

$$|\psi_0\rangle_{\mathrm{MI}} = |0_{L/2} \ldots 0_{-N/2-1} 1_{-N/2} \ldots 1_{N/2-1} 0_{N/2} \ldots 0_{L/2-1}\rangle. \tag{3.5}$$

This state will be the target ground state for all our cooling schemes.

3.1.2 Initial states

Throughout this chapter we will work with 1D thermal states in the grand canonical ensemble, which are characterized by two parameters: the temperature $kT = 1/\beta$ and the chemical potential μ. We are particularly interested in the no-tunnelling limit [2], $J \to 0$. In this limit the Hamiltonian (3.2) becomes diagonal in the Fock basis of independent lattice sites:

---

[2] The condition for the no-tunnelling regime in the presence of a harmonic trap is given by $|J/(bN)|^2 \ll 1$, i.e. the hopping matrix element is much smaller than the average energy spacing between single particle states located at the borders of the trap. If desired one can also demand $|J/b|^2 \ll 1$, which ensures that single particle eigenfunctions even at the bottom of the trap are localized on individual lattice wells [127].

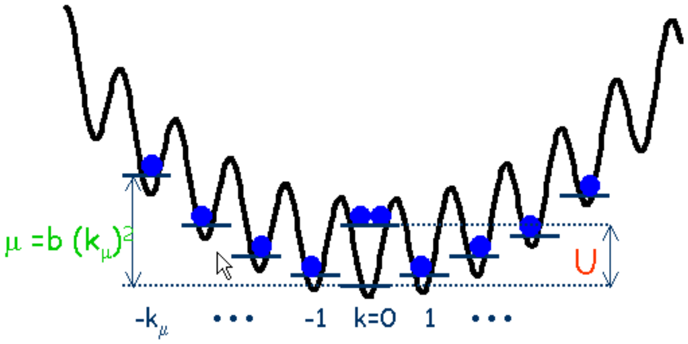

Figure 3.1: Illustration of important energy scales for bosonic atoms in an optical lattice in the no-tunnelling regime: on-site interaction energy U, chemical potential μ, and harmonic confinement $V_{ho} = bk^2$. The characteristic size of the atomic cloud is given by $k_\mu = \sqrt{\mu/b}$.

$\{|n_{-L/2} \ldots n_0 \ldots n_{L/2-1}\rangle\}$ and the density matrix becomes a tensor product of thermal states for each lattice site,

$$\rho = \frac{1}{\Theta} e^{-\beta(H_{BH} - \mu N)} = \bigotimes_{k=-L/2}^{L/2-1} \rho_k. \tag{3.6}$$

This simplifies calculations considerably and for instance the von-Neumann entropy can be written as the sum over single–site entropies

$$S(\rho) = \mathrm{tr}(\rho \log_2 \rho) = \sum_k S(\rho_k). \tag{3.7}$$

Let us now study thermal states of the form (3.6) in more detail. All relevant energy scales, which determine the structure of this state, are depicted in Fig. 3.1. Since we are interested in cooling it is of central importance to know the typical temperature (or entropy) and chemical potential (or particle number) in current experiments. The analysis of recent experiments in the Tonks gas regime [25] implies an entropy per particle $s := S/N \approx 1$ [128]. For the MI regime a temperature on the order of the on-site interaction energy U has been reported [43, 26]. We will now show that both findings are consistent with each other. First we note that the particle number in a 1D tube of a 3D lattice as in [24] typically ranges between $N = 10$ and $N = 130$, with an average value of about $N = 65$. For a typical trap strength, $b = U/370$, we have constructed a thermal state in the no-tunnelling regime which yields the expectation values $N = 65$ and $s = 1$. The resulting density distribution is depicted in Fig. 3.2a. The inverse temperature is given by

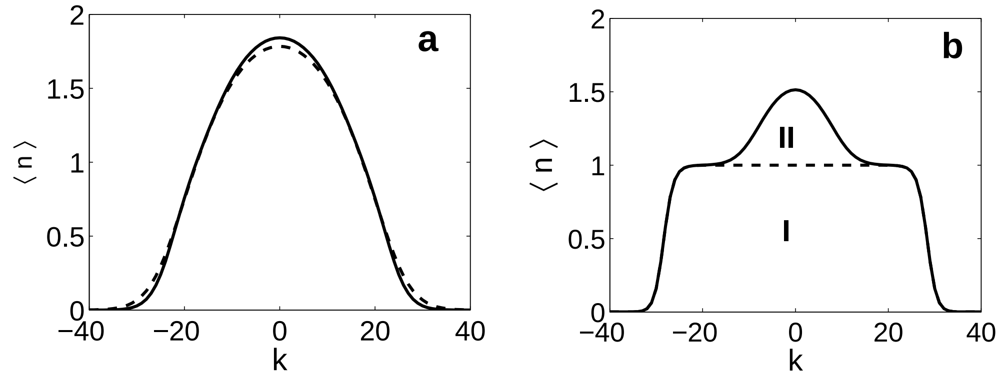

Figure 3.2: (a) Density distribution of two thermal states with equal Rényi entropy $S_2/N = 0.82$ ($S/N = 1$ in MI phase) and equal particle number $N = 65$. At hopping rate $J/U = 0$ (solid) the temperature is given by $kT/U = 0.32$ and at $J/U = 0.16$ ($V_0 = 5E_r$) (dashed) one obtains $kT/U = 0.46$. The harmonic confinement is fixed at $U/b = 370$ ($V_0 = 22E_r$ in transverse direction). (b) The separation into two fermionic phases becomes clearly visible in the density profile of a thermal state at low temperatures. Numerical parameters: $J = 0$, $kT/U = 0.072$, $\mu/U = 1$, $U/b = 800$, ($N = 65$, $s = 0.5$).

$\beta U = 3.1$, which is in good agreement with the findings in [43, 26]. Hence, it is reasonable to take a thermal state with $s = 1$ as starting point for testing our cooling schemes later in this chapter.

We have seen that the typical inverse temperature in current experiments is $\beta U \gtrsim 1$. Since our cooling protocols lead to even lower temperatures, we will from now on focus on the *low temperature regime*, $\beta U \gg 1$. Moreover, we will only consider states with at most two particles per site, which puts the constraint $\mu \lesssim 2U - 1/\beta$ on the chemical potential. Such a situation can either be achieved by choosing the harmonic trap shallow enough or by applying an appropriate filtering operation [45].

Effective description in terms of fermions

Under the assumptions $e^{\beta U} \gg 1$ and $\mu - U/2 \gtrsim b + 1/(2\beta)$ we will now show that the density distribution of the initial state (3.6) can be separated into regions that are completely characterized by fermionic distribution functions of the form:

$$f_k(b, \beta, \mu) = \frac{1}{1 + e^{\beta(bk^2 - \mu)}}. \tag{3.8}$$

To be more precise, we want to show the following two features:

(i) for sites at the borders of the density distribution, $bk^2 \gg \mu - U/2 + 1/(2\beta)$, the mean occupation number is given by $\langle n_k \rangle \approx n_{\mathrm{I}}(k)$ with $n_{\mathrm{I}}(k) := f_k(b, \beta, \mu)$.
(ii) In the center of the trap, $bk^2 \ll \mu - U/2 - 1/(2\beta)$, one has: $\langle n_k \rangle \approx 1 + n_{\mathrm{II}}(k)$ with $n_{\mathrm{II}}(k) := f_k(b, \beta, \mu_{\mathrm{II}})$ and effective chemical potential $\mu_{\mathrm{II}} := \mu - U$.

The argument goes as follows. Starting from the thermal state (3.6), with parameters β, μ and b, the grand canonical partition function for site k is given by:

$$\Theta_k = 1 + a\ x_k + b\ x_k^2, \tag{3.9}$$

with $x_k = e^{-\beta b k^2}$, $a = e^{\beta\mu}$ and $b = e^{\beta(2\mu - U)}$. In this notation the probabilities p_k^n of finding n particles at site k can be written as: $p_k^0 = 1/\Theta_k$, $p_k^1 = a\ x/\Theta_k$ and $p_k^2 = b\ x^2/\Theta_k$. For analyzing these functions we split the lattice into a central region and two border regions. For lattice sites at the borders one finds $bx^2 \ll 1, ax$, meaning that the probability for doubly occupied sites becomes negligible: $p_k^2 \ll p_k^0, p_k^1$. The average occupation is thus given by $\langle n_k \rangle \approx p_k^1$, with

$$p_k^1 \approx \frac{ax}{1 + ax} = \frac{1}{1 + e^{\beta(bk^2 - \mu)}}. \tag{3.10}$$

In the crossover region, $bk^2 \approx \mu - U/2$, one obtains a MI phase ($p_k^0, p_k^2 \ll p_k^1 \approx 1$). In the center of the trap one finds a negligible probability for empty sites: $p_k^0 \ll p_k^1, p_k^2$, since $ax, bx^2 \gg 1$. The average population at site k becomes $\langle n_k \rangle = p_k^1 + 2\ p_k^2 \approx 1 + p_k^2$, where

$$p_k^2 \approx \frac{bx^2}{ax + bx^2} = \frac{1}{1 + e^{\beta(bk^2 - (\mu - U))}}. \tag{3.11}$$

This is identical to the fermionic distribution (3.8) with effective chemical potential $\mu - U$. Hence the density distribution in this lattice region can be interpreted as a thermal distribution of hard-core bosons sitting on top of a MI phase with unit filling. Note that this central MI phase is well reproduced by the function $n_{\mathrm{I}}(k)$, which originally has been derived for the border region. As a consequence, the density distribution for the whole lattice can be put in the simple form: $\langle n_k \rangle \approx n_{\mathrm{I}}(k) + n_{\mathrm{II}}(k)$, which corresponds to two fermionic phases I and II, sitting on top of each other [Fig. 3.2b].

The initial density profile can be further characterized by two distinctive points. At sites $\pm k_\mu := \pm\sqrt{\mu/b}$, which correspond to the Fermi levels of phase I, one obtains $\langle n_{\pm k_\mu} \rangle = 1/2$. Hence, k_μ determines the radius of the atomic cloud. Note also that in the case $\mu \approx U$ singly occupied sites around the Fermi levels become degenerate with doubly occupied sites at the center

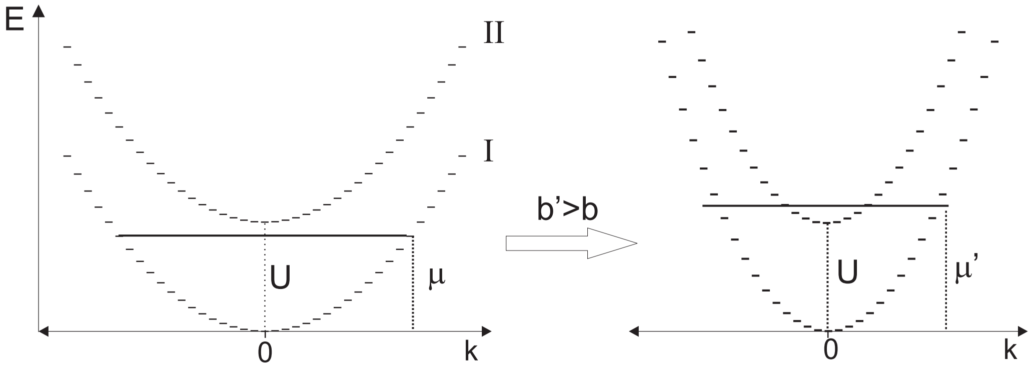

Figure 3.3: Effective description of thermal states in the no-tunnelling limit in terms of independent fermions occupying two energy bands. The dispersion relations are $\varepsilon_{\mathrm{I}} = bk^2$ and $\varepsilon_{\mathrm{II}} = bk^2 + U$, where k denotes the lattice site and U is the interaction energy. Increasing the harmonic trap strength from b to b' increases the chemical potential to μ' so that the population of the upper band becomes energetically favorable. In the bosonic picture this process corresponds to the formation of doubly occupied sites.

of the trap. At the central site ($k = 0$) one finds an average occupation:

$$\langle n_0 \rangle = 1 + \frac{1}{1 + e^{\beta(U-\mu)}}. \tag{3.12}$$

For instance, the value $\langle n_0 \rangle = 3/2$ fixes the chemical potential to be $\mu = U$.

So far we have analyzed the density profile of thermal states and found that it can be well characterized in terms of two species of independent fermions. In Appendix C we derive this fermionic description more rigorously starting directly from the Bose-Hubbard Hamiltonian (3.2). We find that the dynamics at finite J is governed by the effective Hamiltonian:

$$\begin{aligned} \tilde{H} &= -J \sum_k \left(c_k^\dagger c_{k+1} + \sqrt{2} c_k^\dagger d_{k+1} + 2 d_k^\dagger d_{k+1} + \text{H. c.} \right) \\ &+ \sum_k \left[bk^2 c_k^\dagger c_k + (bk^2 + U) d_k^\dagger d_k \right]. \end{aligned} \tag{3.13}$$

Here, the fermionic operators c_k refer to energy band I with dispersion relation $\varepsilon_{\mathrm{I}} = bk^2$ and operators d_k to band II with $\varepsilon_{\mathrm{II}} = bk^2 + U$ [Fig. 3.3]. This effective description in terms of independent fermions is self-consistent as long as the probability of finding a particle–hole pair is negligible, i.e. $\langle c_k c_k^\dagger d_k^\dagger d_k \rangle \approx 0$. We have shown above that for thermal states at low-temperatures and for negligible tunnelling this is indeed fulfilled. The validity of the fermionization for a non-zero tunnelling rate is studied in Fig. 3.4. Tolerating an error of roughly 1% we find that the model is self-consistent up to $J/U \lesssim 0.2$.

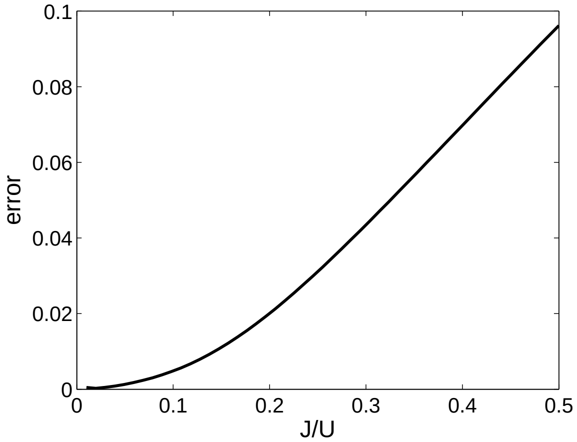

Figure 3.4: Range of validity of the two–species independent fermion model (3.13). For thermal states at $\beta U = 10$ we plot the error $\varepsilon = \sum_k \langle c_k c_k^\dagger d_k^\dagger d_k \rangle / N$ as a function of the hopping rate J for fixed harmonic trap $U/b = 625$ and $\mu/U = 1$.

Numerical computation of thermal states

We have just seen that the effective description in terms of independent fermions fails at large hopping rates. In this regime we resort to a multi-particle description and compute 1D thermal states numerically based on the MPS method proposed in [102]. As an application we can, for instance, estimate how the temperature of a 1D tube changes when passing from the MI to the SF regime. Assuming that the process is thermodynamically adiabatic one obtains the new temperature with the following procedure. We tune the parameters of a thermal state in the SF regime until the expectation values for the entropy and particle number match the corresponding values of the initial thermal state in the MI regime. Let us now consider a realistic example. Starting from a thermal state in the no-tunnelling regime with $s = 1$ and $N = 65$ we have to tune the temperature to $kT = 0.46U = 2.9J$ at $J/U = 0.16$ ($V_0 = 5E_r$) in order to leave s and N unchanged [Fig. 3.2a]. Hence, in the SF regime one faces a substantial temperature of the order of the width of the lowest Bloch band. Note, however, that this is only a lower bound to the true temperature, because our approach does not include any sort of heating processes induced by the adiabatic evolution.

3.1.3 Entropy as figure of merit

We will show below that algorithmic protocols are suited both for ground state cooling and the initialization of quantum registers. The goal in both cases is to create a pure state under the constraint of keeping a large number of particles. Given the fact that our protocols converge to the desired family of states, we can measure the performance of the protocol by computing the mixedness of the state. This mixedness can in turn be quantified using the von–Neumann entropy S (3.7). In some cases, such as for finite hopping J we will not be able to compute the von-Neumann entropy efficiently. We will then refer to the Rényi entropy

$$S_2 = -\log_2(\mathrm{tr}\rho^2), \tag{3.14}$$

which is a lower bound $S_2 \leq S$ and can be evaluated using MPS [Appendix D].

In order to assess the efficiency of a protocol in achieving our objectives we define two figures of merit: (i) The ratio of the entropies *per* particle after and before invoking the protocol, s_f/s_i, quantifies the amount of cooling. (ii) The ratio of the final and initial number of particles, N_f/N_i, quantifies the particle loss induced by the protocol.

Note that these figures of merit can sometimes be misleading and should therefore be applied with care. In the case of ground state cooling the entropy is only a good figure of merit if the state of the system after the cooling protocol, ρ_f, is close to thermal equilibrium. If this is not fulfilled, we compute an effective thermal state, $\rho_f \to \rho_{\mathrm{eff}}$, with the same number of particles, N, and energy, E. This is performed numerically by tuning the chemical potential and temperature of a thermal state ρ_{eff} until the expectation values for particle number and energy coincide with the ones of the original state ρ_f. This procedure can be implemented rather easily in the no-tunnelling regime, in which the density matrix factorizes (3.6). Our figures of merit can then be computed from ρ_{eff}. Given that our system can somehow thermalize, these approach will indeed reflect the properties of our final state. Finally, it is important to point out, that other variables, like energy or temperature, are not very well suited as figures of merit, because they depend crucially on external system parameters like the trap strength.

Let us also note that in the case of quantum registers it can be erroneous to assume that a finite value of the final entropy implies the existence of defects. For example, we will propose a protocol below that generates a state which is an incoherent superposition of defect-free quantum registers with varying length and position. This state has some residual entropy but it is nevertheless perfect for quantum information processing.

3.1.4 Basic operations

All our cooling protocols rely on a set of translationally invariant quantum operations that can be realized in current experiments with optical lattices. They require at most three internal states of the atoms, which will be denoted by $|a\rangle, |b\rangle$ and $|c\rangle$. The operations are:

(i) Particle transfer: Depending on the occupation numbers, an integer number of particles is transferred coherently between internal states $|a\rangle$ and $|b\rangle$. This process can be described by the unitary operation

$$U_{m,n}^{m+x,n-x} : |m,n\rangle \leftrightarrow |m+x,n-x\rangle, \qquad (3.15)$$

where x is an integer and $|m,n\rangle$ are Fock states with m and n atoms in internal states $|a\rangle$ and $|b\rangle$, respectively. Note that for this unitary operator it holds $U_{m,n}^{m+x,n-x} = U_{m+x,n-x}^{m,n}$. Certain operations, like $U_{2,0}^{0,2}$ or $U_{1,0}^{0,1}$, have already been demonstrated experimentally in an entanglement interferometer [129]. We will also consider generalizations of (3.15) that involve three internal levels. For instance, the operation $U_{1,1,0}^{0,0,2}$ transfers two particles to the formerly empty level $|c\rangle$, given that levels $|a\rangle$ and $|b\rangle$ are both singly occupied.

(ii) Lattice shifts: We denote by S_x the operations which shift the $|b\rangle$ lattice x steps to the right. For example, S_{-1} transforms the state $\otimes_k |m_k, n_k\rangle_k$ into $\otimes_k |m_k, n_{k+1}\rangle_k$. This operation can be realized in state-dependent lattices by adjusting the intensity and polarization of the laser beams [46, 118, 119, 47, 130].

(iii) Merging and splitting of lattice sites: Making use of superlattices [131] one can either merge adjacent lattice wells or split a single site into a pair of two sites.

(iv) Emptying sites: All atoms in internal state $|b\rangle$ are removed from the system. We denote this operation by E_b. It transforms the state $\otimes_k |m_k, n_k\rangle_k$ into $\otimes_k |m_k, 0\rangle_k$. Experimentally, this can be achieved either by switching off the lattice potential acting on $|b\rangle$ or by coupling this state resonantly to an untrapped state.

(v) Filtering: This means particle transfer operations of the form $U_{m,0}^{M,m-M}$, followed by E_b, for all $m > M$. After tracing out the subsystem $|b\rangle$, the filter operation is described by a completely positive map acting solely on atoms in state $|a\rangle$:

$$F_M[\rho] : \sum_{n,m} \rho_{n,m} |n\rangle\langle m| \to \sum_{n,m \le M} \rho_{n,m} |n\rangle\langle m| + \sum_{n>M} \rho_{n,n} |M\rangle\langle M|. \qquad (3.16)$$

The first proposal for a coherent implementation of the operation F_1 [Fig. 3.5] appeared in Ref. [45]. More recently, a scheme based on resonant control of interaction driven spin oscillations has been put forward [125].

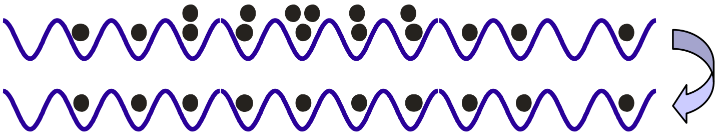

Figure 3.5: Illustration of the filtering operation F_1 which aims at producing a uniform filling of one atom per site. Defects arising from holes cannot be corrected.

3.2 Filtering

We now study the filtering operation F_1 in Eq. (3.16) in more detail. This operation is especially relevant for cooling because it produces a state close to the ground state of the MI regime. Thus, it can serve as a benchmark which has to be beaten by alternative cooling schemes. In this section we provide a theoretical analysis of filtering and discuss the conditions to reach optimal cooling efficiency. We then propose two physical realizations of filtering.

3.2.1 Theory

In Fig. 3.6 we have depicted the particle and entropy distributions before and after the filtering operation F_1. One observes that a nearly perfect MI phase with filling factor $\nu = 1$ is created in the center of the trap. Defects in this phase are due to the presence of holes and concentrate at the borders of the trap. This behavior is reminiscent of fermions, for which excitations can only be created within an energy range of order kT around the Fermi level. This numerical observation can easily be understood within our previous analysis of the initial state [Sect. 3.1.2]. Filtering removes phase II, which is due to doubly occupied sites, and leaves the fermionic phase I unaffected [Fig. 3.6a].

The fermionic picture allows us to to find a simple estimate for the amount of entropy that remains after filtering. From the density of states in band I, $g(E) = 1/\sqrt{bE}$, one immediately obtains that the number of states (lattice sites), which lie within an energy range of $2kT$ around the chemical potential μ, is given by:

$$\Delta = \frac{2}{\beta\sqrt{b\mu}}. \tag{3.17}$$

This parameter is characteristic for the tail width of the density distribution [Fig. 3.6] and will in the following be central for the analysis of our protocols. Since the final entropy must be localized at these sites we expect that $S_f \approx \Delta$. Let us now study the cooling efficiency of F_1 more rigorously. Relying again on the fermionic description this means we have to compute the entropy S

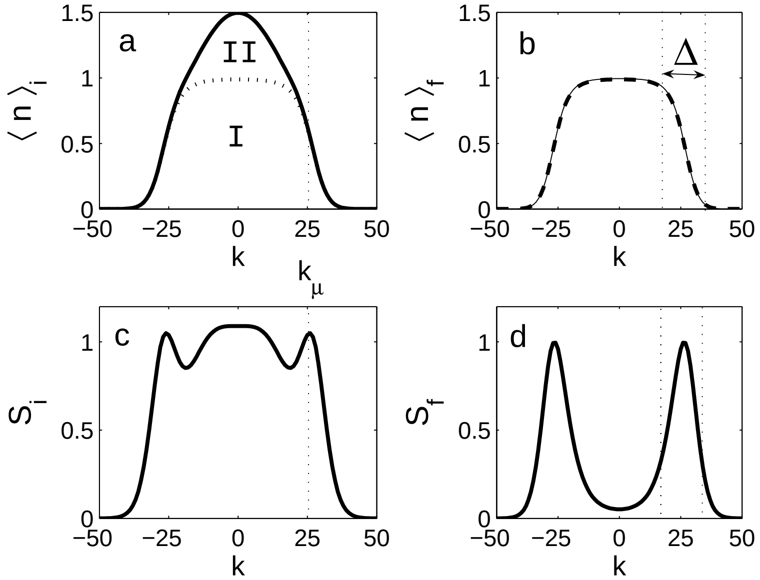

Figure 3.6: Spatial dependence of the mean occupation number $\langle n\rangle$ and entropy S before (left) and after (right) the application of the filter operation F_1. The final particle distribution can be well described by Eq. (3.8) (dashed line). Numerical parameters for initial state: $N_i = 65$, s_i=1, $U/b = 700$, $\beta U = 4.5$ and $\mu/U = 1$. Figures of merit: $s_f/s_i = 0.56$ and $N_f/N_i = 0.80$.

and the particle number N corresponding to the bands I and II [Fig. 3.3]. The entropy of a fermionic distribution of the form (3.8) is given by:

$$\begin{aligned} S_F(b,\beta,z) &= \frac{1}{\sqrt{\beta b}}\,\left[\sigma(z) + \frac{\sqrt{\pi}}{2\ln 2}(2\;\ln z\;\mathrm{Li}_{1/2}(-z)\right.\\ &- \left.\mathrm{Li}_{3/2}(-z))\right], \qquad (3.18)\end{aligned}$$

with fugacity $z = e^{\beta\mu}$ and $\mathrm{Li}_n(x)$ denoting the polylogorithm functions. The function $\sigma(z)$ is defined as the integral

$$\sigma(z) := \int_{-\infty}^{\infty} dx\;\log_2\left(1 + z\;e^{-x^2}\right). \qquad (3.19)$$

For phase I one can find a simpler expression for the entropy (3.18) by expansion around the Fermi level $k = k_\mu + dk$. Note that the range of validity, $|dk| \ll 1/\sqrt{\beta b}$, of this approximation covers all lattice sites that give a significant contribution to the total entropy. This yields the following relations for the entropy and particle number in band I:

$$S_{\mathrm{I}} \approx \sigma_{\mathrm{I}}\frac{2}{\beta\sqrt{b\mu}}, \quad N_{\mathrm{I}} \approx \overline{N}, \qquad (3.20)$$

with $\sigma_{\mathrm{I}} := \pi^2/(6\ln 2)$ and

$$\overline{N} = 2\sqrt{\frac{\mu}{b}}. \tag{3.21}$$

Here we have defined the new parameter $\overline{N}$, because it will become important in assessing the performance of the protocols presented in the remainder of this chapter. In contrast to the lower band, phase II typically does not exhibit an extended Fermi sea. Hence a Sommerfeld-type expansion around the Fermi level is not justified and one obtains only the general formulas:

$$S_{\mathrm{II}} = S_F(b, \beta, z_{\mathrm{II}}), \quad N_{\mathrm{II}} = -\sqrt{\frac{\pi}{\beta b}}\,\mathrm{Li}_{1/2}(z_{\mathrm{II}}), \tag{3.22}$$

with $z_{\mathrm{II}} = e^{\beta\mu_{\mathrm{II}}}$. In the special case $\mu = U$ one can simplify the above expressions to:

$$S_{\mathrm{II}} \approx \sigma_{\mathrm{II}}\frac{1}{\sqrt{\beta b}}, \quad N_{\mathrm{II}} \approx \eta_{\mathrm{II}}\frac{1}{\sqrt{\beta b}}, \tag{3.23}$$

with numerical coefficients $\sigma_{\mathrm{II}} \approx 2.935$ and $\eta_{\mathrm{II}} = (1-\sqrt{2})\sqrt{\pi}\zeta(1/2) \approx 1.063$.

Based on these findings we can now give a quantitative interpretation of Fig. 3.6. The initial entropy is composed of two components: $S_i = S_{\mathrm{I}} + S_{\mathrm{II}}$. Filtering removes the contribution S_{II}, which arises from the coexistence of singly and doubly occupied sites. The final entropy is thus given by $S_f = S_{\mathrm{I}}$. This residual entropy is localized around the Fermi levels $-k_\mu$ and k_μ within a region of width $\Delta = \overline{N}/(\beta\mu)$ and amounts to $S_f = \sigma_{\mathrm{I}}\,\Delta$. For the initial and final particle numbers one has the corresponding relations: $N_i = N_{\mathrm{I}} + N_{\mathrm{II}}$ and $N_f = N_{\mathrm{I}}$. Hence, the final entropy per particle can be written as:

$$s_f = \frac{S_f}{N_f} \approx \sigma_{\mathrm{I}}\frac{1}{\beta\mu}. \tag{3.24}$$

For the special choice $\mu = U$ (or equivalently $\langle n_0\rangle = 1.5$) one finds the following expressions for our figures of merit:

$$\frac{s_f}{s_i} \approx \frac{\sigma_{\mathrm{I}}}{\sqrt{\beta U}}\frac{\eta_{\mathrm{II}} + 2\sqrt{\beta U}}{\sigma_{\mathrm{II}}\sqrt{\beta U} + 2\,\sigma_{\mathrm{I}}}, \tag{3.25}$$

$$\frac{N_f}{N_i} \approx \frac{1}{1 + \frac{\eta_{\mathrm{II}}}{2\sqrt{\beta U}}}. \tag{3.26}$$

This result shows that filtering becomes more efficient with decreasing temperature, since $s_f/s_i \propto 1/\sqrt{\beta U} \to 0$ and $N_f/N_i \to 1$ for $\beta U \to \infty$.

It is important to note that the state after filtering is not an equilibrium state, because it would be energetically favorable to doubly occupy sites in the center of the trap rather than singly occupy sites in the distant border regions. However, thermal equilibrium can easily be restored by adapting the trap strength. While tunnelling is still suppressed, one has to decrease the strength of the harmonic confinement to a new value b', with $b' \leq b\, U/(2\mu)$. The system is then in the equilibrium configuration $f_k(b', \beta', \mu')$ (3.8) with rescaled parameters $T' = T\, b'/b$ and $\mu' = \mu\, b'/b \leq U/2$. This observation shows that it is misleading to infer the cooling efficiency solely from the ratio T'/T, because it depends crucially on the choice of b'.

3.2.2 Optimal initial conditions

Let us now study how the cooling efficiency of filtering depends on the initial state variables b, β and μ. Since the initial temperature is dictated by the experimental setup, we consider only the trap strength b and the chemical potential μ (which can be varied via the particle number N) as free parameters. Since our figures of merit are computed per particle we expect a weak dependence on N and therefore focus on the b dependence. This can be studied in terms of the mean central occupation number $\langle n_0 \rangle$. For instance, in the special case $\langle n_0 \rangle = 1.5$, we have obtained the analytical expression (3.25) for the ratio s_f/s_i, which exhibits a strong temperature dependence. In contrast, for $\langle n_0 \rangle = 2$ one finds that the cooling efficiency becomes independent of the temperature: $s_f/s_i \approx 1/\sqrt{3}$ for $\beta U \gg 1$. This can be understood from the presence of a $\nu = 2$ MI phase in the center of the trap, which does not contain entropy. In the opposite regime $\langle n_0 \rangle = 1$ the protocol has no cooling effect at all.

For general $\langle n_0 \rangle$, we have computed the figures of merit numerically exact [Fig. 3.7]. One observes that for initial entropies $s_i \lesssim 1$ a central filling $\langle n_0 \rangle \approx 1.5$ is always close to optimal. A special situation arises when we approach zero temperature. As shown in Fig. 3.7d, the quantity s_f/s_i changes first periodically when decreasing the trap strength b/U. In this regime an additional MI phase with $\nu = 2$ is present in the center of the trap and the splitting of the entropy between the lower and upper fermionic band is very sensitive to variations of the harmonic confinement. In particular, one can find trap strengths (e.g. $U/b \approx 2000$ in Fig. 3.7d) at which the final entropy approaches zero and only a comparatively small number of particles is lost ($N_f/N_i = 0.9$). For shallower traps the $\nu = 2$ MI phase starts to collapse. In this regime it becomes very difficult to find proper thermal states which match the initial conditions in terms of entropy and particle number. Finally, the central occupation approaches one and the cooling protocol leaves the initial state unchanged.

It is also interesting to study the efficiency of filtering when acting on the

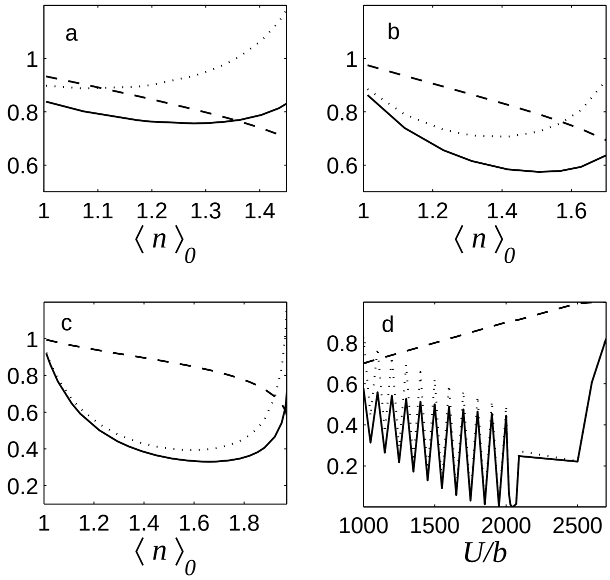

Figure 3.7: Cooling efficiency of the filtering operation F_1 for fixed initial entropy s_i and particle number N_i as a function of the harmonic trap strength. We parameterize the trap strength by either the mean central occupation number $\langle n_0 \rangle$ or the inverse trap strength U/b. We plot the figures of merit s_f/s_i (solid), N_f/N_i (dashed) and the weighted quantity $(s_f N_i)/(s_i N_f)$ (dotted). The initial parameters are $N_i = 100$ and (a) $s_i = 1.5$, (b) $s_i = 1$, (c) $s_i = 0.5$ and (d) $s_i = 0.05$.

full 3D lattice. In this case only a small subset of 1D tubes will satisfy the optimal initial conditions. Using the parameters of Sect. 3.1 ($s_i = 1$ and $N = 2\ 10^5$) we obtain that $s_f/s_i = 0.78$ and $N_f/N_i = 0.62$ for a typical trap strength $b = U/370$ as in the setup [24]. The relatively large particle loss results from the high densities in the center of the trap. This is also the main reason why the protocol performs worse compared to a 1D tube with $s_i = 1$ as shown in Fig. 3.7b.

3.2.3 Experimental realization of ultra-fast filtering

We now propose an ultra-fast, coherent implementation of filtering, which is based on optimal laser control. We restrict our discussion to the filtering operation F_1 which is the most relevant for our upcoming cooling protocols. We consider atoms in a particular internal level, $|a\rangle$, which are coupled to a second internal level, $|b\rangle$, via a Raman transition with Rabi frequency $\Omega(t)$. In contrast to the adiabatic scheme [45] we consider constant detuning, but vary $\Omega(t)$ in time. The Hamiltonian for a single lattice site reads

$$\begin{aligned}\hat{H} &= \frac{U_a}{2}\hat{n}_a(\hat{n}_a-1)+U_{ab}\hat{n}_a\hat{n}_b+\frac{U_b}{2}\hat{n}_b(\hat{n}_b-1)\\ &\quad -(\Omega(t)\hat{a}^\dagger\hat{b}+\Omega^*(t)\hat{b}^\dagger\hat{a}),\end{aligned} \tag{3.27}$$

where U_a, U_b and U_{ab} denote the on-site interaction energies, according to the different internal states. Note that $\Omega(t)$ can be complex, thus allowing for time-dependent phases. Our goal is to populate state $|a\rangle$ with exactly one particle per site which can be expressed by the unitary operation U_0 : $|N,0\rangle \rightarrow |1,N-1\rangle,\ \forall\ N\in\{1,2,\ldots,N_{max}\}$. In order to do this, we control the time-dependence of $\Omega(t)$ coherently and in an optimal way. To be more precise, we optimize a sequence of M rectangular shaped pulses of equal length:

$$\Omega(t)=\sum_{l=1}^{M}\Omega_l\times[\theta(t-t_l)-\theta(t-t_{l+1})]. \tag{3.28}$$

After time T the system has evolved according to the unitary operator $U(T)$. We want to minimize the deviation of $U(T)$ from the desired operation U_0, which we quantify by the infidelity $\epsilon(T)=\sum_{N=1}^{N_{max}}\epsilon_N$, where $\epsilon_N=1-|\langle 1,N-1|U(T)|N,0\rangle|$. Since we allow for complex Rabi frequencies, $\epsilon(T)$ is a function of $2M$ parameters $\{\Omega_l,\Omega_l^*\}$ with $l=1,\ldots,M$. For given M and time T we optimize the cost function $\epsilon(T)$ numerically using the Quasi-Newton method with a mixed quadratic and cubic line search procedure. This is repeated for different times T, while keeping the number of pulses M constant. We then increase M and repeat the whole procedure in order to check convergence of our results.

In Fig. 3.8 we plot the minimal error $\varepsilon(T)$ for different interaction strengths. Already for our simple control scheme we obtain very small errors, e.g. $\epsilon\sim 10^{-4}$ for operation time $T\approx 7/U_a$ and interaction strengths $U_{ab}=U_b=0.2U_a$. In comparison, the adiabatic scheme [45] would require $T\approx 150/U_a$ for the same set of parameters. Apart from the gain in operation speed, our method has the second advantage that it reaches high operation fidelities over a much broader range of interaction energies as compared to [45].

It is important to remark that the operation time increases with decreasing interaction anisotropy $\delta=|U_a+U_b-2U_{ab}|/U_a$. For $\delta=0$ our method fails completely. In the special case $U_a=U_b=U_{ab}$ this follows from the fact that in the Hamiltonian (3.27) the interaction part commutes with the coupling part. These problems can be solved, either by displacing the lattices that trap atoms $|a\rangle$ and $|b\rangle$ and thereby reducing the effective interaction, U_{ab}, or by performing more elaborate controls than the one from Eq. (3.28).

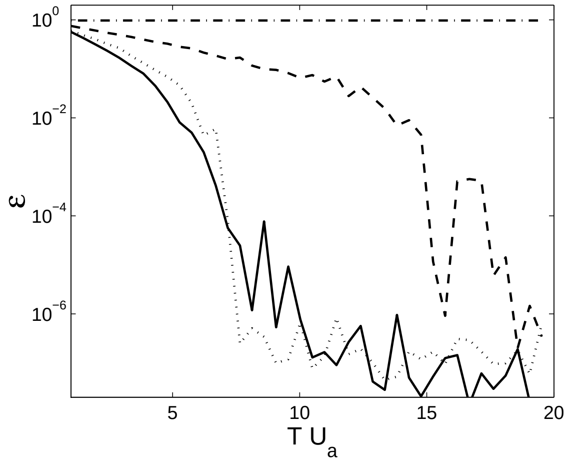

Figure 3.8: Operation error ϵ vs. operation time TU_a for different interaction energies: $U_b = 0.2U_a$, $U_{ab} = 0.2U_a$, $\delta = 0.8$ (solid); $U_b = U_a$, $U_{ab} = 0.6U_a$, $\delta = 0.8$ (dashed); $U_b = U_a$, $U_{ab} = 0.2U_a$, $\delta = 1.6$ (dotted); $U_b = U_a = U_{ab}$, $\delta = 0$ (dashed-dotted). We optimize a sequence of $M = 10$ pulses (3.28) and have chosen an occupation number cutoff $N_{max} = 4$.

3.2.4 Experimental realization of continuous filtering

So far all physical realizations of filtering rely on the *coherent* transfer of particles between two internal states followed by particle removal. We will now show that both processes can be combined into a single step. This produces an *incoherent* evolution that gives rise to the completely positive map F_1 (3.16).

The experimental procedure for achieving the map F_M is very simple. We will use two atomic states: one atomic state shall be confined by an optical lattice, deep in a MI phase, while the other one will be in a continuum of untrapped states which are free to escape the lattice. We will couple the trapped and untrapped states with two Raman lasers which have a relative detuning of the order of the interaction energy, $\delta \sim MU$ [Fig. 3.9]. As long as the coupling is active, the lasers will depopulate lattice sites which have too many atoms, $n > M$, while leaving other sites untouched [3]. If the untrapped states are such that they have few atoms and they are quickly expelled from the trap (for instance by a magnetic field gradient), these states will behave

---

[3] Additionally, particles from the tails may also be coupled to the continuum and expelled. In order to avoid that this process leads to an unwanted increase of entropy in the tails, one can lower the harmonic confinement once the MI phase has been reached.

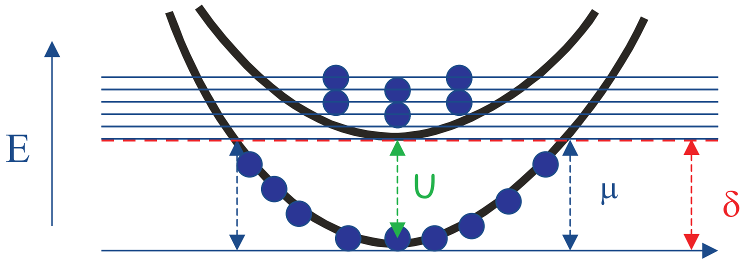

Figure 3.9: Possible physical realization of incoherent and continuous filtering F_1. The detuning of the laser frequency is chosen to be $\delta = U$. This means that atoms with energy $E \geq U$ are resonantly coupled to a continuum of untrapped states and thereby removed from the system.

for practical purposes like a thermal bath in a vacuum state. If the coherence time of this bath, physically determined by the time free atoms spend close to the trapped ones, is very short compared to the Rabi frequency Ω of the Raman transition, we will be allowed to write a master equation for the trapped atoms. The solution of this equation converges at large times to the desired filtered state, e.g. $M = 1$ for F_1.

Conceptually, this mechanism is equivalent to the frequency knife from evaporative cooling, where atoms containing too much kinetic energy are expelled from the trap in order to lower the temperature. In our case, however, it is the interaction energy we get rid off and, as a side effect, we make the filling of the lattice more uniform.

Compared to the optimal control scheme in [64], the operation of this much simpler method is not very fast. From the solution of the master equation it follows that states with occupation $n > 1$ decay after a time which is of the order of the inverse Rabi frequency, $t_1 \sim 1/(n\Omega)$. The main source of errors arises from the non-resonant coupling of the $n = 1$ state with the reservoir. The probability of a defect (empty site) will approximately be given by: $p_0 \approx \Omega^2/U^2$. Hence, for $p_0 = 10^{-4}$ we get an operation time $t_1 \sim 100/U$ which is comparable to the time scale of the adiabatic scheme [45]. However, our incoherent scheme has two big advantages. First, it can be applied continuously. Second, it does not put any constraints on the interaction energies of the two species. This holds under the assumption that untrapped atoms are expelled so quickly from the trap, that they do not interact significantly with the trapped atoms.

3.3 Ground state cooling protocols

We have seen that the residual entropy after filtering is concentrated at the borders of the atomic cloud. Particles located at these sites are also the only source of energy excitations because all doubly occupied sites have been removed. In the following we will propose several protocols which selectively remove particles at the borders, thereby bringing the system closer to its ground state.

3.3.1 Sequential filtering

Filtering is limited by the fact that it cannot correct defects that arise from holes in a perfect MI phase. In order to overcome this problem, we will now propose two protocols, which rely on the repeated application of filtering. The central idea is to transfer "hot" particles from the borders to the center of the trap, where they can be removed by subsequent filtering.

Discrete Protocol

The main feature of this protocol is that filtering is always performed in the no–tunnelling regime. Reformation of doubly occupied sites is achieved by adiabatically varying the lattice and trapping potential. To be more specific, one has to iterate the following sequence of operations: (i) we allow for some tunnelling while the trap is adjusted adiabatically in order to reach a central occupation of $\langle n_0 \rangle \approx 1.5$; (ii) we suppress tunnelling and perform the filtering operation F_1; (iii) the trap is slightly opened so that the final distribution resembles a thermal distribution of hard-core bosons.

We are interested in the convergence of the entropy and temperature as a function of the number of iterations. However, the adiabatic process is very difficult to treat both analytically and numerically. Therefore we distinguish in the following between three different scenarios that are based on specific assumptions.

(i) Thermal equilibrium: We assume that the entropy is conserved and that the system stays in thermal equilibrium throughout the adiabatic process. Since this condition will in general not be fulfilled for closed, isolated quantum systems, the following analysis can only provide a rather rough description of the real situation. To be more precise, we start from a thermal state with initial parameters β, b and μ. After filtering and adiabatic evolution one has a thermal state in the no-tunnelling regime with new parameters β', b' and μ'. As we have shown in the previous sections, thermal states in the no-tunnelling regime can effectively be described in terms of two fermionic components. This allows us to determine the new parameters β' and b' by identifying: $S_{\mathrm{I}}(\beta, b) = S_{\mathrm{I}}(\beta', b') + S_{\mathrm{II}}(\beta', b')$ and $N_{\mathrm{I}}(\beta, b) = N_{\mathrm{I}}(\beta', b') + N_{\mathrm{II}}(\beta', b')$. The desired central filling $\langle n_0 \rangle = 1.5$ fixes the chemical potentials to be $\mu = \mu' = U$. Using expressions (3.20) and (3.23) one finds:

$$\begin{aligned} \beta' U &= \left(A + \sqrt{A^2 + 4\beta U}\right)^2 /4, && (3.29) \\ \frac{b'}{U} &= \frac{b}{U}\left(1 + \frac{\eta_{\mathrm{II}}}{2\sqrt{\beta' U}}\right), && (3.30) \end{aligned}$$

with $A = (\sigma_{\mathrm{II}} \beta U / \sigma_{\mathrm{I}} - \eta_{\mathrm{II}})/2$. After a second filtering operation the entropy per particle is thus given by:

$$s_2 = \sigma_{\mathrm{I}} \, \frac{1}{\beta' U}. \tag{3.31}$$

Since our analysis only holds in the limit $\beta U \gg 1$, one can simplify the above expressions to: $\beta' U \approx (\sigma_{\mathrm{II}} \beta U / (2\sigma_{\mathrm{I}}))^2$ and $b' \approx b$. This allows us to establish a simple recursion relation for the entropy per particle s_n after the n-th filter operation:

$$s_n \approx \frac{4\sigma_{\mathrm{I}}}{\sigma_{\mathrm{II}}^2} \, s_{n-1}^2. \tag{3.32}$$

Since the limit $\beta U \gg 1$ implies $s < 1$, one finds that the entropy per particle converges extremely fast to zero.

(ii) Quantum evolution: Let us now study a more realistic situation. To this end we resort to the effective description in terms of independent fermions [Sect. 3.1.2 and Appendix C]. Since the effective Hamiltonian $\tilde{H}$ (3.13) is quadratic, we can study the complete protocol on a single-particle basis. We further assume that the single-particle energy spectrum does not exhibit level crossings in the course of the adiabatic evolution. Then, the state at any time t can be computed by populating the single-particle energies of the effective Hamiltonian $\tilde{H}(t)$ (3.13) according to the initial probabilities (after filtering) in energetically increasing order. This method is illustrated in more detail in Fig. 3.3. After the initial filtering step only states in the lowest energy band are occupied and the occupation probability is given by the fermionic distribution $f_k(b, \beta, \mu)$ (3.8). Increasing the trap strength to an appropriate value $b' > b$ in the course of the adiabatic process makes it energetically favorable to occupy also the second band. We find the state after returning to the no-tunnelling regime, ρ', by populating the energy levels, corresponding to the new trap strength b', in energetically increasing order according to the initial probabilities $f_k(b, \beta, \mu)$. At this point we distinguish between two further scenarios: **(ii.a)** The state ρ' is mapped to a thermal state in the usual way by accounting for energy and particle number conservation. This way we can quantify the amount of "heating" resulting from the fact that the system is not in thermal equilibrium at the end of the adiabatic process due to the different structure of the energy spectrum. **(ii.b)** We continue the protocol directly with the time evolved state ρ'.

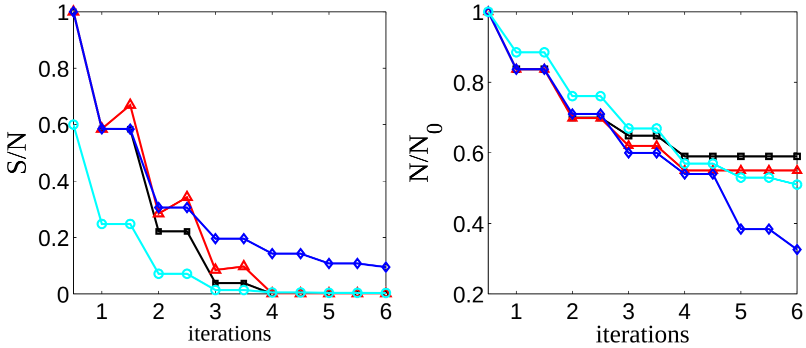

Figure 3.10: Entropy per particle S/N (left) and normalized number of particles N/N_0 (right) as a function of the number of filtering iterations for initially $N_0 = 100$ particles. As discussed in the text, we distinguish between the scenarios (i) (black line), (ii.a) (red line) and (ii.b) (blue and cyan).

Our results for all three cases are summarized in Fig. 3.10. We have computed numerically exact the entropy per particle as a function of the number of filtering cycles. Starting with an initial entropy $s_0 = 1$, scenarios (i) and (ii.a) predict that an entropy value close to zero can be obtained after only four iterations of the protocol [4]. According to our underlying assumptions the system is in thermal equilibrium after each iteration of the protocol. In scenario (ii.b) the final entropy saturates at a finite value and the system is not in perfect thermal equilibrium. However, the final state still resembles a thermal state of hard-core bosons in a harmonic trap.

These results imply that sequential filtering can clearly profit from equilibration. The reason is that equilibration reduces the defect probability in the center of the lower band and transfers entropy to the upper band, where it can be removed subsequently. This process in combination with the increasingly high cooling efficiency of filtering at low temperatures can easily compensate the heating induced by the adiabatic quantum evolution. From

---

[4] Remember that for thermal states at very low temperatures the entropy is concentrated in only a few particles. Hence, finite size effects become important and the minimal attainable entropy per particle depends very sensitively on the strength of the harmonic confinement.

our data we can deduce that this heating corresponds to an entropy increase of around 20 % [5]. Without equilibration sequential filtering becomes very inefficient after the fourth iteration, which is also reflected in the excessive particle loss [Fig. 3.10]. The minimal attainable entropy is determined by the initial defect (hole) probability in the center of the trap. Starting from a much colder state, which exhibits almost unit filling in the center of the lower band, therefore yields a final state very close to the ground state [Fig. 3.10].

Remember that scenario (ii.b) is based on the assumption that no level crossings occur during the evolution. From our numerical analysis of the energy spectrum of (3.13) we know, however, that level crossings can indeed appear (see also [127, 132]). The reason is the vanishing small spatial overlap between single particle states at the border of the lower band and the center of the upper band. This has the following consequences for our previous analysis: For rather small particle numbers ($N \lesssim 15$) level crossings are rare and inter-band coupling occurs already for hopping rates, which are well within the range of validity of our single-particle description. We therefore expect that our predictions, as depicted in Fig. 3.10, are reasonable. For larger systems one has to tune the tunnelling rate deep into the superfluid regime $J \gtrsim 0.5$ in order to couple the two bands and to form doubly occupied sites. However, this regime is no longer accessible within our fermionic model (3.13). It remains to be investigated to what extent this will alter our predictions for the cooling efficiency of sequential filtering.

Continuous protocol

As an alternative to the previous scheme, one can devise a continuous variant, which operates at a fixed but non-zero hopping rate. Such a protocol would clearly profit from the fact that adiabatic changes of the lattice potential, which might lead to additional heating, are not required.

Let us first study how the cooling efficiency of filtering changes as a function of the hopping rate J. The results are shown in Fig. 3.11. For high temperatures the ratio s_f/s_i is rather independent of J and we achieve some cooling. For very small temperatures, $kT \lesssim 0.01U$, it changes dramatically with J. This is a clear signature of the quantum phase transition, which is expected to occur at $J_c \approx 0.085U$ in the thermodynamic limit. While for $J < J_c$ the state is well described in terms of independent wells and filtering works very efficiently, for $J > J_c$ particles are delocalized over the lattice, and filtering causes heating rather than cooling.

---

[5] We have also performed multi-particle calculations in the canonical ensemble, which predict an even lower value of about 5%.

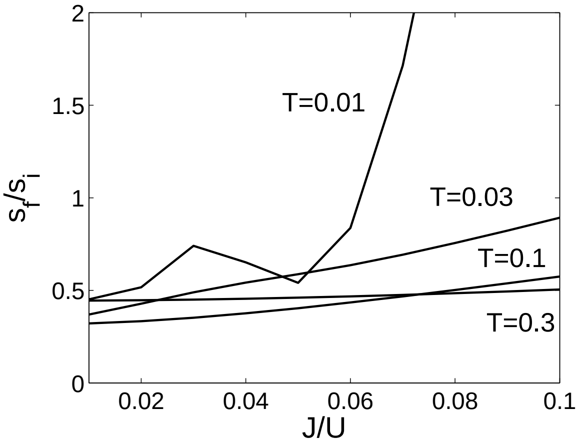

Figure 3.11: Cooling efficiency $s_{2,f}/s_{2,i}$, in terms of the Rényi entropy, of filtering F_1 as a function of the hopping rate J/U. For the numerical computation in terms of MPS we use a lattice of length $L = 27$, which typically contains $N \approx 20$ particles. The trap strength is chosen to be $b/U = 1/65$ and $\mu = U$, yielding $\langle n \rangle_0 \approx 1.5$.

A second important ingredient of sequential filtering is the generation of doubly occupied sites. In order to accomplish this in a continuous way one has to fix the hopping rate at a value, at which there exists a coupling between doubly occupied sites at the center and singly occupied sites at the borders. Our analysis of the effective Hamiltonian (3.13) shows, however, that this occurs typically only deep in the SF regime for $J/U \gtrsim 0.5$.

Together with the findings in Fig. 3.11 one has to conclude that this continuous variant of sequential filtering can only be used as an initial step, when temperatures are still comparatively high.

3.3.2 Algorithmic Cooling

We now propose a second cooling scheme, which we call *algorithmic cooling*, because it is inspired by quantum computation. As before the goal is to remove high energy excitations at the borders of the atomic cloud, which have been left after filtering. In contrast to sequential filtering we now restrict ourselves to a sequence of quantum operations that operate solely in the no-tunnelling regime.

The protocol

The central idea is to make use of spin-dependent lattices. A part of the atomic cloud can then act as a "pointer" in order to address lattice sites which contain "hot" particles. In this sense the scheme is similar to evaporative cooling, with the difference that an atomic cloud takes the role of the rf-knife. Another remarkable feature of the protocol is that the pointer is very inaccurate in the beginning (due to some inherent translational uncertainty in the system), but becomes sharper and sharper in the course of the protocol.

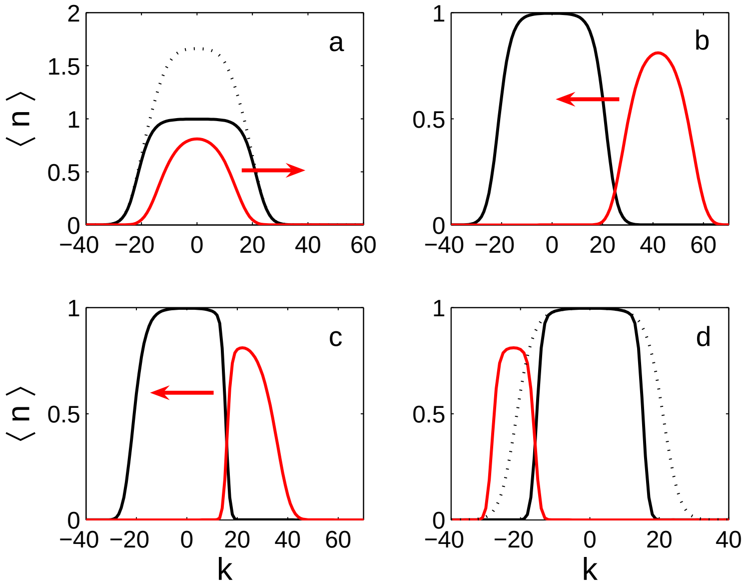

Figure 3.12: Illustration of the algorithmic cooling protocol. The state is initialized with the filter operation F_2. (a) Particles from doubly occupied sites are transferred to state $|b\rangle$ (red) using operation $U^{1,1}_{2,0}$. (b) The lattice $|b\rangle$ has been shifted $2k_\varepsilon$ sites to the right, so that the two distributions barely overlap. (c) Density distribution after k_s lattice shifts. After each shift doubly occupied sites have been emptied. Afterwards lattice $|b\rangle$ is shifted $4k_\varepsilon - k_s$ sites to the left and an analogous filter sequence is applied. (d) The final distribution of atoms in state $|a\rangle$ is sharper compared to the initial distribution (dotted). Numerical parameters: $N_i = 65$, $s_i = 1$, $U/b = 300$, k_ε=21, $k_s = 20$, $N_f = 30.2$, $s_f = 0.31$ (after equilibration).

The individual steps are the following: (i) We begin with a cloud in thermal equilibrium in the no-tunnelling regime, having two or less atoms per site, all in internal state $|a\rangle$. This can be ensured with a filtering operation

F_2. (ii) We next split the particle distribution into two, with an operation $U_{2,0}^{1,1}$ [Fig. 3.12a]. (iii) The $|a\rangle$ and $|b\rangle$ atoms are shifted away from each other until both ensembles barely overlap [Fig. 3.12b]. We then empty all doubly occupied sites and shift the clouds one lattice site towards each other. This sequence is iterated for a small number of steps of order Δ (3.17), thereby sharpening the density profiles of both clouds [Fig. 3.12c]. (iv) The atoms of type $|b\rangle$ are moved again to the other side of the lattice and a process similar to (iii) is repeated [Fig. 3.12d]. (v) Remaining atoms in state $|b\rangle$ can now be removed.

Experimentally, doubly occupied sites can be emptied by introducing a third internal level $|c\rangle$ and applying the unitary operation $U_{1,1,0}^{0,0,2}$ in generalization of (3.15). Afterwards all atoms in $|c\rangle$ are removed.

Scaling behavior and numerical results

The density distribution after the protocol will never be perfectly sharp [Fig. 3.12d] because this protocol is intrinsically limited by thermal and quantum fluctuations in the initial state. Qualitatively, in order to remove a particle of type $|a\rangle$ from the tail, one has to put a particle of type $|b\rangle$ from the other cloud on the same lattice site. Errors arise when a particle of type $|a\rangle$ hits a hole instead of a particle of type $|b\rangle$. The error probability is thus proportional to the fluctuations of the density on each lattice site. If we want to clean about Δ sites or remove Δ particles, the errors will be $\mathcal{O}(\sqrt{\Delta})$. In the limit $\beta U \gg 1$, we obtain the following scaling behavior for the final entropy per particle:

$$s_f \propto \frac{\sqrt{\Delta}}{\overline{N}} = \frac{1}{\sqrt{\overline{N}}\,\sqrt{\beta\mu}} \propto \frac{1}{\sqrt{N_i}}, \tag{3.33}$$

where $\overline{N}$ (3.21) is the number of particles in $|a\rangle$ after step (ii) and N_i is the initial particle number. This simple estimate shows that the algorithmic protocol becomes more efficient with increasing initial particle number. This is in contrast to filtering, for which s_f is independent of N_i.

We have verified numerically the scaling (3.33) [Fig. 3.13b]. The numerical simulation is by no means trivial because the protocol establishes classical correlations both among lattice sites and also among internal states. To reproduce these correlations we have resorted to a representation of classical density matrices in terms of MPS [Appendix D]. These numerical simulations also show that the final density distribution is very close to a thermal distribution [Fig. 3.13a]. This does not necessarily mean that the underlying state is close to an equilibrium state. If one applies one or few iterations of

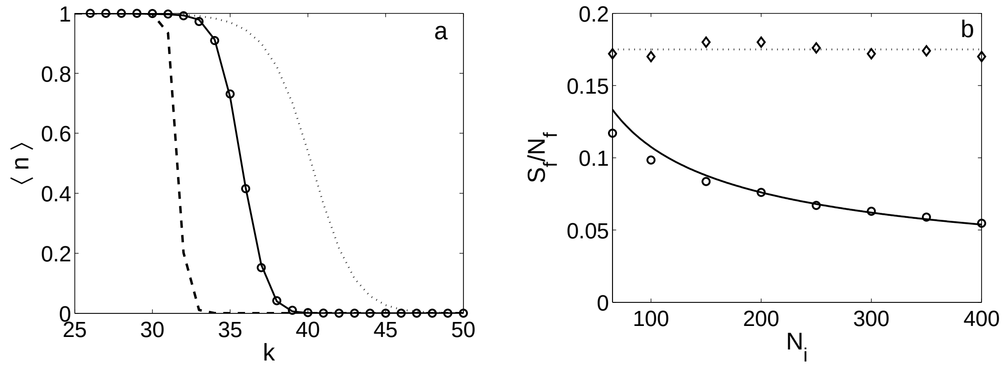

Figure 3.13: (a) Density distribution after filtering (dotted) and after algorithmic cooling (solid) which can be well approximated by a thermal distribution (circles). For comparison we consider a variant of the algorithmic protocol, which exhibits no classical correlations at all times (dashed). Parameters for the initial state: $N_i = 100$, $s_{2,i} = 0.42$ ($s_i = 0.50$), $U/b = 1500$; Parameters for the algorithmic protocol: $k_0 = 62$, $k_s = 18$, $N_f = 71.4$, $s_{2,f} = 0.0659$; Final entropy after equilibration: $s_{2,f} = 0.0740$ ($s_f = 0.0988$); Parameters for alternative protocol (dashed line): $k_s = 28$, $N_f = 63.3$, $s_f = 0.0389$. (b) Final entropy per particle s_f as a function of the initial particle number N_i for fixed $s_i = 0.5$ (circles). For large N_i one obtains a $1/\sqrt{N_i}$ dependence (solid). For comparison we plot s_f after filtering (diamonds) which is expected to be independent of N_i (dotted). Small variations in s_f can be attributed to the specific choice of the harmonic confinement.

the protocol, the final state will still contain some holes at the borders and be close to thermal equilibrium, as the computation of the Rényi entropy entropy $s_{2,f}$ (3.14) before and after equilibration shows [Fig. 3.13a]. For a large number of iterations, however, the final state will be far from thermal equilibrium. As will be discussed later in more detail, the density matrix is then given by an incoherent superposition of perfect uniform MI states which differ in their length and position [see Fig. 3.17]. Hence, this protocol can also be used to generate an ensemble of quantum registers, similar to the ones produced by the protocols in Sect. 3.4. These registers form the basis for quantum computation with atoms in optical lattices.

3.3.3 Theoretical description

For the sake of simplicity we consider a slightly modified version of the protocol. The particle distributions $|a\rangle$ and $|b\rangle$ are now two identical but independent distributions of hard-core bosons of the form (3.8) [6]. The lattice $|b\rangle$ is shifted $2k_\varepsilon$ sites to the right. For given ε the value $k_\varepsilon = \sqrt{\mu/b}\sqrt{1-\ln\varepsilon/\beta\mu}$ is chosen such that for atoms $|a\rangle$ it holds $\langle n^a_{k_\varepsilon}\rangle = \varepsilon$. This initial situation is depicted schematically in Fig. 3.14.

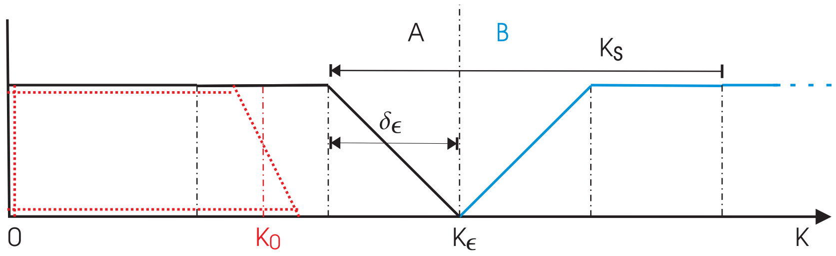

Figure 3.14: Schematic description of the initial state for lattice sites $k \geq 0$: Two identical density distributions for hard-core bosons, belonging to different species A (black) and B (blue), are shifted $2k_\varepsilon$ lattice sites apart. The region of non-integer filling has width δ_ε. In the course of the protocol the lattice of species B is shifted $k_s = 3\delta_\varepsilon$ sites to the left.

The cutoff ε defines also the width of the region with non-integer filling:

$$\delta_\varepsilon = \sqrt{\mu/b}\left(\sqrt{1-\ln\varepsilon/\beta\mu} - \sqrt{1+\ln\varepsilon/\beta\mu}\right). \tag{3.34}$$

We analyze first a protocol that involves $k_s = 3\delta_\varepsilon$ lattice shifts and after each shift doubly occupied sites are emptied. Our goal is to compute the final shape of the density profile of atoms in state $|a\rangle$ (red line in Fig. 3.14). It is sufficient to consider only the reduced density matrices $\hat\rho_a$ and $\hat\rho_b$, which cover the range $k \in [k_\varepsilon - 2\delta_\varepsilon; k_\varepsilon]$ and $k \in [k_\varepsilon; k_\varepsilon + 2\delta_\varepsilon]$, respectively. These density matrices can be written in terms of convex sums over particle number subspaces:

$$\hat\rho_a = \sum_{N_a=0}^{2\delta_\varepsilon} p_a(N_a)\hat\rho_a(N_a), \tag{3.35}$$

$$\hat\rho_b = \sum_{N_b=0}^{2\delta_\varepsilon} p_b(N_b)\hat\rho_b(N_b). \tag{3.36}$$

The further discussion is based on the following central observation. If a state $\hat\rho_a(N_a)$ interacts with a state $\hat\rho_a(N_b)$ then our protocol produces a

---

[6] In practice, this can be achieved by applying F_1 to two non-interacting bosonic clouds in different internal states.

perfect MI state $\hat{\rho}'_a(N'_a)$ (as in Eq. 3.5) composed of $N'_a = (N_a - N_b)/2$ particles. The factor 1/2 arises from the fact that k_s lattice shifts remove at most $k_s/2$ particles from distribution $|a\rangle$. Note that this relation also allows for negative particle numbers, because N'_a merely counts the number of particles on the right hand side of the reference point $k_0 = k_\varepsilon - 3/2\delta_\varepsilon$. The final density matrix after tracing out particles in $|b\rangle$ can then be written as a convex sum over nearly perfect (up to the cutoff error ε) MI states

$$\hat{\rho}'_a = \sum_{N'_a=-\delta_\varepsilon/2}^{\delta_\varepsilon/2} p'_a(N'_a)\hat{\rho}'_a(N'_a), \tag{3.37}$$

with probabilities

$$p'_a(N'_a) \simeq 2 \sum_{N_b=\delta_\varepsilon}^{2\delta_\varepsilon} p_a(2N'_a + N_b)p_b(N_b). \tag{3.38}$$

The factor two is due to the fact that states with $N_a - N_b = 2M$ and $N_a - N_b = 2M + 1$ are collapsed on the same MI state with $N'_a = M$. Since Lyapounov's condition [133] holds in our system, we can make use of the generalized central limit theorem and approximate $p_a(N) = p_b(N)$ by a Gaussian distribution with variance $\sigma^2 = \delta N^2 = \Delta/4 = 1/(2\beta\sqrt{b\mu})$. Evaluation of Eq. (3.38) then yields a Gaussian distribution with variance $\sigma'^2 = \sigma^2/2$. Since MI states do not contain holes, one can infer the final density distribution $\langle n^a_k\rangle'$ directly from $p'_a(N)$ by simple integration. This distribution can then be approximated by the (linearized) thermal distribution:

$$\langle n_k\rangle' \simeq \frac{1}{1 + e^{4(k-k_0)/\Delta'}}. \tag{3.39}$$

The new effective tail width $\Delta' = \sqrt{\Delta\pi}/2$ of the distribution is roughly the square root of the original width Δ (3.17). This effect leads to cooling, which we will now quantify in terms of the entropy.

When applying similar reasoning also to the left side of distribution $|a\rangle$ one ends up with a mixture of MI states, which differ by their length and lateral position. This results in an extremely small entropy of the order $S_{\mathrm{MI}} \sim \log_2 \Delta$. However, this final state is typically far from thermal equilibrium. In order to account for a possible increase of entropy by equilibration, we have to compute the entropy of a thermal state, which has the same energy and particle number expectation values as the final state. In our case this is equivalent to computing the entropy directly from the density distribution (3.39):

$$S' \approx \sigma_{\mathrm{I}}\,\Delta' = \frac{\sigma_{\mathrm{I}}\sqrt{\pi}}{\sqrt{2}}\frac{1}{(\beta^2 b\mu)^{1/4}} = \frac{\sqrt{\pi}}{2}\frac{\sqrt{\beta\mu}}{\sqrt{N}}\,S, \tag{3.40}$$

where $N = N_{\mathrm{I}}$ and $S = S_{\mathrm{I}}$ (3.20) correspond to the expectation values for the initial state of atoms $|a\rangle$ (3.35). The final particle number is given by: $N' \simeq 2k_0 \approx N(1 + \ln\varepsilon/\beta\mu)$.

A significant improvement can be made by shifting the clouds only $k_s = 2\delta_\varepsilon$ sites. This prevents inefficient particle loss, which has been included in our previous analysis in order make the treatment exact. With this variant the final particle number increases to $N'' = 2\ (k_\varepsilon - \delta_\varepsilon)$, while in good approximation the final entropy is still given by S'. Hence, the final entropy per particle can be lowered to:

$$s' = \frac{S'}{N''} \approx \frac{\sqrt{\pi}}{2}\,\frac{\sqrt{\beta\mu}}{1 + \frac{\ln\varepsilon}{2\beta\mu}}\,\frac{1}{\sqrt{N}}\ s. \tag{3.41}$$

Since s corresponds to the entropy after a possible filtering operation F_1, we can directly deduce to what extent algorithmic cooling outperforms filtering. For fixed N the ratio s'/s becomes smaller at higher temperatures. Even more important, for fixed βU, the entropy per particle s' decreases with $1/\sqrt{N}$ as the initial number of particles in the system increases. Here we recover the same scaling behavior as in our simple estimate (3.33).

Variants and extensions of the protocol

It is clear that we could cool the atoms to the ground state with 100% efficiency if the density distributions of $|a\rangle$ and $|b\rangle$ atoms were perfectly correlated. It seems also that we can improve the performance in realistic situations by removing the classical correlations which are established in the course of the protocol. To be more precise, we consider the following variant of the protocol. After each filtering operation we first break the correlations between the two atomic species (i.e. we consider only the reduced density operators) and then perform the next lattice shift. This way we ensure that no classical correlations can build up. The resulting density profile is much sharper than for the original protocol [Fig. 3.13a]. Numerically we find that the tail width of the distribution can be reduced to approximately two lattice sites independent of the original size of the cloud. From a practical point of view this protocol is, however, very demanding. The minimal number of independent copies of the system required in an actual experiment would be given by the number of filtering operations. A more realistic variant would be to break the correlations only between the atomic species at the end of the original protocol while leaving the inter–site correlations untouched. According to our theoretical analysis (Eq. (3.38)) each iteration of the complete protocol would reduce the total entropy by a factor of $\sqrt{2}$ [64]. This way one would require only a rather small number of independent copies to get closer to the ground state.

To sum up, algorithmic cooling can be improved considerably by using multiple independent clouds to clean each other. Experimentally, these clouds may come from loading the lattice with atoms in different internal states, from splitting the cloud into multiple condensates, or simply by using the clouds from different 1D tubes to clean each other... Many other possibilities can be conceived. Alternatively, the performance can be enhanced by extracting specific particle number subspaces from the final density matrix at the end of the protocol (see Sect. 3.4 for details).

Moreover, we have devised variations of the original protocol, which might be better applicable to experimental setups. Firstly, there is no need to discard the remaining atomic cloud in state $|b\rangle$. For appropriate initial trap parameters, it is preferably to move this cloud back to the center and to pump all atoms back into internal state $|a\rangle$. The resulting state will exhibit a MI shell structure with two plateaus at densities $n = 1$ and $n = 2$. This is a simple way to engineer ground states of tighter traps. Secondly, it is in principle possible to sharpen the two tails of the central cloud simultaneously. To this end we initially apply the filtering operation F_3 instead of F_2. One atom from all triply occupied sites is stored in an additional internal level. This cloud can then be used to clean one side of the distribution, while atoms in state $|b\rangle$ (which stem from doubly occupied sites) clean the other side.

Finally, let us remark that the algorithmic cooling scheme has been designed for 1D systems. In order to adapt it to 3D setups with spherical symmetry, we propose to apply the protocol at least along three orthogonal directions.

3.3.4 Discussion of results

Let us now discuss and compare the cooling performance of the protocols proposed so far. To this end we provide exact numerical results and compare them with our analytical findings. For the calculations we fix two parameters, b/U and μ/U, and determine the entropy per particle as a function of the inverse temperature βU.

Our results are shown in Fig. 3.15 and can be summarized as follows. Firstly, we find that our theoretical predictions for all three protocols – filtering, sequential filtering and algorithmic cooling – are very accurate in the low temperature limit $\beta U \gg 1$, and even hold in good approximation for the (relatively) high temperature regime $\beta U \gtrsim 1$. Secondly, our algorithmic protocol outperforms filtering considerably, especially in the high temperature range. Finally, based on the assumptions that underlie our calculations,

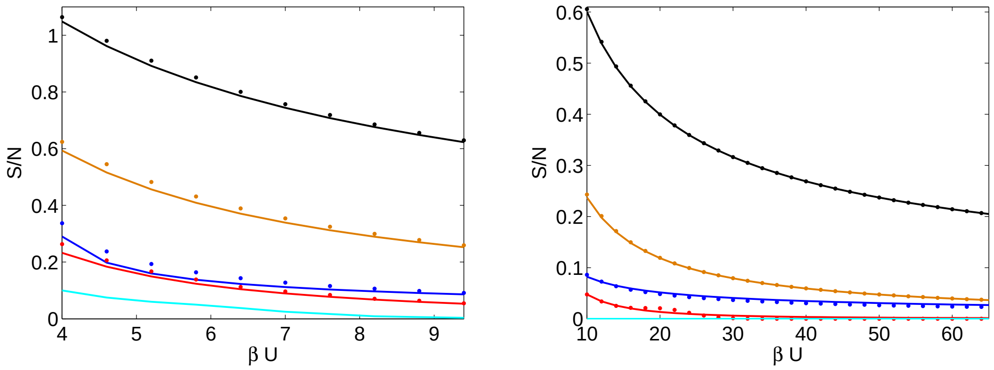

Figure 3.15: Analytical (solid) and numerical (dots) results for the entropy per particle $s = S/N$ versus the inverse temperature βU for fixed trap strength $b/U = 1/2500$ and fixed $\mu = U$. We plot the initial value (black line) and the values after filtering with F_1 (Eq. (3.24), brown line). This is compared to more elaborate cooling protocols: entropy after two iterations of sequential filtering including equilibration (Eq. (3.31), red line), minimal entropy after sequential filtering without equilibration (cyan), and entropy after algorithmic cooling (Eq. (3.41), blue line). For the algorithmic protocol we have chosen $\varepsilon = 0.03$ and $k_s = 2\ \delta_\varepsilon$. Note that this protocol creates classically correlated states. The numerics are therefore based on a representation of classical density matrices in terms of matrix-product states [Appendix C].

subsequent filtering is typically superior to algorithmic cooling with respect to the minimal achievable entropy.

We now discuss advantages, experimental requirements and time scales of our cooling protocols.

Sequential filtering

(i) *Advantages*: If one combines filtering with equilibration then the entropy per particle converges very fast to zero with the number of filter steps. The minimal value is only limited by finite size effects. Without equilibration, the minimal entropy is limited by the finite probability of finding a hole in the central MI phase of the initial distribution. Furthermore, sequential filtering naturally allows for cooling in a 3D setup, because it preserves the spherical symmetry. Note that filtering, and hence sequential filtering, can also be applied to fermionic atoms in an optical lattice [45].
(ii) *Requirements and limitations*: The repeated creation of doubly occupied sites in the center of the trap requires precise control of the harmonic con-

finement over a wide range of values. In addition, non-adiabatic changes of lattice and external potentials might induce heating, which could reduce the cooling efficiency considerably.
(iii) *Time scales*: The limiting factor here is not filtering but the adiabaticity criterion for changes of the hopping rate and the harmonic confinement. We have shown that after filtering the density distribution can be identified with a thermal distribution of hard-core bosons. Hence it is possible to find estimates for adiabatic evolution times based on fermionic single-particle states, as calculated in [127]. In the MI regime particle transfer from the borders to the center of the trap is very unlikely, because the eigenfunctions of the upper and lower Fermi band do not overlap. Therefore, we propose as a first step to decrease the lattice potential at fixed harmonic confinement until eigenfunctions start overlapping. This process can be treated very well with our fermionic model (3.13), because only the lower band is populated [Fig. 3.3]. The average energy spacing around the Fermi level is $\overline{\delta E} = bN \approx 2\ U/N$ in the no-tunnelling regime, and stays roughly constant when passing over to the tunnelling regime [127]. As a consequence, the lattice potential should be varied on a time scale $T \gg h/\overline{\delta E} \approx 10$ ms for $N = 50$ and $h/U = 396\ \mu$s [129]. For the second process, which involves the change of the harmonic potential at fixed hopping rate, it is more difficult to make analytic predictions for adiabatic time scales, since our single-particle description (3.13) is no longer justified in general. One can, however, obtain a lower bound by considering the energy spectrum after returning to the no-tunnelling regime [Fig. 3.3]. The average energy spacing around the Fermi level is now dominated by the energy spacing at the bottom of the upper band: $\overline{\delta E'} = \sqrt{b'/\beta}/2 \approx U/(N\sqrt{\beta U})$. This implies adiabatic evolution times which are a factor $\sqrt{\beta U}/2$ larger than for the first process. We have also verified the whole process numerically, using the matrix-product state representation of mixed states [102]. For initially $N = 11$ particles we find adiabatic evolution times of the order $T \sim 30\ \hbar/U$ for the first process, which is consistent with our analytical estimate. The second process is more time consuming with $T \gtrsim 120\ \hbar/U$.

Algorithmic cooling

(i) *Advantages*: The algorithmic protocol operates solely in the no-tunnelling regime. Adiabatic changes of the lattice and/or the harmonic potential, which are time consuming and might induce heating, are therefore not required. Moreover it does not demand arbitrary control over the harmonic confinement. The correct initial conditions can always be generated by the filter operation F_1. The protocol is more efficient in the high temperature

range and for large particle numbers. Additionally to ground state cooling, the algorithm can be used to generate an ensemble of nearly perfect quantum registers for quantum computation. This state, which can also be considered as an ensemble of possible ground states in the uniform system, might already be sufficient for quantum simulation of certain spin Hamiltonians. Finally, note that this protocol can naturally be applied also to fermionic systems.
(ii) *Requirements and limitations*: The heart of the protocol is the existence and control of spin-dependent lattices. Moreover, the algorithm is explicitly designed for cooling in one spatial dimension. Generalizations to higher dimensions are possible, but will typically not preserve the spherical symmetry of the initial density distribution. Moreover, one should keep in mind that the final states are typically far from thermal equilibrium.
(iii) *Time scales*: Adiabatic lattice shifts can be performed very fast on a time scale determined by the on-site trapping frequency $\nu \simeq 30$ kHz. The limiting factor is the number of filter operations, which is of the order δ_ε (3.34). Under realistic conditions this can amount to 50 operations. Filter operation times based on the adiabatic scheme [45] are of the order $T_F \sim 200\ \hbar/U$. With $h/U = 396\ \mu$s [129] one finds a total operation time $T \sim 630$ ms, which is comparable with the typical particle life time in present setups using spin-dependent lattices [47]. We have studied this problem with an alternative implementation of filtering [Sect. 3.2.3], which allows one to reduce the operation time by a factor of ~ 15, and hence makes algorithmic cooling feasible in current experimental setups.

3.3.5 Alternative cooling scheme: Filtering combined with frequency knife

We again start with the filtering operation F_1. The remaining "hot" particles located at the borders of the trap can also be removed with a method similar to evaporative cooling or a frequency knife. The idea is to make use of inhomogeneous on-site energies and to choose the detuning δ of a radiation field in such a way that only atoms located at specific lattice sites are resonantly coupled to another internal state. Using a magnetic field gradient it has been demonstrated that individual lattice sites can be resolved within an uncertainty of about five sites [134]. In our case the spatial dependence of the on-site energies is naturally provided by the harmonic trapping potential. However, in order to make use of this inhomogeneity one has to ensure that the atoms are coupled to an internal state which responds differently to the ac-Stark shift induced by the lattice laser beams. Experimentally, this can, for instance, be achieved with a setup similar to the one for the creation of spin-dependent lattices [46, 47, 130]. There, one atomic species is trapped exclusively by σ^- polarized laser light, whereas the other species is trapped predominantly by σ^+ polarized light. Hence, an optically untrapped internal state can simply be realized by using only σ^+ polarized laser light for creating the optical lattice.

Let us now estimate the requirements on the the Rabi frequency Ω of the transition depending on the trap strength b. For simplicity, we consider two internal states, and a configuration for which the excited state exhibits zero on-site energy at each lattice site. We are interested in removing particles which are typically located at a distance k_μ from the center of the trap. Hence, for resonant coupling of these atoms we must choose the detuning to be $|\delta| = bk_\mu^2 = \mu$. Particles at sites $k_\mu + \Delta k$ feel an effective detuning $\delta_{eff}(\Delta k) \approx b\overline{N}\Delta k$, where $\overline{N} = 2k_\mu$ denotes the particle number (3.21). The probability that a particle at site $k_\mu + \Delta k$ is transferred to the excited state is then given by:

$$P_e(\Delta k) = \frac{\Omega^2}{\Omega^2 + \delta_{eff}(\Delta k)^2}. \tag{3.42}$$

In order to locally address the site k_μ reasonably well one has to demand: $\Omega \lesssim b\overline{N}$. For typical harmonic trapping frequencies in the MI regime, $\omega_{ho} = \sqrt{8b/(\hbar m\lambda^2)} \gtrsim 2\pi \times 65$ Hz [24], and $\overline{N} = 50$ this translates into $\Omega \lesssim 1$ kHz.

Experimentally it should therefore be feasible to resolve individual sites with an uncertainty of a few lattice sites and thus to sharpen the density profile within this uncertainty. Note that this scheme clearly profits from a large number of particles per tube. Another advantage is that it preserves the spherical symmetry of the density distribution in a 3D lattice.

Finally let us remark that this method can easily be incorporated in the continuous filtering scheme [Fig. 3.9] proposed in Sect. 3.2, since there the atoms are also coupled to untrapped states.

3.4 Algorithmic cooling of defects in quantum registers

A perfect one-dimensional quantum register is a connected array of commensurately filled lattice sites. Hence, quantum registers are equivalent to MI states of the form (3.4). For most purposes the filling factor $\nu = 1$ is sufficient. This state appears naturally as the unique MI ground state (3.5) of the BHM in the no-tunnelling limit and in the presence of a weak harmonic confinement. Hence, any efficient ground state cooling protocol will produce a good quantum register. Moreover, we have seen in the previous section, that algorithmic protocols can be used to create an *ensemble* of quantum registers rather than a unique one (see also [44, 64]). In this section we will propose and analyze two alternative algorithms for the creation of a quantum register ensemble. As compared to previous proposals [44, 64] these schemes require only a small number of operations, which makes them more appealing for experimental implementation. The first protocol produces registers with filling $\nu = 1$, whereas the second protocol is optimized for filling $\nu = 2$. In addition, we propose how to transform atoms at the endpoints of each register into "pointer" atoms, which then enables addressing individual lattice sites. This can be used, for instance, to create registers of equal length. Even more important it offers the opportunity to perform ensemble quantum computation in this system.

We start from a rather cold cloud, $\beta U \gg 1$, which has been subject to fundamental filtering operations F_M (3.16). The result is an almost perfect MI in the center of the trap with some residual defects (or holes) which are predominantly localized at the borders [See Fig. 3.6]. Since we operate solely in the no-tunnelling regime these defects cannot redistribute nor evaporate. Our goal is to remove all these defects and we will achieve it by applying nearest-neighbor quantum gates which simulate inelastic collisions between particles and holes. Simply put, whenever a particle sits next to a hole, the particle will be annihilated. This process is analogous to spin flips in ferromagnets and the formation of domains of equal magnetization. Thus, these algorithmic schemes can also be understood as controlled equilibration and cooling of defects.

For all protocols that will be proposed below, the resulting state is a mixture of perfect (up to defects in the central MI phase) quantum registers of the form (3.5), which differ only in their length and lateral position. The entropy of this state will be of the order $S_f \sim \log_2 \Delta$, where the parameter Δ (3.17) quantifies the translational uncertainty in the initial density distribution. Note, however, even though the final entropy is very small, these protocols are typically not suited for ground state cooling. The reason is that the final state is far from thermal equilibrium. Numerically we find that the value of the entropy after equilibration is comparable to the value before invoking the protocol. However, if one makes use of the pointer atoms to select only registers with a specific length then these protocols indeed lead to cooling.

3.4.1 Protocol 1

The operation sequence is illustrated in Fig. 3.16. We first merge oddly aligned pairs of sites using a superlattice [135, 136] and empty sites with

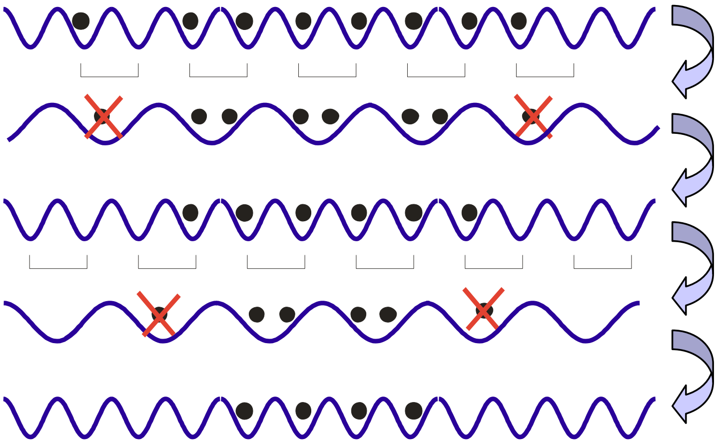

Figure 3.16: Illustration of protocol 1 for the creation of quantum registers. After merging neighboring lattice sites, one empties single occupied sites. The algorithm stops, when all particles in the tails have been removed and only the central MI phase remains.

only one atom. The sites are again split and the original lattice is restored. This operation is then repeated several times, alternating between even and oddly aligned sites, until the *total* entropy reaches a minimum.

We have analyzed the performance of this protocol under realistic conditions using the MPS description to compute the at most classically correlated density matrix [Appendix D]. In Fig. 3.17 we plot the typical density distribution after different steps of the protocol. A single step changes very little the density but decreases dramatically the entropy (From $S_2 = 17.5$ to $S_2 = 7.9$). Indeed, the first steps account for the elimination of most defects. After a few iterations entropy saturates because the density matrix has collapsed to a classical ensemble of defect-free quantum registers [Fig. 3.17]. As a consequence of the protocol, the number of atoms per register must be even, which leads to steps in the final density profile [Fig. 3.17].

Clearly the fix point of this protocol would be a state with no particles at all. Let us now estimate how many iterations M of the protocol are required to reach a state with reasonable particle number and tolerable defect probability. Firstly, we have to point out that there are two sources of defects: (i) holes in the central MI phase and (ii) particles at the borders which are disconnected from the central MI phase and which have not yet been erased by the protocol. The probability for defects of the first kind is negligible in the limit of low temperatures $\beta U \gg 1$ [see Sect. 3.1.2]. Defects of kind (ii) can be assessed by the following observation: In order to erase a connected array of M particles, which is separated by at least one empty site from a central MI

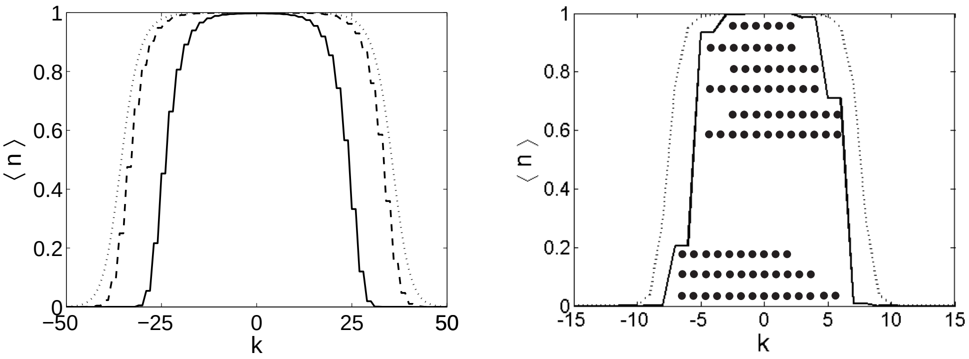

Figure 3.17: Left: Particle distribution after different steps of the protocol: after filtering F_1 (dotted), after one iteration (dashed), after eight iterations (solid). Parameters of the initial state: $N = 100$, $s = 0.7$ ($s_2 = 0.56$), U/b=1000, $\beta U = 5.8$. Parameters after filtering: $\overline{N} = 70.5$, $s = 0.33$ ($S_2 = 17.5$, $s_2 = 0.25$). Parameters after iteration 1: $N = 65.5$, $S_2 = 7.89$, $s_2 = 0.12$; iteration 2: $N = 60.8$, $S_2 = 5.95$, $s_2 = 0.098$; iteration 7: $N = 48.8$, $S_2 = 5.297$, $s_2 = 0.108$; iteration 8: $N = 46.8$, $S_2 = 5.296$, $s_2 = 0.113$. Stopping the algorithm at iteration 3 gives a minimum in the entropy *per* particle: $s_2 = 0.095$. Upon reaching thermal equilibrium this value has increased to $s_2 = 0.265$ ($s = 0.36$) which is comparable to the value after filtering. However, when selecting the subspace containing only registers of length $N = 48$ then the protocol leads to cooling. The entropy per particle in thermal equilibrium will then be given by $s = 0.17$. Right: The step like structure of the density distribution allows one to deduce the states which contribute significantly to the final density matrix. The states can be classified according to their particle number and their lateral position.

state, one requires exactly $M/2$ iterations of the protocol. The probability of finding defects after M iterations is then given by the probability of having states with array size larger than M in the initial density matrix. This probability can easily be computed numerically exact from the distribution (3.8). The derivation of closed expressions is however difficult. Nevertheless, one can get a good estimate for the optimal number of iterations based on the following argument. The characteristic tail width of the initial particle distribution (3.8) is Δ (3.17). Hence, the occurrence of arrays of size $M = 2\Delta$ is already very unlikely. This implies that after roughly Δ iterations of protocol 1 we expect to have registers with negligible defect probability. This can be illustrated with an example. For the initial state in Fig. 3.17 we have $\Delta = 10$ and the relative difference in the total entropy after the seventh and eighth iteration has reduced to 10^{-4}, which implies a defect probability of the same order of magnitude. The typical size of the registers after Δ iterations is roughly $\overline{N} - 2\Delta$, where $\overline{N}$ (3.21) is the characteristic size of the initial MI state. This implies $\overline{N} \gg \Delta$, otherwise no particles remain in the system. Since $\Delta \approx \overline{N}/\beta U$, one has to require the low temperature regime $\beta U \gg 1$.

As mentioned above, the algorithmic ground state cooling protocol of the previous section can also be used for the creation of quantum registers. However, the ground state cooling algorithm involves $\mathcal{O}(\overline{N})$ operations as compared to $\mathcal{O}(\Delta)$ operations of the current protocol. Note also that the example presented in Fig. 3.17 indicates that this protocol does not lead to cooling. After restoring thermal equilibrium, the entropy has reached a value comparable to the one after filtering. We have repeated this analysis for various initial conditions and our results confirm this observation. However, if one selects a particle number subspace with N being larger than the mean value than our protocol can indeed be used for cooling. According to the data in Fig. 3.17 the entropy per particle can be reduced by roughly 50% as compared to filtering.

3.4.2 Protocol 2

We start from a state which contains only empty or doubly occupied sites. This can be achieved by applying filtering operation F_2, followed by $U_{1,0}^{0,1}$ and E_b. The protocol is depicted in Fig. 3.18.

We begin with transferring one particle per site to state $|b\rangle$. Then the $|b\rangle$–lattice is shifted one site to the left and the same operation as before is performed. Afterwards one empties single occupied sites. This procedure allows one to remove defects in a correlated way. Occupied sites which have an unoccupied site to the right are emptied. Since the probability of finding particles in the center is close to one, the central MI is preserved except for losses at the right border. This procedure is repeated until all particle disconnected from the central MI phase become annihilated and only perfect MI phases in the center remain. One step of the protocol can be summarized in the following sequence of operations: $U_{2,0}^{1,1}$, S_{-1}, $U_{2,0}^{1,1}$, E_b, $U_{1,0}^{0,1}$, E_b. Following the discussion of protocol 1, this sequence has to be applied approximately 2Δ times, where Δ denotes again the characteristic tail width of the initial particle distribution. The factor two stems from the fact that at each step of the protocol the size of "particle islands" in the tails, as well as the central MI phase, is reduced only by one as compared to two in protocol 1. The final density matrix looks very similar to the one after protocol 1, with the difference that also registers with odd number of atoms appear.

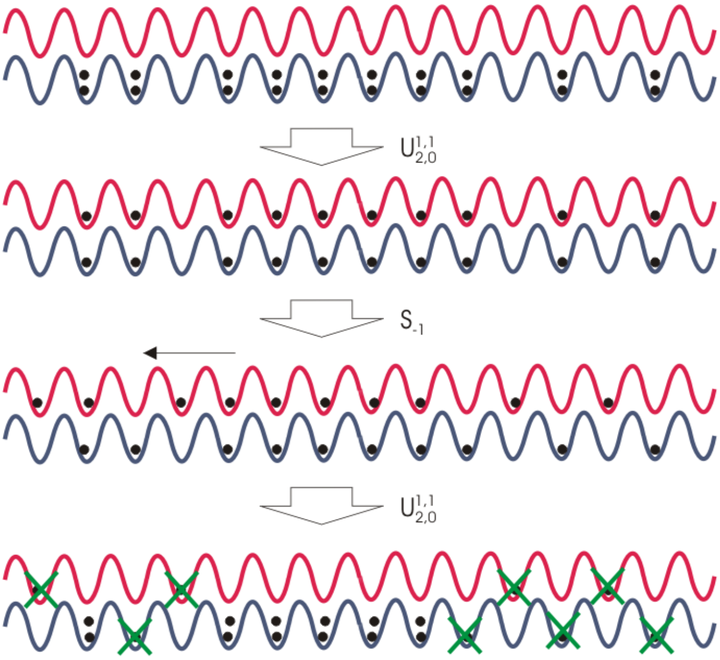

Figure 3.18: Illustration of protocol 2 for the creation of quantum registers. Spin-dependent lattice shifts allow one to remove defects in a correlated way.

3.4.3 Pointer atoms and register length control

Given an ensemble of quantum registers we will now show how to create pointer atoms. To be more precise, our goal is to selectively transfer the two end atoms of each register to a different internal level. These pointer atoms enable single–site addressing which can be used to engineer registers of specific length.

Creation of pointer atoms

Our scheme relies on the same set of operations that is used in current experiments for entangling atoms located at different lattice sites [47]. We consider quantum registers with one atom per site. Initially all atoms are in internal state $|a\rangle$. A Hadamard transformation puts the atoms in the coherent superposition state $(|a\rangle + |b\rangle)/\sqrt{2}$. One then shifts the $|b\rangle$–lattice one site to the right and waits an appropriate time until the on–site interaction between species $|a\rangle$ and $|b\rangle$ yields a collisional π–phase. This means that on each site the state $|a\rangle|b\rangle$ is transformed into $-|a\rangle|b\rangle$. After two lattice shifts to the left one waits again until a π–phase has built up. Then the lattice is shifted back to its original position and a second Hadamard operation is performed. The resulting state is a again a product state but the end atoms have been promoted to level $|b\rangle$. These atoms can be considered as pointer atoms because they mark the beginning (and the end) of each register and can thus be used to access every site within the register in a deterministic way. In practice, only one pointer atom is needed. The second pointer atom, e.g. the one on the left, can easily be removed by applying the following operation sequence: S_{-1}, $U^{2,0}_{1,1}$, E_b, $U^{1,1}_{2,0}$.

Manipulation of register length

The pointer atoms can now be used to create an ensemble of registers of fixed length, a feature which is desired for quantum computation and which can even lead to cooling. We first present a protocol that requires only two internal states of the atoms. Then we show that the algorithm can be simplified considerably when a third internal level is included. In both cases we start from a situation where all registers have one pointer atom in state $|b\rangle$ which is located at the right most occupied site of the register.

Protocol based on two internal states: The central idea is to remove atoms selectively from the system by transferring them to the pointer level $|b\rangle$. We first show how to discard all registers which are shorter than a desired length M. We start with the sequence: $U^{0,2}_{1,1}$, S_{-M}, $U^{2,0}_{0,2}$, E_b. This ensures that registers of length $N \geq M$ are protected against further modifications, because their pointer atoms have been removed. Next we promote atoms in doubly occupied sites to the pointer level and shift this (two–atom) pointer one site to the right. If the pointer hits an occupied site then one atom in $|a\rangle$ will be removed. Iteration of this process removes all atoms on the right of the current pointer position. To be more precise, one has to iterate $M-1$ times the sequence: $U^{0,2}_{2,0}$, S_1, $U^{2,0}_{0,2}$, $U^{2,1}_{1,2}$, E_b. In a last step the remaining doubly occupied sites are emptied via $U^{0,2}_{2,0}$, E_b. After creating new pointer atoms the minimal register length is given by $M' = M-2$. Again we keep only the pointer atom on the right side. Let us now show how to shorten registers of length $N > M'$ to length M'. We first apply the sequence: S_{-1}, $U^{0,2}_{1,1}$, $S_{-M'}$, $U^{1,1}_{0,2}$, S_{-1}. For the target register of length M' this merely transfers one atom from the right end of the register to the left end. For larger registers one obtains a two–atom pointer that can now be used to select and discard all atoms located left of the pointer. This can be accomplished by iterating the sequence: $U^{2,1}_{1,2}$, E_b, $U^{0,2}_{2,0}$, S_{-1} until all registers with appreciable weight in the density matrix have been shortened to the desired size.

Protocol based on three internal states: This protocol is based on the operation $U^{0,1,1}_{1,1,0}$, which transfers an atom from $|a\rangle$ to $|c\rangle$, given that a pointer atom is present. This way one can use the pointer as a "marker", which allows one to produce registers of desired length M in a very simple manner. One first marks an array of M atoms and then discards all atoms which have remained in level $|a\rangle$. The algorithm can be summarized as follows: apply the sequence $S_{-(M-1)}, U_{1,1}^{2,0}, E_b, U_{2,0}^{1,1}, U_{1,1,0}^{0,1,1}$; iterate $M-1$ times the sequence $S_1, U_{1,1,0}^{0,1,1}$; finally apply the operation E_a.

3.5 Perspectives

We have proposed various ground state cooling schemes that allow one to reduce the temperature in current optical lattice setups considerably. A special virtue of our schemes is, that they rely on general concepts which can easily be adapted to different experimental situations. For instance, little modifications ensure that our protocols can be applied both to bosonic and fermionic systems. A second advantage of our protocols is, that they are designed for the no–tunnelling regime and hence do not necessarily require equilibration processes induced by particle hopping and elastic collisions. As a consequence, the time to approach a state close to the ground state does not increase with decreasing initial temperature, rather the opposite is the case.

In this sense, the collection of cooling schemes presented in this chapter can be considered as a toolbox which is tailored for cooling atoms in optical lattice setups. The tool (or combination of tools) which is best suited for a given purpose, can be chosen according to the characteristic features of a specific experimental setup. For instance, in the case of large systems at high temperatures, one can think of combining filtering with the frequency knife method which is then followed by the algorithmic ground state cooling protocol. Or ground state cooling can be combined with adiabatic transformation of the Hamiltonian so as to produce ground states of models different from the simple Bose-Hubbard considered here. And one should also keep in mind that a 3D lattice structure offers a large variety of possibilities, which have not been fully explored yet.

The methods introduced here greatly enhance the potential of optical lattice setups for future applications and might pave the way to the experimental realization of quantum simulation and quantum computation in this system. We also hope that the concepts introduced in this work might trigger further research in the direction of ground state cooling in optical lattices.

Chapter 4

Adiabatic Path to Fractional Quantum Hall states in Cold Atomic Systems

The creation of highly entangled multi-particle states is one of the most challenging goals of modern experimental quantum mechanics. In this respect atomic systems offer a very promising arena in which entangled states can be created and manipulated with a high degree of control. The experimental difficulty increases, however, with the number of particles that are to be entangled, since the system becomes then more sensitive to decoherence. Starting with a small number of particles as a first step, important achievements have been already obtained in the creation of atomic entangled states. For example, in recent experiments with trapped ions, entangled states of up to 8 ions have been demonstrated [4, 5]. Moreover, in experiments with neutral bosonic atoms in optical lattices Bell-type states have been created by accurately controlling the interactions between neighboring atoms [47]. As a typical feature of most of the experimentally realized entangled states, atoms get entangled through their internal degrees of freedom, keeping separable their motional part.

In this chapter we develop a scheme to create *motional* entangled states of a small number of atoms in an actual experimental setup with an optical lattice. These states are a sequence of fractional quantum Hall (FQH) states, analogous to the ones that appear in the context of the fractional quantum Hall effect [48, 137]. In contrast to typical atomic entangled states, the particles are here entangled in real space, and not in internal space. This peculiarity makes them specially interesting, for it represents a novel nature of atomic entanglement.

The possibility of creating FQH atomic states as the Laughlin state by rapidly rotating the trap confining the atoms has been discussed in several theoretical works [50, 51, 52, 53, 54, 55, 56, 57, 58]. However, experiments dealing with typically large number of particles have not yet succeeded in reaching these states. Here, we fully address the case of a small number of particles and design a realistic way of entangling them into FQH states. The experimental setup that we have in mind corresponds to a situation in which a Bose-Einstein condensate is loaded in a deep optical lattice. When the lattice depth is very large tunnelling between different sites is strongly suppressed and the system can be treated as a lattice of independent wells, each of them with a small number of particles. By independently rotating each of these 3D wells [138] the lowest Landau level (LLL) regime can be achieved for each copy. We have studied the problem exactly within the LLL for $N = 2, N = 3$ and $N = 4$ particles per well. The main results of this chapter can be summarized as follows:

(i) For the most interesting case of four atoms we have identified the following sequence of highly entangled stable ground states: the Pfaffian state [139], the 1/2-Laughlin quasiparticle [49] and the 1/2-Laughlin state [49]. The 1/2-Laughlin quasiparticle state (which had never been identified before in an atomic system) is particularly interesting. It is the counterpart of the 1/2-Laughlin quasihole found in [57] and contains a 1/2-anyon.

(ii) Exact knowledge of the spectrum of the system has allowed us to design adiabiatic paths to these states by simultaneously rotating and deforming each of the wells. All parameters and evolution times lie well within the reach of present experimental setups.

(iii) We discuss how to detect these entangled states by measuring different properties, such as their density profile, angular momentum or correlation functions. In particular, we propose a novel technique based on the lattice setup to measure the density-density correlation function of these strongly correlated states. Even though the number of atoms per well is small, the lattice setup allows one to have multiple copies of the system, so that the experimental signal is highly enhanced.

(iv) In Appendix E we study the problem of two interacting particles in a harmonic trap analytically. In particular, we derive a condition for the validity of the pseudo-potential approximation in tight traps, i.e. when the scattering length becomes larger than the typical trap size.

We point out that our findings also show that adiabatically achieving FQH states for rapidly rotating traps with a large number of particles turns out to be very challenging. The reason is that all relevant experimental parameters scale linearly with the number of particles. Nevertheless, we hope that our results can shed some light on the problems that these current experiments are dealing with, and even may pave the way to new methods of achieving FQH multi-particle entangled states.

4.1 Identification of entangled states

We consider a system of bosonic atoms loaded in a 3D optical lattice. We assume a commensurate filling of N atoms per lattice site [1], and a large value of the lattice depth $V_0/E_R \gg 1$, where $E_R = \hbar^2 k^2/2M$ is the recoil energy, k is the wave vector of the laser lattice light, and M the atomic mass. In this limit the lattice can by treated as a system of independent 3D harmonic wells, each of them having N atoms and a trapping frequency $\omega \approx \sqrt{V_0 E_R}$.

Let us rotate each of these 3D harmonic wells around the direction x_3 with frequency Ω. We will identify a sequence of motional entangled ground states of the N atoms that appear as the frequency Ω is increased. We will assume the limit of rapid rotation [57]. In this case the motion in the x_3 direction is frozen, and the motion in the plane of rotation x_1, x_2 is restricted to the LLL [Appendix E]. This implies that in order to project the system onto the LLL we do not need to start with a 2D configuration (as it is the case in previous proposals [50, 51, 52, 53, 54, 55, 56]), since the fast rotation itself restricts the motion in the direction of the rotation to zero point oscillations. The system is then governed by a two dimensional effective Hamiltonian, which written in units of $\hbar\omega$ has the form:

$$H = (1 - \Omega/\omega)\, L + 2\pi\ \eta V, \tag{4.1}$$

where $L = \sum_{m=0} m\, a_m^\dagger a_m$ is the angular momentum operator in the x_3 direction, and $V = \sum_{m_1,m_2,m_3,m_4} V_{m_1,m_2}^{m_3,m_4} a_{m_1}^\dagger a_{m_2}^\dagger a_{m_3} a_{m_4}$ is the interaction operator. Here the bosonic operator $a_m^\dagger (a_m)$ create (anihilate) an atom in the state $|m\rangle$ of the LLL with well defined x_3 component of the angular momentum m. The wave functions of the LLL in complex coordinates read

$$\varphi_m(z) = \langle z|m\rangle = \frac{1}{\sqrt{\pi m!}\ell}\ z^m e^{-|z|^2/2}\ , \tag{4.2}$$

where $z = (x_1 + ix_2)/\ell$, $\ell = \sqrt{\hbar/M\omega}$ is the harmonic oscillator length, and $m = 0, 1, \ldots \infty$. Assuming contact interactions between the atoms the

---

[1] Typically the filling factor N is not homogeneous, because the Gaussian intensity profile of the laser beams results in an additional weak harmonic confinement of the atoms. However, it has been demonstrated that commensurate filling can be achieved using an entanglement interferometer [129]

interaction coefficients are:

$$V_{m_1,m_2}^{m_3,m_4} = \frac{(m_1+m_2)!}{2^{m_1+m_2}\sqrt{m_1!m_2!m_3!m_4!}} \,. \tag{4.3}$$

In Hamiltonian (4.1) we have introduced the important interaction parameter $\eta = \sqrt{2/\pi} a_s/\ell$, with a_s being the 3D scattering length. Our analytical calculations in Appendix E for scattering potentials of finite size b show that the pseudo-potential approximation, which underlies Eq. 4.3, is also valid for tight traps with $a_s \gtrsim \ell$ given that $b a_s \ll \ell^2$ and $b \ll \ell$ are fulfilled.

4.1.1 *N=2*

The problem of two interacting particles in a rotating harmonic trap can be solved analytically [Appendix E]. Here we summarize the main results. The Hamiltonian (4.1) is diagonal in the states $|m_r, m_{cm}\rangle$ of well defined relative (m_r) and center of mass (m_{cm}) angular momentum:

$$H = \sum_{m_r,m_{cm}} E_{m_r,m_{cm}} |m_r, m_{cm}\rangle\langle m_r, m_{cm}|, \tag{4.4}$$

with $E_{m_r,m_{cm}} = \delta_{m_r,0}\,\eta + (1-\Omega/\omega)(m_r + m_{cm})$. We note that due to the restriction to s-wave scattering, only particles with zero relative angular momentum feel the interaction energy. Moreover we have assumed the weak interaction limit $\eta \ll 1$. It follows that for $\Omega/\omega < 1 - \eta/2$ the ground state of the system is $|0,0\rangle$ (with total angular momentum $L=0$), which is not entangled, whereas for $\Omega/\omega > 1-\eta/2$ the state $|2,0\rangle$ (with $L=2$) becomes energetically favorable [Fig. 4.1a]. This state,

$$\langle z_1, z_2|2,0\rangle \propto (z_1 - z_2)^2\, e^{-|z_1|^2/2} e^{-|z_2|^2/2}, \tag{4.5}$$

is clearly entangled since it cannot be written as a product of two single particle wave functions. It is the Laughlin state $|\psi_L\rangle$ for two particles at filling factor $\nu = 1/2$ [49]. In order to quantify the entanglement of this state we write it in the basis of states $|m_1 m_2\rangle$ with well defined single-particle angular momentum. Then the Laughlin state takes the form of a pure two qutrit state: $|\psi_L\rangle = \frac{1}{2}\left(|02\rangle + |20\rangle\right) - \frac{1}{\sqrt{2}}|11\rangle$. This is already the Schmidt decomposition of the state, and the entropy of entanglement [84] can immediately calculated to be $E(|\psi_L\rangle) = 1.5$. This value is close to $\log_2 3$, corresponding to a maximally entangled pure two qutrit state.

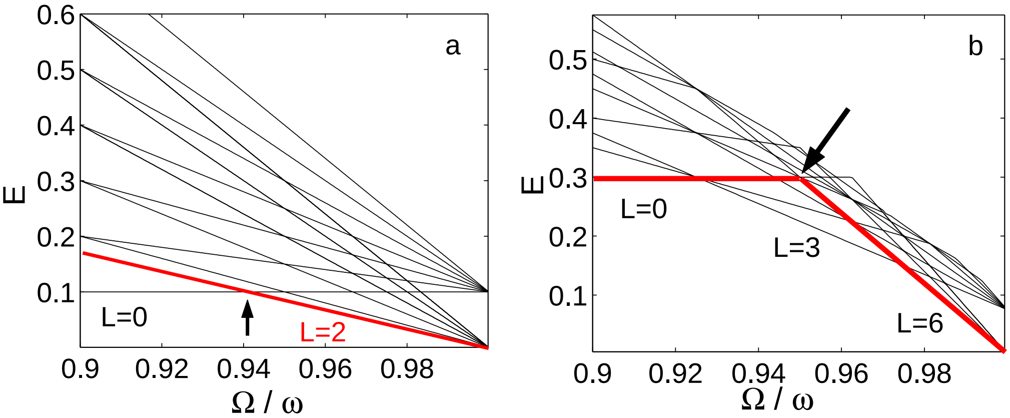

Figure 4.1: Energy spectrum (in units of $\hbar\omega$) of the Hamiltonian 4.1 for $\eta = 0.1$ as a function of the trap rotation frequency Ω/ω. (a) $N = 2$: At $\Omega = 0.95\omega$ we observe a level crossing between the Gaussian ground state (L=0) and the Laughlin state (L=2). (b) $N = 3$: The ground state sequence involves a state with odd angular momentum ($L = 3$). In order to reach the $L = 6$ Laughlin state with the perturbation (4.9) we will later design an adiabatic path via excited states (red line). The arrow marks the level crossing between the $L = 0$ and the $L = 6$ state.

4.1.2 *N=3*

The case of three particles per lattice well cannot be solved analytically. Therefore we resort to exact numerical diagonalization in order to obtain the multi-particle energy spectrum of the Hamiltonian (4.1). We find that the 1/2-Laughlin state ($L = 6$) emerges as ground state after an intermediate state with odd angular momentum $L = 3$ [Fig. 4.1b]. As we will explain in the next section, ground states with odd angular momentum cannot be reached using our proposal. Hence we are forced to design appropriate adiabatic paths via excited states, in order to reach the Laughlin state.

4.1.3 *N=4*

As the frequency of rotation Ω increases the ground state of the system passes through a sequence of states with increasing and well defined total angular momentum $L = 0, 4, 8, 12$ [Fig. 4.3]. These states can be identified as follows: The state with $L = 0$ is a non-entangled state in which all the atoms are condensed in the single-particle Gaussian state with angular momentum $m = 0$. The first nontrivial ground state is the $L = 4$ state. This state is not,

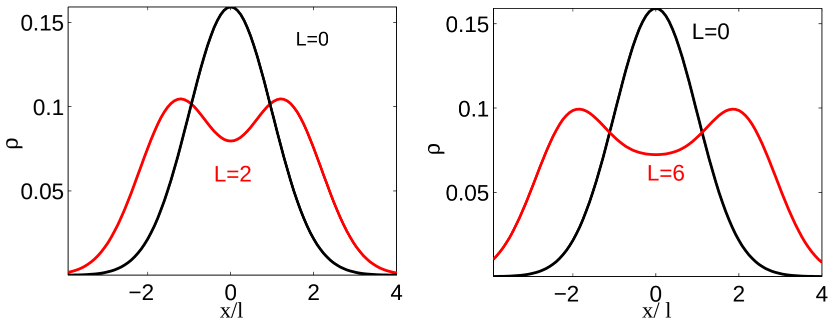

Figure 4.2: Density profile $\rho(x, y = 0)$ of the Laughlin state (red) as compared to the Gaussian ground state ($L = 0$). (a) $N = 2$. (b) $N = 3$. Note that the spatial width of the distribution increases with N.

as one might expect, a single vortex state, in which all the particles would be condensed in the single particle state $m = 1$. In contrast, this state is highly entangled and is very close (fidelity $\mathcal{F} = |\langle\psi|\psi_{Pf}\rangle|^2 = 0.95$) to the well-known Pfaffian state:

$$\psi_{Pf}([z]) = \prod_{i<j}^{4}(z_i - z_j)\ \mathrm{Pf}\left(\frac{1}{z_i - z_j}\right) . \tag{4.6}$$

This state is specially interesting, also in the context of quantum information theory, because its elementary excitations are known to exhibit non-abelian statistics [10]. The next stable state in row ($L = 8$) can be very well characterized (fidelity $\mathcal{F} = 0.98$) by a Laughlin quasiparticle state:

$$\psi_{QP}([z]) = \frac{\partial}{\partial z_1} \cdots \frac{\partial}{\partial z_4}\ \psi_L . \tag{4.7}$$

This state is the counterpart of the quasihole excitation, which has previously been studied in the context of 1/2-anyons in rotating Bose-Einstein condensates [57]. Finally, the last stable state is identical to the $\frac{1}{2}$-Laughlin state, which we have already encountered in the case of two particles per well:

$$\psi_L([z]) = \prod_{i<j}^{4}(z_i - z_j)^2 \prod_{k}^{4} e^{|z_k|^2/2} . \tag{4.8}$$

This state is an exact eigenstate of (4.1) with zero interaction energy. In Fig. 4.3 we have plotted the density distribution in the x_1, x_2 plane of the different stable ground states. As the frequency of rotation Ω/ω increases the wave function spreads, and the interaction between the atoms decreases.

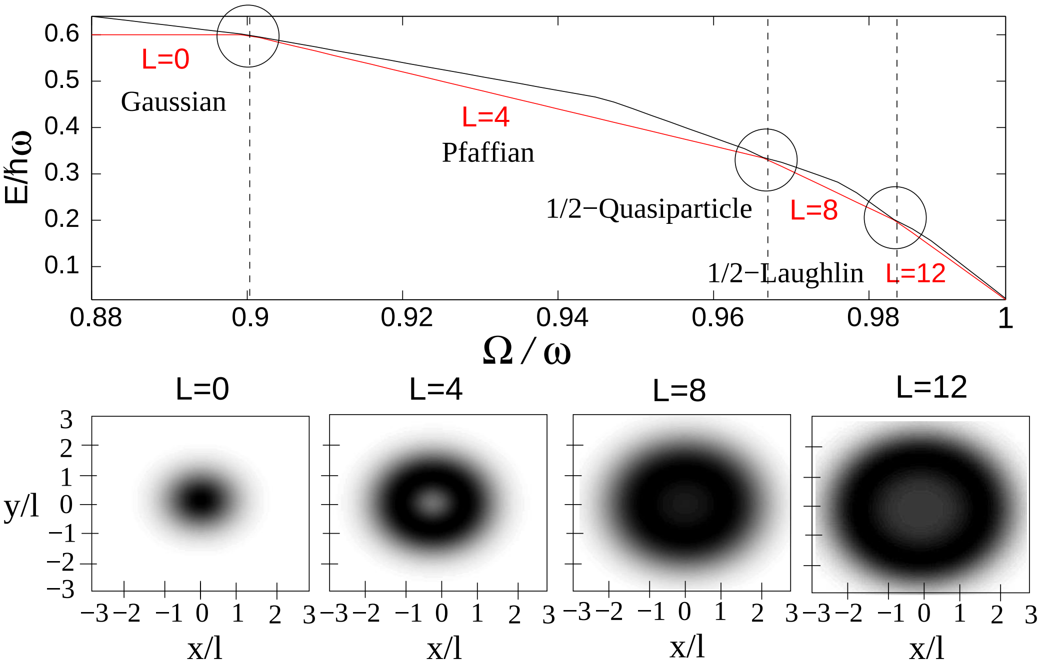

Figure 4.3: Lowest two eigenenergies (in units of $\hbar\omega$) of the Hamiltonian (4.1) for 4 particles and $\eta = 0.1$ as a function of the trap rotation frequency Ω/ω. The circles mark the level crossings and L denotes the total angular momentum of the ground state. The ground state sequence can be identified as follows (with fidelity $\mathcal{F} = |\langle\psi|\psi'\rangle|^2$ given in brackets): L= 0 Gaussian ground state (exact) , L=4 Pfaffian state (0.95), L=8 quasiparticle state (0.98), L=12 Laughlin state (exact). The change of angular momentum can readily be obtained from the increasing width of the density distribution depicted below.

4.2 Adiabatic paths to entangled states

The sequence of entangled states we have described above cannot be obtained by simply adiabatically increasing the frequency of rotation Ω. The reason for that is the rotational symmetry which leads to level crossings between different angular momentum states [Fig. 4.3]. In order to pass adiabatically from the zero angular momentum ground state to higher angular momentum states the spherical symmetry of the trapping potential has to be broken. For our optical lattice setup this can be achieved for example by deforming the formerly isotropic trapping potential on each well and letting the deformation rotate with frequency Ω [138]. In the rotating frame the new trapping potential has the form $V_p \propto (\omega + \Delta\omega)^2\, x_1^2 + \omega^2 x_2^2$, and the new Hamiltonian is $H + H_\epsilon$, with

$$H_\epsilon = \frac{\epsilon}{4} \sum_m \beta_m a^\dagger_{m+2} a_m + (m+1) a^\dagger_m a_m + \text{h.c.}, \tag{4.9}$$

where $\beta_m = \sqrt{(m+2)(m+1)}$ and $\epsilon = \Delta\omega/\omega$ is a small parameter. The perturbation (4.9) leads to quadrupole excitations, which means a change in angular momentum by two quanta.

4.2.1 *N=2* and *N=4*

We first consider the cases of two and four particles per well. In order to design appropriate adiabatic paths to the entangled states described above, we have computed numerically the energy gap between the ground and first excited state as a function of the parameters Ω/ω and ϵ for $N = 2$ and $N = 4$ [Fig. 4.4].

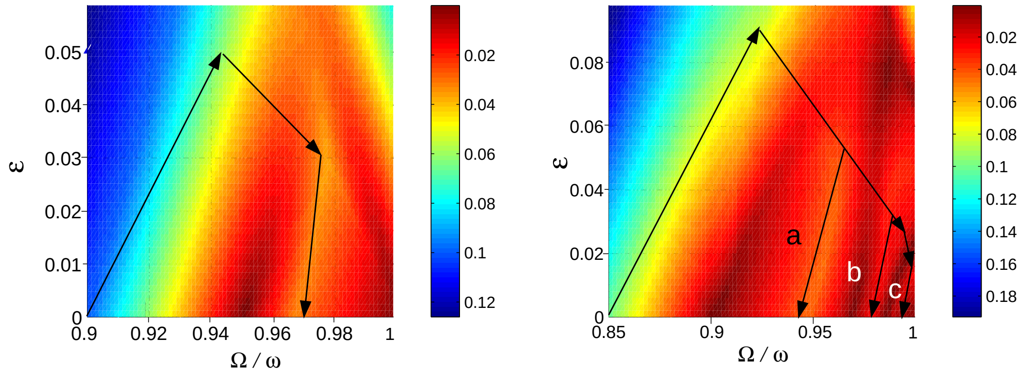

Figure 4.4: Energy gap (in units of $\hbar\omega$) between the ground and first excited state as a function of the rotation frequency Ω/ω and the trap deformation ϵ for an interaction strength $\eta = 0.1$. The black lines mark appropriate paths in parameter space for adiabatic ground state evolution starting from the $L = 0$ state. The adiabatic evolution times have been calculated for a typical trapping frequency $\omega \simeq (2\pi)30$ kHz. Left ($N = 2$): For a final fidelity $\mathcal{F} = |\langle\psi(T)|\psi_L\rangle|^2 = 0.99$ the Laughlin state (L=2) can be reached within $T = 6.5$ ms. Right ($N = 4$): Adiabatic path, evolution time T and fidelity $\mathcal{F}$ for the following final states (see Fig. 4.3): (a) Pfaffian state: $T = 8$ ms, $\mathcal{F} = 0.99$; (b) Quasiparticle state: $T = 12$ ms, $\mathcal{F} = 0.99$; (c) Laughlin state: $T = 215$ ms, $\mathcal{F} = 0.97$.

We first note that the isolines of constant energy gap show an approximately linear behavior. This feature can be easily understood from a perturbative treatment of the Hamiltonian (4.9). To first order, the energy of states with angular momentum L is shifted by an amount $\epsilon L/4$. Therefore the gap profile for a given ϵ is very similar to the one for $\epsilon = 0$ but shifted an amount $\sim \epsilon$ to larger rotation frequencies. As expected, we find that for $\epsilon \neq 0$ avoided crossings emerge (see Fig. 4.5). The energy gap of the avoided crossings does, however, not in general increase monotonically with the deformation ϵ. Due to the interplay with other excited states, "saddlepoints" appear in the gap profile, which makes the design of appropriate adiabatic paths a nontrivial task. For the stable entangled states of $N = 2, 4$ identified above these paths are depicted in Fig. 4.4. The actual time needed for the adiabatic path depends on the number of particles as well as on the state we want to achieve. For a typical trapping frequency $\omega = (2\pi)30$ kHz and an interaction coupling $\eta = 0.1$, the evolution times for the $N = 2$ Laughlin state as well as for the $L = 4$ and $L = 8$ states for $N = 4$ are of the order of 10 ms. In contrast, the evolution time for the $N = 4$ Laughlin state is one order of magnitude larger.

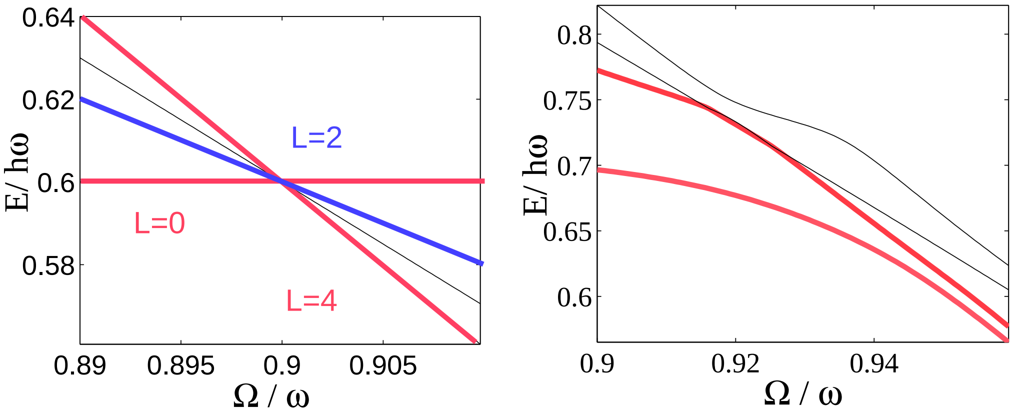

Figure 4.5: Left side: Energy spectrum (in units $\hbar\omega$) for N=4 and $\eta = 0.1$ in the vicinity of the first level crossing from the L=0 to the L=4 state (see Fig. 4.3 left circle). Using quadrupole excitations ($|\Delta L| = 2$) coupling between these states is provided by the intermediate state L=2. Right side: Emergence of an avoided level crossing for a trap deformation $\epsilon = 0.06$.

We can understand this result in the following way. For the case of $N = 2$ direct coupling of the $L = 0$ state to the $L = 2$ Laughlin state is mediated by (4.9). For the case of $N = 4$ there is no direct coupling between the ground states, since their angular momenta differ by 4. But, as one can see from the spectrum in the vicinity of the crossing to the state $L = 4$ [Fig. 4.5], there is a state with $L = 2$ near the crossing that mediates the coupling between the $L = 0$ and the $L = 4$ state. A similar situation occurs for the crossing to the $L = 8$ state. However, there is no such intermediate state in direct proximity of the crossing to the $N = 4$ Laughlin state, which leads to a decrease of the energy gap by one order of magnitude.

4.2.2 *N=3*

The case of $N = 3$ is somehow special, because here a ground state with odd angular momentum ($L = 3$) arises [Fig. 4.1b]. From the nature of the perturbation (4.9) it is clear that ground state evolution is not possible, because angular momentum can only be increased by multiples of two quanta. However, one can design appropriate adiabatic paths via excited levels in order to reach the 1/2-Laughlin state. We first increase the rotation frequency without deforming the trap until we are in the vicinity of the level crossing between the $L = 0$ and the $L = 6$ (Laughlin) state [Fig. 4.1b]. We then switch on the perturbation and follow the adiabatic path in parameter space depicted in Fig. 4.6. The required evolution time for a final fidelity $\mathcal{F} = |\langle\psi(T)|\psi_L\rangle|^2 = 0.99^2$ is $T \approx 15$ ms.

4.3 Feasibility

Let us now discuss the experimental feasibility of our proposal for a small number of particles N. The crucial assumption in our scheme is the absence of tunnelling between wells resulting in independent 3D harmonic wells. This requires the overlap between Wannier functions on neighboring sites to be small, which can be achieved by increasing the laser intensity. For a single occupied band (small rotation frequency) the assumption of independent wells (Mott regime) is well justified for a laser intensity of $V_0 \approx 20\ E_r$ [24]. With increasing rotation frequency higher angular momentum states of the LLL manifold can be occupied. In the laboratory frame of the lattice this corresponds to the occupation of higher bands. In order to obtain a bound on the required laser intensity for the setup [24] we consider the limiting case of the Laughlin state ($\Omega \approx \omega$). As a rough estimate we require for a given N that the radius of the highest occupied angular momentum single particle state ($\approx \sqrt{2N-1}\ell$) is much smaller than the separation between lattice sites ($a = \pi/k$). In terms of the laser intensity this translates to the condition:

$$(V_0/E_R)^{1/4} \gg \sqrt{2N-1}/\pi\ . \tag{4.10}$$

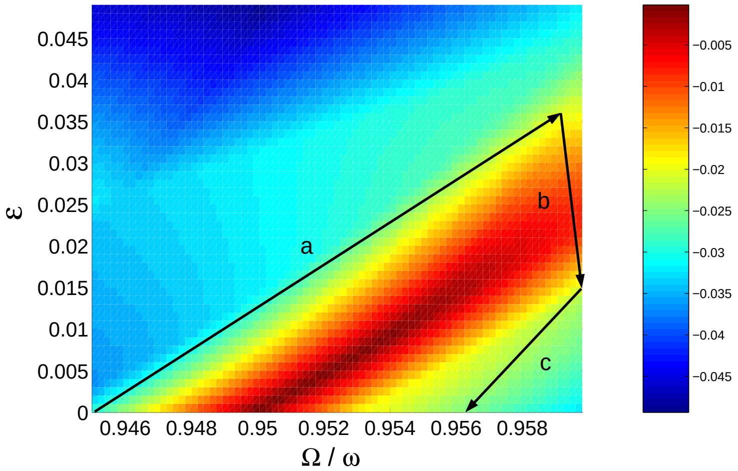

Figure 4.6: Energy gap (in units of $\hbar\omega$) between the fourth and sixth energy level for $N = 3$ and $\eta = 0.1$ as a function of the rotation frequency Ω/ω and the trap deformation ϵ. The fifth energy level involves a state with odd angular momentum and hence is decoupled from states with even angular momentum. The adiabatic evolution times T have been calculated for a typical trapping frequency $\omega \simeq (2\pi)30$ kHz. The black line marks the path in parameter space for adiabatically driving the system from the $L = 0$ ground state to the $L = 6$ (Laughlin) state: (path a) $\Omega/\omega = 0.945 \to 0.959$, $\epsilon = 0 \to 0.035$, $T = 0.7$ ms; (path b) $\Omega/\omega = 0.959 \to 0.96$, $\epsilon = 0.035 \to 0.015$, $T = 12.7$ ms; (path c) $\Omega/\omega = 0.96 \to 0.956$, $\epsilon = 0.015 \to 0$, $T = 1.5$ ms; fidelity with Laughlin state $|\langle\psi(T)|\psi_L\rangle|^2 = 0.99^2$.

Numerical calculations of hopping and on-site interaction matrix elements have confirmed that indeed for $N = 2(4)$ and $V_0/E_R \gtrsim 30(50)$ hopping becomes negligible and wells can be treated independently. We further note that these lower bounds for the laser intensity, which can very well be achieved experimentally, also guarantee the validity of the harmonic approximation.

A second important assumption of our proposal is the projection to the LLL manifold. This implies that the typical energies per particle have to be much smaller than the energy gap to the next Landau level, $\hbar\omega$. For the limiting cases of the $L = 0$ state and the Laughlin state, this leads to the conditions $(N-1)\eta/2, (N-1)(1-\Omega/\omega) \ll 1$, which are easily fulfilled for typical interaction strengths ($\eta \sim 0.1$) and small N.

Finally, in order to adiabatically achieve the entangled states identified above further conditions are required. We analyze the most restrictive case, which corresponds to the Laughlin state. First of all the frequency of rotation has to be very close to the centrifugal limit. Let us find a lower bound to the critical rotation frequency at which the crossing to the Laughlin state appears. This can be done by calculating the rotation frequency at which the Laughlin quasiparticle state, $\psi_{QP}([z]) = \frac{\partial}{\partial z_1} \cdots \frac{\partial}{\partial z_N}\, \psi_L$, becomes equal in energy to the Laughlin state. Since the quasiparticle state has N units of angular momentum less than the Laughlin state and an interaction energy $\lesssim \eta$, it follows that $\Omega_c/\omega \geq 1 - \eta/N$. For the cases of $N = 2(4)$ this condition is in agreement with the exact values found above. Secondly, the evolution time required for the adiabatic path has to be much smaller than the typical decoherence time. We can estimate this time in the following way. Given the critical frequency above and that the position of the avoided crossing is displaced to larger rotation frequencies an amount proportional to ϵ it follows that the maximum ϵ we can have is $\sim \eta/N$, corresponding to a rotation frequency $\Omega/\omega = 1$. Assuming an energy gap $\approx \epsilon$ it follows that the typical evolution time scales as N/η. For the case of $N = 2(4)$ and typical η and ω these times are of the order of tens of miliseconds as exactly found above, which is much smaller than the typical life time of the lattice states. Finally, a high degree of control of the parameters Ω/ω and ϵ is required to perform the appropriate adiabatic paths. The required precision scales again as η/N, which for the case of $N = 4$ means a control of the parameter space up to the second digit.

From our analysis it follows that the adiabatic creation of the Laughlin state by means of low angular momentum excitations, as quadrupole excitations, becomes very difficult in samples with large number of particles [140, 141]. Even if the centrifugal limit is possible to achieve, as it happens when including an additional r^4 trapping potential [141], the adiabatic creation of the Laughlin state is still very demanding. One reason is that the rotation frequency and the trap deformation have to be controlled within a precision that also scales linearly with N. Furthermore we point out that only the exact knowledge of the multi-particle energy spectrum allows one to design adiabatic paths that minimize the evolution time.

4.4 Detection

In this section we consider the important issue of experimental detection by measuring different characteristic properties of the entangled states identified above. As an important feature of our lattice setup of independent wells, we note that any signal will be highly enhanced by a factor equal to the number of occupied lattice sites ($\sim 150,000$ [24]).

i) *Density profiles.* A very characteristic feature of our entangled states can be found in the density profiles. Due to their large angular momentum they exhibit a strongly extended spatial density distribution compared to the non-entangled $L = 0$ state. For the 1/2-Laughlin state the typical radius is given by $\bar{r} \approx \sqrt{2N-1}\,\ell$. In the case of $N = 2(4)$ this results in a radius that is $\sim 2(3)$ times larger than in the case of the condensate. As proposed in [142] the density profile of states within the LLL can be measured in a time of flight (TOF) image of the atomic system, since the momentum distribution coincides with the density profile for LLL states. In our case of independent 3D wells, a TOF absorption picture after expansion time t will exhibit a broad central peak of the form:

$$\rho(\mathbf{r},t) \approx \frac{N_s}{(\omega t)^3}\,|\rho_0(-iz/(\omega t), x_3/(\omega t)|^2\ . \tag{4.11}$$

Here, $\rho_0(z, x_3)$ is the initial density distribution on a single well. In the TOF image it is enhanced by a factor proportional to the number of lattice sites N_s and rescaled by a factor $\omega t \gg 1$. The $\pi/2$ rotation $z \to -iz$ leaves isotropic states, like the FQH states described above, unaffected. The underlying assumption of free (interactionless) expansion is justified, since the interaction energy is small compared to the kinetic energy (in the stationary frame).

ii)*Angular momentum.* For any state within the LLL integration over the density distribution gives $\int d\mathbf{r}\ r^2\rho(\mathbf{r}) = L + N$. Thus in the limit of weak interaction the total angular momentum can be extracted directly from the TOF picture.

iii)*Correlation functions.* Here we propose a novel technique that makes directly use of the rich possibilities offered by the optical lattice setup and which allows to measure both the

$$g_1(\mathbf{r},\mathbf{r}') = \langle\psi^\dagger(\mathbf{r})\psi(\mathbf{r}')\rangle, \tag{4.12}$$

and the

$$g_2(\mathbf{r},\mathbf{r}') = \langle\psi^\dagger(\mathbf{r})\psi^\dagger(\mathbf{r}')\psi(\mathbf{r})\psi(\mathbf{r}')\rangle \tag{4.13}$$

correlation functions. The g_2 correlation function is for instance very characteristic for a Laughlin state. Since particles can only be at least in relative angular momentum $m_r = 2$ it follows that $g_2 \propto |r - r'|^4$. This behavior reveals the $\frac{1}{2}$-fractional nature of this Laughlin state.

We consider two species a and b (hyperfine levels) of bosonic atoms, which can be coupled via Raman transitions. We start with atoms in level a and create the entangled state of interest $|\Psi_i\rangle$ with the method described above. Next we apply a $\pi/2$-pulse with the laser and create an equal superposition of a and b states. Finally, we shift the lattice potential trapping atoms of type b (as proposed in [46] and realized in [47]) by a distance $\mathbf{r_0}$ small compared to the lattice spacing and perform another $\pi/2$-pulse. In the Heisenberg picture this procedure corresponds to the following transformation of the field operator for species a:

$$\psi_a(\mathbf{r}) \rightarrow \psi_a(\mathbf{r}) + \psi_a(\mathbf{r} + \mathbf{r_0}) \ . \tag{4.14}$$

Thus the density distribution of atoms of type a in this new state $|\Psi_f\rangle$ contains information about the g_1 correlation function of the original state:

$$\begin{aligned} &\langle\Psi_f|\psi_a^\dagger(\mathbf{r})\psi_a(\mathbf{r})|\Psi_f\rangle = \\ &\langle\Psi_i|(\psi_a^\dagger(\mathbf{r}) + \psi_a^\dagger(\mathbf{r}+\mathbf{r_0}))(\psi_a(\mathbf{r}) + \psi_a(\mathbf{r}+\mathbf{r_0}))|\Psi_i\rangle \ . \end{aligned} \tag{4.15}$$

Using this procedure we can also measure higher order correlation functions like g_2. In this case measuring the interaction energy of the final state will allow us to calculate the g_2 of the initial state. For instance, for the Laughlin state we find:

$$\begin{aligned} E_{int}(\mathbf{r_0}) &= \frac{\pi\eta}{4}\int d\mathbf{r}\langle\Psi_i|\psi_a^\dagger(\mathbf{r})\psi_a^\dagger(\mathbf{r}+\mathbf{r_0})\psi_a(\mathbf{r})\psi_a(\mathbf{r}+\mathbf{r_0})|\Psi_i\rangle \quad (4.16) \\ &= \frac{\pi\eta}{4}\int d\mathbf{r} \ g_2(\mathbf{r}, \mathbf{r}+\mathbf{r_0}). \end{aligned}$$

The interaction energy is, unfortunately, not directly accessible experimentally. However, the total energy of the final state can be obtained from integrating over the TOF absorption picture, since energy is conserved during the time of flight. For small coupling η, however, the measurable effect due to interactions will be small compared to the kinetic part of the energy. In addition, the kinetic energy itself shows a significant dependence on the shifting r_0, which has to be distinguished from the interaction. Hence, we propose to tune the scattering length a_s (e.g. via a photo association induced Feshbach resonance [143]) and to measure the interaction energy both in the weak and strong scattering limit. The difference would then reveal the characteristic behavior of the g_2 correlation function.

We finally note that, as a further way of detection for the $N = 4$ Laughlin state, a strong reduction of the three body losses should be observed.

Appendix A

Proof of the lower bound on LE

A.1 Theorem on connected correlation functions and local measurements

Here we present the proof of the following theorem:
Given a (pure or mixed) state ρ of N qubits with connected correlation function Q^{ij}_{AB} (2.22) between the spins i and j and directions $\vec{a}, \vec{b}$, then there always exists a basis in which one can locally measure the other spins such that this correlation does not decrease, on average.
Proof:
Using the notation of Sect. 2.4 we have to show that there exists a measurement $\mathcal{M}$ such that:

$$|Q^{ij}_{AB}(\rho^{ij})| \leq \sum_s p_s |Q^{ij}_{AB}(\rho^{ij}_s)|. \tag{A.1}$$

To this end let us first consider mixed states of three qubits. A mixed 3-qubit density operator can be parameterized by four 4×4 blocks

$$\rho = \left[\begin{array}{cc} \rho_1 & \sigma \\ \sigma^\dagger & \rho_2 \end{array} \right]. \tag{A.2}$$

Since local unitary operations can be absorbed in ρ it is sufficient to consider the Q^{12}_{zz} correlations. Thus, the original correlations are completely determined by the diagonal elements of the reduced density operator $\rho_1 + \rho_2$. A von Neumann measurement in the basis

$$\begin{aligned} |+\rangle &:= \cos(\theta/2)|0\rangle + \sin(\theta/2)e^{i\phi}|1\rangle, & \text{(A.3)} \\ |-\rangle &:= -\sin(\theta/2)e^{-i\phi}|0\rangle + \cos(\theta/2)|1\rangle, & \text{(A.4)} \end{aligned}$$

on the third qubit results in the hermitian unnormalized 2-qubit operators

$$\begin{aligned} X_\pm \;&:=\; \langle \pm|\rho|\pm\rangle = \frac{\rho_1+\rho_2}{2} \pm \cos(\theta)\frac{\rho_1-\rho_2}{2} \\ &\pm \sin(\theta)\left(\cos(\phi)\frac{\sigma+\sigma^\dagger}{2} + \sin(\phi)\frac{i(\sigma-\sigma^\dagger)}{2}\right), \end{aligned} \tag{A.5}$$

with probabilities $p_\pm = \mathrm{Tr}(X_\pm)$ conditioned on the outcome $\{+\}$ or $\{-\}$. From these equations we see that the SU(2) transformation on the third qubit can be accounted for by a SO(3) rotation of the z-axis, defined by the unit vector:

$$\vec{x} := [\cos(\theta); \sin(\theta)\cos(\phi); \sin(\theta)\sin(\phi)] \; . \tag{A.6}$$

As noted above we have to consider only the diagonal parts of the measurement outcomes $X_\pm$, which can be represented in terms of the column vectors:

$$\vec{X}_\pm := \frac{1}{2}\, R \begin{pmatrix} 1 \\ \pm\vec{x} \end{pmatrix} \; , \tag{A.7}$$

where R is the real 4×4 matrix whose columns consist of the diagonal elements of the matrices $(\rho_1+\rho_2)$, $(\rho_1-\rho_2)$, $(\sigma+\sigma^\dagger)$, $i(\sigma-\sigma^\dagger)$.

Provided with these definitions the inequality (A.1) can be written in the form:

$$p_+|Q_{zz}(X_+/p_+)| + p_-|Q_{zz}(X_-/p_-)| \geq |Q_{zz}(X_+ + X_-)|.$$

Inserting $1 = \mathrm{tr}(\vec{X}_\pm/p_\pm)$ in the definition of Q_{zz}, this inequality can be transformed in a bilinear form in $\vec{x}$:

$$\frac{1}{p_+}\left|(1 \;\; \vec{x}^T) S \begin{pmatrix} 1 \\ \vec{x} \end{pmatrix}\right| + \frac{1}{p_-}\left|(1 \;\; -\vec{x}^T) S \begin{pmatrix} 1 \\ -\vec{x} \end{pmatrix}\right| \geq |4\alpha| \; . \tag{A.8}$$

Here α is the first element of the matrix

$$S := R^T(\sigma_y \otimes \sigma_y)R = \begin{bmatrix} \alpha & \vec{\beta}^T \\ \vec{\beta} & Q \end{bmatrix} \; , \tag{A.9}$$

and $\vec{\beta}, Q$ are defined as 3×1 and 3×3 blocks, respectively. Without loss of generality we can assume that α is positive and thus remove the absolute value sign in (A.8). Some straightforward algebra yields then the sufficient inequality:

$$\vec{x}^T\,(A+B)\,x \geq 0 \; , \tag{A.10}$$

with

$$A := \alpha\left(\vec{c} - \frac{\vec{\beta}}{\alpha}\right)\left(\vec{c} - \frac{\vec{\beta}}{\alpha}\right)^T, \quad B := Q - \frac{\vec{\beta}\vec{\beta}^T}{\alpha}, \tag{A.11}$$

where $\vec{c}$ is such that $p_\pm = (1 \pm \vec{c}^T\vec{x})/2$. We now have to show that the matrix $A + B$ has at least one positive eigenvalue. From the form of A one immediately sees that it is positive semidefinite ($\alpha > 0$). The matrix B requires more work. First we note that the matrix $\sigma_y \otimes \sigma_y$ in (A.9) has two negative and two positive eigenvalues. Assuming nonsingular R it follows from Sylvester's law of inertia [144] that S also has two positive and two negative eigenvalues[1], and so has the inverse S^{-1}. Now B is the inverse of the Schur complement of α, and hence corresponds to a principal 3×3 block of the matrix S^{-1}:

$$S^{-1} = \begin{pmatrix} * & * \\ * & B^{-1} \end{pmatrix}, \tag{A.12}$$

where the entries $*$ are of no interest here. Let us denote the eigenvalues of S^{-1} in algebraic increasing order by $\lambda_1 \dots \lambda_4$ and those of B^{-1} by $\mu_1 \dots \mu_3$. From the interlacing properties of eigenvalues of principal blocks [144], we obtain the following relation:

$$\lambda_1 \leq \mu_1 \leq \lambda_2 \leq \mu_2 \leq \lambda_3 \leq \mu_3 \leq \lambda_4. \tag{A.13}$$

Knowing that $\lambda_3 > 0$ we deduce that B^{-1} posesses at least one positive eigenvalue, and so does B. The existence of one positive eigenvalue in $A+B$ ensures that one can always find a measurement direction $\vec{x}$ such that the inequality (A.10) is fulfilled. We have proven the theorem for a mixed three qubit state. However, this result can immediately be extended to arbitrary N. To see this let us consider e.g. the correlation $|Q_{zz}(X_+/p_+)|$ for one of the measurement outcomes on the third qubit. The two qubit state X_+ can be expanded in a basis corresponding to a measurement of the fourth qubit ($X_+ = Y_+ + Y_-$). The theorem can now be applied with respect to the states $Y_\pm$ and so forth, completing the proof. ■

Note that the proof is constructive and allows to determine a measurement strategy that would at least achieve the bound reported.

Let us now show that the above result can also be generalized to a setup where the spins i and j can have any dimension, but the measurements are still performed on qubits. To be more specific we consider the operator $S_A^i \otimes S_B^j$ acting on a bipartite state ρ_{ij} of arbitrary dimension. Since local unitary transformations can always be absorbed in the definition of ρ_{ij} we can choose S_A^i and S_B^j to be diagonal. The correlation function can then be

---

[1] In the case of a singular matrix R Sylvester's law of inertia cannot directly be applied. However, it is guaranteed that in the worst case the principal block has one zero eigenvalue, which would lead to the equality with the original correlations.

written in the bilinear form:

$$\begin{aligned} Q^{ij}_{AB} &= \mathrm{tr}[\rho_{ij}\ (S^i_A \otimes S^j_B)] - \mathrm{tr}[\rho_{ij}\ (S^i_A \otimes \mathbb{1})]\mathrm{tr}[\rho_{ij}\ (\mathbb{1} \otimes S^j_B)] \\ &= \frac{1}{2}\vec{x}^T(\vec{a}\ \vec{1}^T - \vec{1}\ \vec{a}^T) \otimes (\vec{b}\ \vec{1}^T - \vec{1}\ \vec{b}^T)\vec{x}\ , \end{aligned} \tag{A.14}$$

where the column vectors $\vec{x}, \vec{a}$ and $\vec{b}$ are representing the diagonal elements of the matrices ρ_{ij}, S^i_A and S^j_B, and $\vec{1}$ is a column vector with all ones. Thus the matrix $Z := (\vec{a}\ \vec{1}^T - \vec{1}\ \vec{a}^T) \otimes (\vec{b}\ \vec{1}^T - \vec{1}\ \vec{b}^T)$ replaces the matrix $\sigma_y \otimes \sigma_y$ in the definition (A.9). Z is the tensor product of two antisymmetric matrices of rank two and therefore has two positive and two negative eigenvalues. This property is sufficient to fulfill the inequality (A.10).

A.2 Relation between correlation functions and bipartite entanglement

In this section we are interested in establishing a relation between the maximum connected correlation function and the entanglement of a pure bipartite state. In the following we will only consider bipartite qubit and qutrit states.

A.2.1 Two-qubit states

For an arbitrary two-qubit state ρ we want to maximize the correlation function:

$$Q^{ij}_{AB} = \mathrm{tr}[\rho(\ S^i_A \otimes S^j_B)] - \mathrm{tr}[\rho(\ S^i_A \otimes \mathbb{1})]\mathrm{tr}[\rho(\mathbb{1} \otimes S^j_B)]. \tag{A.15}$$

For qubits we can parametrize S_A and S_B by the three-dimensional unit vectors $\vec{a}, \vec{b}$:

$$\begin{aligned} S_A &= \vec{\sigma} \cdot \vec{a}\ , && \text{(A.16)} \\ S_B &= \vec{\sigma} \cdot \vec{b}\ , && \text{(A.17)} \end{aligned}$$

where $\vec{\sigma} = (\sigma_x\ \sigma_y\ \sigma_z)$. The correlation can then be written in the form:

$$Q_{AB} = \sum_{\alpha\beta} a_\alpha\ Q_{\alpha\beta}\ b_\beta =: \vec{a}^T\ Q\ \vec{b} \qquad (\alpha, \beta = x, y, z)\ . \tag{A.18}$$

The matrix elements $Q_{\alpha\beta}$ of the 3×3 matrix Q are defined by (A.15) with $S_A = \sigma_\alpha$, $S_B = \sigma_\beta$. Clearly the maximum value for Q_{AB} is given by the largest singular value of the matrix Q.

For a pure state $\rho = |\psi\rangle\langle\psi|$ the matrix Q can be computed using the Schmidt decomposition $|\psi\rangle = \sum_i\ \lambda_i\ |i_A\rangle \otimes |i_B\rangle$ with $\lambda_i \geq 0$. Note that local unitary transformations can always be absorbed in the definition of S_A and S_B. In this representation the matrix Q is diagonal and one can show that the maximum value is given by $Q_{xx} = 2\lambda_1\lambda_2$. It can easily be checked that this expression is equal to the concurrence C as defined in (2.4). Thus we have shown that the entanglement of a pure two-qubit state $|\psi\rangle$ as measured by the concurrence C is equal to the maximum correlation function:

$$\max_{\vec{a},\vec{b}}(Q_{AB}(|\psi\rangle)) = Q_{xx}(|\psi\rangle) = C(|\psi\rangle) = 2\lambda_1\lambda_2 \ . \tag{A.19}$$

A.2.2 Two-qutrit states

As in the qubit case we consider correlations of the form (A.15). In generalization to the usual spin-1 operators we want to maximize with respect to the bounded operators $-\mathbb{1} \leq S_A, S_B \leq \mathbb{1}$. In the forthcoming discussion we will only consider pure states. In Schmidt decomposition we have $|\psi\rangle = \sum_{i=1}^{3} \lambda_i \ |i\rangle \otimes |i\rangle$ with $\lambda_i \geq 0$ and $\lambda_1^2 + \lambda_2^2 + \lambda_3^2 = 1$. Let us begin with rewritting the correlation function:

$$\begin{aligned} Q_{AB} &= \operatorname{tr}_A(S_A \ (\rho_1 - \beta D) && \text{(A.20)} \\ &= \operatorname{tr}_B(S_B \ (\rho_2 - \alpha D) \ . && \text{(A.21)} \end{aligned}$$

Here we have defined the 3×3 matrices:

$$\begin{aligned} \rho_1 &:= \operatorname{tr}_B(\mathbb{1} \otimes S_B \ \rho) = D^{\frac{1}{2}} S_B^T D^{\frac{1}{2}} \ , && \text{(A.22)} \\ \rho_2 &:= \operatorname{tr}_A(S_A \otimes \mathbb{1} \ \rho) = D^{\frac{1}{2}} S_A D^{\frac{1}{2}} \ , && \text{(A.23)} \\ D &:= \operatorname{diag}(\lambda_1^2, \lambda_2^2, \lambda_3^2) \ , && \text{(A.24)} \end{aligned}$$

and the scalars $\alpha = \operatorname{tr}(\rho_2)$, $\beta = \operatorname{tr}(\rho_1)$. We further introduce the eigenvalue decomposition $\rho_1 - \beta D = UEU^\dagger$. Note that the diagonal matrix E has zero trace and thus has at least one negative entry. Now one immediately sees from (A.20) that Q_{AB} is maximized if S_A has the same eigenvectors as $\rho_1 - \beta D$ and if its eigenvalues are given by the sign of the matrix E. Hence we can formulate the following relations that hold for the maximum correlation function:

$$\begin{aligned} &(i) && S_A = U \ \mathrm{sign(E)} \ \mathrm{U}^\dagger \quad \text{with} \ \ \mathrm{tr(E)} = 0 && \text{(A.25)} \\ &(ii) && [S_A, \rho_1 - \beta D] = 0 && \text{(A.26)} \\ &(iii) && [S_B, \rho_2 - \alpha D] = 0 \ . && \text{(A.27)} \end{aligned}$$

These conditions lead to the simple commutator relation $[D, M] = 0$ where $M := U(|E| - \alpha \ E)U^\dagger$. Since M commutes with the diagonal matrix D it has to be diagonal. Trivially this is fulfilled for diagonal U implying also a diagonal operator S_A. A nondiagonal U is only possible if the matrix $(|E| - \alpha\, E)$ is degenerate. Since this matrix can be at most two-fold degenerate, we arrive at the interesting result that the operator S_A that maximizes the correlation Q_{AB} is either diagonal $S_A = \mathrm{diag}(1, -1, -1)$ or can be parameterized in the form:

$$S_A = \begin{pmatrix} 1 & 0 & 0 \\ 0 & \cos(\theta) & \sin(\theta)e^{-i\phi} \\ 0 & \sin(\theta)e^{i\phi} & -\cos(\theta) \end{pmatrix} . \tag{A.28}$$

As Q_{AB} is symmetric in A and B an equivalent expression with rotation angles θ' and ϕ' holds for the operator S_B. From this we can deduce the relations $\alpha = \lambda_1^2 + \cos(\theta')(\lambda_2^2 - \lambda_3^2)$ and $\beta = \lambda_1^2 + \cos(\theta)(\lambda_2^2 - \lambda_3^2)$.

The required degeneracy of the matrix $(|E| - \alpha\, E)$ puts a constraint on α (or the optimal rotation angle θ') as a function of β: $\alpha = F(\beta)$ (for simplicity we do not specify the function F here). Due to symmetry it also holds $\beta = F(\alpha)$. Clearly a fixpoint of the maximization procedure is given by the symmetric solution $\alpha = \beta$ (or $\theta = \theta'$). However, there also exists an asymmetric solution. In order to obtain nice analytical expressions for these solutions it is more convenient to parameterize the function Q_{AB} using the form (A.28) and then maximize with respect to the rotation angles θ and θ':

$$\begin{aligned} Q_{AB} &= \lambda_1^2 + \cos\theta\cos\theta'(\lambda_2^2 + \lambda_3^2) + 2\sin\theta\sin\theta'\lambda_2\lambda_3 \\ &- (\lambda_1^2 + (\lambda_2^2 - \lambda_3^2)\cos\theta)(\lambda_1^2 + (\lambda_2^2 - \lambda_3^2)\cos\theta') . \end{aligned} \tag{A.29}$$

Here we made the choice $\phi = -\phi'$, which maximizes Q_{AB}. We further note that in this expression the role of the Schmidt coefficient λ_1 is special, which results from the ordering $\lambda_1 \leq \lambda_2 \leq \lambda_3$. For the symmetric case ($\theta = \theta'$) we obtain the optimal rotation angle:

$$\cos(\theta_{opt}) = \frac{\lambda_1^2(\lambda_2^2 - \lambda_3^2)}{(\lambda_2 - \lambda_3)^2 - (\lambda_2^2 - \lambda_3^2)^2} , \tag{A.30}$$

which yields the maximum correlation function:

$$Q_{AB}^{sym} = \frac{4\lambda_2^2\lambda_3^2}{2\lambda_2\lambda_3 - \lambda_1^2} . \tag{A.31}$$

Notice that for $\lambda_1 = 0$ this reduces to the qubit solution $Q_{AB}^{max} = 2\lambda_2\lambda_3$. As for the symmetric case Q_{AB} (A.29) is quadratic in $\cos(\theta)$ the maximum can also be reached at the boundaries $\cos(\theta) = \pm 1$. This leads to diagonal operatators $S_A = S_B$ and the maximum correlation is given by:

$$Q_{AB}^{diag} = 1 - (\lambda_3^2 - (\lambda_2^2 + \lambda_1^2))^2 . \tag{A.32}$$

The asymmetric solution can also be worked out, but is difficult to cast in a nice analytical form. For our purpose it is enough to establish the following relation for the optimal rotation angles:

$$a(\cos(\theta) + \cos(\theta')) = -b(1 + \cos(\theta)\cos(\theta')), \tag{A.33}$$
$$a := \lambda_2^2 + \lambda_3^2 - (\lambda_3^2 - \lambda_2^2)^2, \tag{A.34}$$
$$b := \lambda_1^2(\lambda_3^2 - \lambda_2^2). \tag{A.35}$$

It can easily be verified that $a, b > 0$ and $a \geq b$. Inserting (A.33) in Q_{AB} (A.29) it follows that the asymmetric solution can be upper bounded by:

$$Q_{AB}^{asym} \leq \lambda_1^2 - \lambda_1^4 - \frac{b^2}{a} + 2\lambda_2\lambda_3 \ . \tag{A.36}$$

Straightforward analysis shows that the two-qubit limit ($\lambda_1 = 0$) yields an *upper* bound for the maximum correlation in the two-qutrit case:

$$Q_{AB}^{max} := \max(Q_{AB}^{sym}, Q_{AB}^{diag}, Q_{AB}^{asym}) \leq 2\lambda_2\lambda_3|_{\lambda_1=0}. \tag{A.37}$$

The maximum correlation function decreases if the number of non-zero Schmidt coefficients increases. Thus Q_{AB}^{max} cannot be used for measuring entanglement as in the qubit case. The entropy of entanglement $E(|\,\psi\rangle)$ [84], on the contrary, increases with the number of non-zero Schmidt coefficients. A fact that follows directly from the concavity property of $E(|\,\psi\rangle)$. Hence the $\lambda_1 = 0$ case $E(|\,\psi\rangle) = f(2\lambda_2\lambda_3|_{\lambda_1=0})$, with f being the convex function (2.5), yields a *lower* bound on the entropy of entanglement. From this it follows that the entanglement of a pure two-qutrit state is lower bounded by the maximum correlation function:

$$E(|\,\psi\rangle) \geq f(Q_{AB}^{max}). \tag{A.38}$$

Appendix B

Analytical calculation of the string order parameter and the LE for MPS

We consider a matrix-product state (MPS) (2.30) with qubit bonds ($D = 2$). In the case of OBC and qubits at the endpoints ($i = 0, N+1$) this (unnormalized) MPS state can be written in the form:

$$|\psi\rangle = \sum_{\alpha, i_1 \dots i_N, \beta} \vec{a}^{\alpha} A^{i_1} \dots A^{i_N} \vec{b}^{\beta} \, |\alpha\rangle |i_1 \dots i_N\rangle |\beta\rangle, \tag{B.1}$$

where $\vec{a}$ and $\vec{b}$ are two dimensional row and column vectors, respectively, and $\alpha, \beta \in \{0, 1\}$. We are interested in the string order parameter (2.48) between the endspins. Using expression (2.31) for calculating expection values of MPS, we can write:

$$Q_{SO}^{0,N+1} = \frac{\vec{E}^{a}_{\sigma_z} (E_R)^N \vec{E}^{b}_{\sigma_z}}{\vec{E}^{a}_{\mathbb{1}} (E_{\mathbb{1}})^N \vec{E}^{b}_{\mathbb{1}}}. \tag{B.2}$$

In the limit of large N and diagonalizable E_R ($E_{\mathbb{1}}$) only the maximum eigenvalue λ_R ($\lambda_{\mathbb{1}}$) will survive:

$$\xi_{SO} := \lim_{N \to \infty} Q_{SO}^{0,N+1} = \frac{(\vec{E}^{a}_{\sigma_z} \vec{r}_R)(\vec{l}_R \vec{E}^{b}_{\sigma_z})}{(\vec{E}^{a}_{\mathbb{1}} \vec{r}_{\mathbb{1}})(\vec{l}_{\mathbb{1}} \vec{E}^{b}_{\mathbb{1}})} \left(\frac{\lambda_R}{\lambda_{\mathbb{1}}} \right)^N, \tag{B.3}$$

where $\vec{l}_O$ and $\vec{r}_O$ denote the left and right eigenvectors of E_O.
In the case of the AKLT model and for the basis (2.47), we have: $A^1 = i\sigma_y$, $A^2 = \sigma_z$ and $A^3 = \sigma_x$. Hence one finds

$$\begin{aligned} E_{\mathbb{1}} &= \sigma_x \otimes \sigma_x - \sigma_y \otimes \sigma_y + \sigma_z \otimes \sigma_z, && \text{(B.4)} \\ E_R &= -\sigma_x \otimes \sigma_x + \sigma_y \otimes \sigma_y + \sigma_z \otimes \sigma_z, && \text{(B.5)} \end{aligned}$$

and $\lambda_R = \lambda_{\mathbb{1}} = 3$. Realizing that $\vec{a}^{\alpha}$ and $\vec{b}^{\beta}$ are representing unit vectors in the standard basis, we obtain the result: $\xi_{SO} = 1$.

Let us now show how to calculate the LE between the endpoints of the chain for states of the form (B.1). Since the end spins are represented by qubits we can use the concurrence (2.4) as entanglement measure, which simplifies the calculation considerably. For the basis $\mathcal{M} = \{|i\rangle\langle i|\}$ the average entanglement can be written as [74]:

$$L^{\mathcal{M},C}_{0,N+1} = \frac{\sum_{i_1 \dots i_N} 2\,|\det(A^{i_1}\dots A^{i_N})|}{\vec{E}^{a}_{\mathbb{1}}(E_{\mathbb{1}})^N \vec{E}^{b}_{\mathbb{1}}}. \tag{B.6}$$

Since the determinant factorizes, we obtain

$$L^{\mathcal{M},C}_{0,N+1} \to \frac{2}{(\vec{E}^{a}_{\mathbb{1}}\vec{r}_{\mathbb{1}})(\vec{l}_{\mathbb{1}}\vec{E}^{b}_{\mathbb{1}})}\left(\frac{\sum_i |\det(A^i)|}{\lambda_{\mathbb{1}}}\right)^N, \tag{B.7}$$

in the limit of large N. The basis which maximizes $L^{\mathcal{M},C}$ is clearly the same basis, which maximizes the expression $\sum_i |\det(A^i)|$. This problem is equivalent to calculating the EoA of the $D^2 \times D^2$ state $A^\dagger A$:

$$E_A(A) := \sup_{\mathcal{M}} \sum_i |\det(A^i)| = \mathrm{tr}|A^T(\sigma_y \otimes \sigma_y)A|. \tag{B.8}$$

The elements of the $(2S+1) \times D^2$ matrix A are given by $A_{i,(\alpha\beta)} = A^i_{\alpha,\beta}$. Hence we found a necessary and sufficient condition for long range order in the entanglement (i.e. non-vanishing $L^C_{0,N+1}$ for $N \to \infty$): The expression $E_A(A)$ has to be equal to the largest eigenvalue, $\lambda_{\mathbb{1}}$, of the matrix $E_{\mathbb{1}}$. For the AKLT model, one can easily check that this condition is indeed fulfilled, and that $L^C_{0,N+1} = 1$.

The ground state of the AKLT thus exhibits long range order both in terms of the LE and the string order parameter.

Appendix C

Fermionization of the Bose-Hubbard model

We start from the single-band Bose-Hubbard Hamiltonian (3.2) and restrict the occupation numbers at each lattice site k to $n_k \in \{0, 1, 2\}$. In this truncated basis the Hamiltonian reads:

$$\begin{aligned} H &= \sum_k [bk^2 |1\rangle_k\langle 1| + 2(bk^2 + U)|2\rangle_k\langle 2| \\ &- J\ (|0\rangle_k |1\rangle_{k+1}\langle 1|_k\langle 0|_{k+1} + \text{h.c.}) \\ &- \sqrt{2}J\ (|0\rangle_k |2\rangle_{k+1}\langle 1|_k\langle 1|_{k+1} + \text{h.c.}) \\ &- \sqrt{2}J\ (|2\rangle_k |0\rangle_{k+1}\langle 1|_k\langle 1|_{k+1} + \text{h.c.}) \\ &- 2J\ (|2\rangle_k |1\rangle_{k+1}\langle 1|_k\langle 2|_{k+1} + \text{h.c.})]. \end{aligned} \tag{C.1}$$

One can now embed the three dimensional single site Hilbert space $\mathcal{H}_B = \mathbb{C}^3$ into the composite Hilbert space $\mathcal{H}_F = \mathbb{C}^2 \otimes \mathbb{C}^2$ of two species of hard-core bosons by applying the following mapping:

$$\begin{aligned} |2\rangle = \frac{1}{\sqrt{2}}(a^\dagger)^2|\text{vac}\rangle &\rightarrow \tilde{c}^\dagger \tilde{d}^\dagger |\text{vac}\rangle, \\ |1\rangle = a^\dagger|\text{vac}\rangle &\rightarrow \tilde{c}^\dagger|\text{vac}\rangle. \end{aligned} \tag{C.2}$$

Note that singly occupied bosonic states are mapped exclusively to the $\tilde{c}$–manifold, i.e. we omit the possibility of having one particle in the the $\tilde{d}$–manifold and no particle in the $\tilde{c}$–manifold on the same site. After transforming hard-core bosons to fermions, $\tilde{c}, \tilde{d} \rightarrow c, d$, via a Jordan-Wigner transformation one obtains the following fermionic Hamiltonian:

$$\begin{aligned} H &= \sum_k [bk^2 c_k^\dagger c_k d_k d_k^\dagger + (bk^2 + U) c_k^\dagger c_k d_k^\dagger d_k \\ &- J\ (c_k^\dagger c_{k+1} d_k d_k^\dagger d_{k+1} d_{k+1}^\dagger + \text{h.c.}) \\ &- \sqrt{2} J\ (c_k^\dagger d_{k+1} d_k d_k^\dagger c_{k+1}^\dagger c_{k+1} + \text{h.c.}) \\ &- \sqrt{2} J\ (d_k^\dagger c_{k+1} c_k c_k^\dagger d_{k+1} d_{k+1}^\dagger + \text{h.c.}) \\ &- 2J\ (d_k^\dagger d_{k+1} c_k c_k^\dagger c_{k+1} c_{k+1}^\dagger + \text{h.c.})] \end{aligned} \tag{C.3}$$

This Hamiltonian can also be written in the form $H = P^\dagger \tilde{H} P$, where $\tilde{H}$ is the quadratic Hamiltonian (3.13) and P denotes the projection on the subspace, which is defined by $c_k^\dagger d_k = 0$ for all sites k. This implies that bosonic atoms in an optical lattice can effectively be described in terms of the quadratic Hamiltonian (3.13), given that the probability of finding a particle-hole pair is negligible, i.e. $\langle c_k c_k^\dagger d_k^\dagger d_k \rangle \approx 0$.

Appendix D

Numerical description of classical density matrices in terms of MPS

Our algorithmic protocols establish classical correlations between different lattice sites, when applied to thermal states in the no-tunnelling regime. Hence, a description in terms of independent wells (as in (3.6)) is no longer adequate. Therefore we refer to a representation in terms of matrix product states (MPS).

To be more precise, for a 1D lattice of length L we want to map a classical density matrix of the form

$$\rho = \sum_{\{i\}} \rho^{i_1 \ldots i_L} |i_1 \ldots i_L\rangle\langle i_1 \ldots i_L| \tag{D.1}$$

onto a pure state in MPS form:

$$|\psi\rangle = \sum_{\{i\}} A_1^{i_1} A_2^{i_2} \ldots A_L^{i_L} |i_1 \ldots i_L\rangle. \tag{D.2}$$

Here, A^{i_k} denote matrices of dimension $D \times D$ and $i_k \in \{0, \ldots, d-1\}$ is the occupation number of site k. The matrices at the endpoints, $A_1^{i_1}$ and $A_L^{i_L}$, are $1 \times D$ and $D \times 1$ vectors, respectively. The mapping from ρ to $|\psi\rangle$ can easily be accomplished by setting: $\rho^{i_1 \cdots i_L} = A_1^{i_1} A_2^{i_2} \ldots A_L^{i_L}$.

Expectation values for operators of the form $\hat{O} = \hat{O}_1 \otimes \hat{O}_2 \ldots \otimes \hat{O}_L$ are calculated according to the relation

$$\langle \hat{O} \rangle = \mathrm{tr}\ \hat{O}\rho = \prod_{k=1}^{L} \sum_{i_k=1}^{d} \langle i_k|\hat{O}_k|i_k\rangle A_k^{i_k}. \tag{D.3}$$

Local operations on ρ, like unitary operations $U_{n,m}^{n',m'}$ (3.15) or filter operations (3.16), amount to transformations of the local matrices $A_k^{i_k}$ in the MPS picture. For illustration, let us consider a completely positive map $\mathcal{C}$ which acts on a local state ρ_k at site k. In Kraus representation one can write

$$\mathcal{C}(\rho_k) = \sum_\alpha E_\alpha \rho_k E_\alpha^\dagger, \tag{D.4}$$

with the Kraus operators E_α satisfying the completeness relation $\sum_\alpha E_\alpha^\dagger E_\alpha = \mathbb{1}$. The MPS matrices transform according to

$$\tilde{A}_k^{i_k} = \sum_\alpha \sum_{j_k} |E_\alpha^{i_k,j_k}|^2 A_k^{j_k}. \tag{D.5}$$

Non-local operations that involve more than one lattice site are more complicated to implement. As an example, let us consider the most complicated case, which occurs in our protocols: a spin-dependent lattice shift S_{-1} which shifts the lattice $|b\rangle$ one site to the left. For this we have to consider two species of atoms. In generalization of (D.2), the MPS matrices $A_k^{i_k,j_k}$ are now labelled with two physical indices, i_k and j_k, referring to states $|a\rangle$ and $|b\rangle$, respectively. It will turn out to be convenient to rewrite these matrices in tensor form: $(A_k^{i_k,j_k})_{\alpha,\beta} = A_k(\alpha,\beta,i_k,j_k)$, with $\alpha,\beta = 1\ldots D$.

To begin with let us consider only the first two lattice sites. We start out with tracing over subsystem $|b\rangle$ at the first site, which yields the reduced matrix:

$$B_1(\alpha_1,\beta_1,i_1) = \sum_{j_1} A_1(\alpha_1,\beta_1,i_1,j1). \tag{D.6}$$

The reason is simply that we want to omit sites which pass the system boundaries after the lattice shift. The induced error is negligible, given that sites at the boundaries are not populated. We then multiply the matrix of the second site and perform the lattice shift: $\Theta(\alpha_1,i_1,\beta_2,i_2,j_2) = B_1(\alpha_1,\beta,i_1)A_2(\beta,\beta_2,i_2,j_2) \rightarrow \Theta(\alpha_1,i_1,j_2,\beta_2,i_2)$, where we use Einstein summation convention. After relabelling $j_2 \rightarrow j_1$ we perform a singular value decomposition:

$$\begin{aligned}&\Theta(\alpha_1,i_1,j_1,\beta_2,i_2) = \\ &U((\alpha_1,i_1,j_1),\gamma)\ \Sigma(\gamma,\gamma')\ W^\dagger(\gamma',(\beta_2,i_2)),\end{aligned} \tag{D.7}$$

with Σ being a diagonal square matrix and $\gamma,\gamma' = 1\ldots\tilde{D} \leq dD$. The new MPS matrix for site 1 can then be defined as:

$$\left(\tilde{A}_1^{i_1,j_1}\right)_{\alpha_1,\beta_1} := U(\alpha_1,i_1,j_1,\gamma)\ \Sigma^{1/2}(\gamma,\beta_1). \tag{D.8}$$

Accordingly, we define

$$B_2(\alpha_2, \beta_2, i_2) := \Sigma^{1/2}(\alpha_2, \gamma)\ W^{\dagger}(\gamma, \beta_2, i_2), \tag{D.9}$$

and iterate this scheme until the end of the lattice. Note, that the dimension D of the MPS matrices can, in principle, increase exponentially with the number of lattice shifts. If D becomes larger than a desired value D_{max} one has to resort to a truncation method similar to the one proposed for mixed quantum states [102]. However, in practice, we find that D increases only linearly with the number of lattice shifts, given that each shift is followed by a filter operation. Thus, with our method we can fairly easy simulate protocols exactly, i.e. without truncation, which involve up to 100 lattice shifts on lattices with up to $L = 500$ sites.

Appendix E

Two interacting atoms in a rotating harmonic trap

In this Appendix we study the problem of two interacting bosonic atoms in a 3D rotating harmonic trap analytically. The interaction between the atoms is approximated by a zero-range pseudo-potential. We compute the interaction energy and obtain from that the critical rotation frequency, at which the 1/2-Laughlin state becomes the ground state. Afterwards we derive a condition for the validity of the pseudo-potential approximation in tight harmonic traps.

E.1 Eigenenergies and critical rotation frequency

We consider two interacting bosonic particles of mass m in a 3D harmonic potential with trapping frequency ω. The trap is rotating in z-direction with frequency Ω. In the rotating frame the Hamiltonian reads:

$$H^{\mathrm{3D}} = -\frac{\hbar^2}{2m}\left(\nabla_1^2 + \nabla_2^2\right) + \frac{1}{2}m\omega^2\left(r_1^2 + r_2^2\right) - \Omega(L_{z,1} + L_{z,2}) + V_{\mathrm{int}}^{\mathrm{3D}}(|\mathbf{r}_1 - \mathbf{r}_2|), \tag{E.1}$$

where $L_{z,i}$ is the z-component of the angular momentum of particle $i = 1, 2$ and $V_{\mathrm{int}}^{\mathrm{3D}}$ is the interaction term. Since the interaction depends only on the relative distance of the particles, we now introduce relative and center of mass coordinates:

$$\mathbf{r} = \mathbf{r}_1 - \mathbf{r}_2, \tag{E.2}$$

$$\mathbf{R} = \frac{1}{2}\left(\mathbf{r}_1 + \mathbf{r}_2\right). \tag{E.3}$$

For the momentum operators $\mathbf{p}_i = \hbar/i\nabla_i$ this change of coordinates amounts to: $\mathbf{p} = (\mathbf{p}_1 - \mathbf{p}_2)/2$ and $\mathbf{P} = \mathbf{p}_1 + \mathbf{p}_2$. For the angular momentum operators in z-direction we deduce:

$$L_{z,1} + L_{z,2} = L_{z,\mathrm{rel}} + L_{z,\mathrm{cm}} = (\mathbf{r} \times \mathbf{p})_z + (\mathbf{R} \times \mathbf{P})_z. \tag{E.4}$$

The Hamiltonian for the relative motion can therefore be written as:

$$H_{\mathrm{rel}}^{3\mathrm{D}} = -\frac{\hbar^2}{2\mu}\,\nabla^2 + \frac{1}{2}\mu\omega^2\,r^2 - \Omega L_z + V_{\mathrm{int}}^{3\mathrm{D}}(\mathbf{r})\ , \tag{E.5}$$

where $\mu = m/2$ is the reduced mass and we have defined $L_z := L_{z,\mathrm{rel}}$ for convenience. We approximate the true interaction potential by a zero range pseudo-potential:

$$V_{\mathrm{int}}^{3\mathrm{D}}(\mathbf{r}) = g\ \delta_{reg}^{(3)}(\mathbf{r}) = \frac{2\pi\hbar^2 a_s}{\mu}\ \delta^{(3)}(\mathbf{r})\left(\frac{\partial}{\partial r} r\ .\right). \tag{E.6}$$

The coupling constant g is chosen to recover the correct long range behavior of the scattered wave for a realistic interatomic potential in the limit of low energies. The s-wave scattering length a_s can experimentally be determined, for instance, with photassociation. The regularized delta-function $\delta_{reg}^{(3)}(\mathbf{r})$ removes the $1/r$ dependence of the scattered wave and makes it regular at the origin.

For simplicity, let us first consider the case of no rotation and no interaction. The eigenstates of the 3D harmonic trap in terms of angular momentum eigenfunctions and spherical coordinates are given by [145]

$$\psi_{n'lm}^{3\mathrm{D}} \propto r^l e^{-r^2/4\ell^2} M(-n'+1, l+3/2, r^2/2\ell^2) Y_l^m(\theta,\phi), \tag{E.7}$$

where $\ell = \sqrt{\hbar/(m\omega)}$ is the harmonic oscillator length. The function $M(a,b,x)$ denotes one set of the confluent hypergeometric functions [145] and $Y_l^m(\theta,\phi)$ are the spherical harmonics. As a function of the quantum numbers $n' = 1, 2, \ldots$ and $l = 0, 1, \ldots$ the eigenenergies are:

$$E_n = (n + 3/2)\ \hbar\omega = (2(n'-1) + l + 3/2)\ \hbar\omega\ . \tag{E.8}$$

The spectrum is depicted in Fig. E.1. Each energy level is $(n+1)(n+2)/2$ fold degenerate.

Let us now consider the effect of the rotating frame. Due to the angular momentum term in (E.5) states with large and positive angular momentum become lowered in energy [Fig. E.1]. At sufficiently high rotation frequencies the lowest lying states form an almost degenerate subsystem, separated by $\hbar\omega$ from the next excited levels. The states of this subsystem read:

$$\psi_m^0(\mathbf{r}) = \varphi_m(\rho,\phi)\ \varphi_0(z), \tag{E.9}$$

where $\varphi_m(\rho,\phi)$ are the lowest Landau level (LLL) states (4.2) in the x-y plane and $\varphi_0(z)$ is the ground state of the harmonic oscillator in z-direction. This shows that in the limit of high rotation frequencies the motion in the z-direction is frozen. Hence, the LLL regime appears naturally at high rotation frequencies and a quasi-2D setup, as in Quantum Hall systems, is not required.

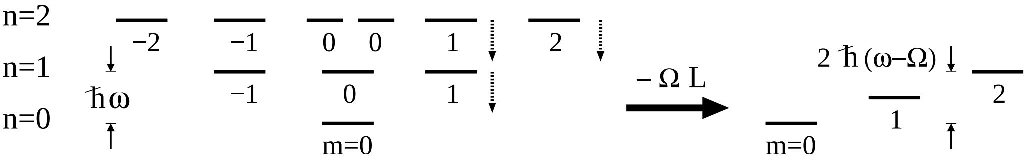

Figure E.1: Spectrum of the 3D harmonic trap in terms of angular momentum quantum numbers ($L_z = m\hbar$). The energy is given by $E_n/\hbar\omega = n+3/2$. In the rotating frame the energy of states with positive angular momentum ($m > 0$) is lowered by the amount $m\hbar\Omega$. In the limit of high rotation frequencies Ω an almost degenerate ground state subspace is formed, which is equivalent to the LLL subspace in quasi 2D systems.

We now include the interactions. For s-wave scattering (as described by the pseudo-potential (E.6)) only states with zero relative angular momentum ($l = 0$) feel the scattering potential and become modified. Since these states are unaffected by the trap rotation the situation is equivalent to the scattering problem in a 3D harmonic trap. The solution has been worked out by Busch *et al* [146] and the new eigenstates for $l = 0$ read

$$\psi_0(\mathbf{r}) \propto\ e^{-r^2/4\ell^2}\Gamma(-E/2+3/4)\ U(-E/2+3/4, 3/2, r^2/2\ell^2), \tag{E.10}$$

with U(a,b,x) denoting the other set of the confluent hypergeometric functions [145]. The energies in units of $\hbar\omega$ are defined by the equation:

$$\sqrt{2}\,\frac{\Gamma(-E/2+3/4)}{\Gamma(-E/2+1/4)} = \frac{\ell}{a_s}. \tag{E.11}$$

At positive scattering lengths ($a_s > 0$) the pseudo-potential (E.6) exhibits one bound (molecular) state. Here, we are only interested in the properties of the unbound atoms whose energies lie in the range $3/2 < E < 5/2$. Hence, the energy of the (non-molecular) ground state is effectively increased by the interaction and the interaction is therefore denoted as repulsive. The interaction energy of the new ground state ($3/2 < E < 5/2$) can be computed numerically from Eq. (E.11). The result is depicted in Fig. E.2. For weak interaction $\sqrt{2/\pi}\ a_s/\ell \ll 1$ this energy can be approximated by

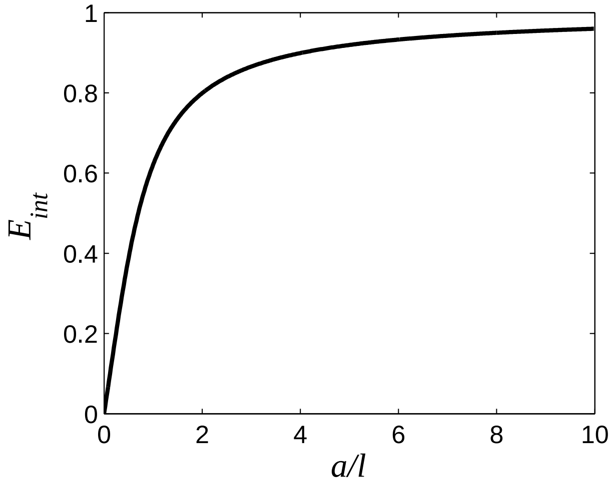

Figure E.2: Interaction energy $E_{int} = E_0/(\hbar\omega) - 3/2$ of the (non-molecular) ground state as a function of the s-wave scattering length a_s/ℓ. The interaction potential is approximated by the regularized δ-potential (E.6).

$$E_{int} = \frac{E}{\hbar\omega} - \frac{3}{2} \simeq \sqrt{\frac{2}{\pi}}\frac{a_s}{\ell} = \eta. \tag{E.12}$$

Here we have introduced the dimensionless parameter η that determines the interaction energy of two particles in a 3D trap. In this limit of weak interaction we could have calculated the interaction energy also directly using perturbation theory. For $a_s \ll \ell$ the scattered wave reaches its asymptotic form before it feels the influence of the trapping potential. Hence, the scattering problem is equivalent to s-wave scattering in free space. In first order perturbation theory the change of the ground state energy is given by the expression $E_{int} = g \int d\mathbf{r}\ |\psi_0^0(\mathbf{r})|^2\ \delta^{(3)}(\mathbf{r})$, where $\psi_0^0(\mathbf{r})$ is the Gaussian ground state of a 3D harmonic trap (see Eq. (E.9) with $m = 0$). Evaluation of the integral yields the result (E.12).

As a consequence of the repulsive s-wave scattering, the $m = 0$ ground state in Fig. E.1 becomes shifted upwards in energy, whereas all the other states of the LLL remain unchanged. Thus for a certain critical rotation frequency Ω_c the $m = 2$ state ψ_2^0 (E.9) becomes energetically favorable (for bosons the $m = 1$ state is forbidden due to symmetry). The 2D component of this state is equivalent to the 1/2-Laughlin state of 2 particles (4.5). In the weak interaction limit (E.12) the critical rotation frequency is given by:

$$\frac{\Omega_c}{\omega} = 1 - \frac{\eta}{2}. \tag{E.13}$$

In current experiments [24] with ^{87}Rb atoms we have $\eta = 0.062$ and hence we are well in the regime of validity of Eq. (E.13). The critical rotation frequency to obtain the 1/2-Laughlin state as the ground state is then $\Omega_c = 0.97\ \omega$.

E.2 Validity of the pseudo-potential approximation

We now address the problem of the validity of the pseudo-potential approximation (E.6). The key idea of the pseudo-potential is to replace the exact inter-atomic scattering potential by a model potential, which meets the following conditions: (i) in the limit of low energies (s-wave scattering) it has the same scattering amplitude as the true potential. (ii) it should be treatable in the Born approximation. For scattering in 3D the simplest model potential satisfying these requirements is the zero range pseudo-potential (E.6) initially introduced by Enrico Fermi [147, 148]. The only free parameter is the coupling constant g which is fixed by solving the scattering problem in free space and by identifying the s-wave scattering amplitude of the pseudo-potential with the one for the true scattering potential. So far it is not completely clear under which conditions this approach also accounts for scattering in systems with tight harmonic confinement. Recently there has been a controversy [149, 150] whether the s-wave scattering length a_s or the range of the potential (e.g. given by the characteristic length of the van der Waals tail $\beta_6 = (2\mu C_6/\hbar^2)^{1/4}$) sets the relevant length scale that has to be compared to the harmonic oscillator length ℓ.

In order to possibly resolve this controversy we address the problem of two interacting particles in a 3D harmonic trap analytically. To this end we replace the true inter-atomic scattering potential by a central well potential of radius b:

$$V_{int}(r) = -V_0\ \Theta(b - r). \tag{E.14}$$

In the following we will first review the scattering problem in free space and determine necessary validity conditions for the substitution of the well potential (E.14) by the pseudo-potential (E.6). In a second step, we generalize our approach to systems with harmonic confinement.

We consider two un-trapped particles interacting via the potential (E.14). Using spherical coordinates and the ansatz $\psi_{l,m}(\mathbf{r}) = u_l(r)/r\, Y_l^m(\theta,\phi)$ for the wavefunction, we arrive at the following Schrödinger equation for the relative motion of the two particles:

$$\partial_r^2 u_l - \frac{l(l+1)}{r^2} + \frac{2\mu}{\hbar^2}\left[E - V_{int}(r)\right] u_l = 0 \tag{E.15}$$

Considering only s-wave scattering ($l = 0$) this simplifies to:

$$\begin{aligned} u_{\mathrm{I}}^{''} + k_1^2 u_{\mathrm{I}} &= 0 \quad \text{for} \quad \mathrm{r} \leq \mathrm{b}, & \text{(E.16)} \\ u_{\mathrm{II}}^{''} + k^2 u_{\mathrm{II}} &= 0 \quad \text{for} \quad r \geq b, & \text{(E.17)} \end{aligned}$$

with $k^2 = 2\mu E/\hbar^2$, $\kappa^2 = 2\mu V_0/\hbar^2$ and $k_1^2 = k^2 + \kappa^2$. The solution of these equations can be written in the form $u_{\mathrm{I}} \propto \sin(k_1 r)$ and $u_{\mathrm{II}} \propto \sin(kr + \delta_0(k))$. The scattering phase $\delta_0(k)$ is determined by the boundary condition at $r = b$:

$$\left.\frac{u_{\mathrm{I}}}{u_{\mathrm{I}}'}\right|_{r=b} = \left.\frac{u_{\mathrm{II}}}{u_{\mathrm{II}}'}\right|_{r=b} \quad \Longleftrightarrow \quad k_1 \cot(k_1 b) = k \cot(kb + \delta_0(k)). \tag{E.18}$$

Solving for $\delta_0(k)$ we find:

$$k \cot \delta_0(k) = \frac{k^2 + k\ k_1 \cot(k_1 b)\ \cot(kb)}{k \cot(kb) - k_1 \cot(k_1 b)}. \tag{E.19}$$

The scattering phase can be associated with an energy-dependent scattering length via the relation:

$$a_s(k) = \tan \delta_0(k)/k. \tag{E.20}$$

Under the assumption of a deep well ($E \ll V_0$) one can now express Eq. (E.19) in terms of the so-called effective range approximation:

$$\frac{1}{a_s(k)} = \frac{1}{a_s} - \frac{1}{2} k^2 r_{eff} + \mathcal{O}\left((k/\kappa)^4\right). \tag{E.21}$$

Here we have used the definition for the energy-independent scattering length $a_s = b - \tan(\kappa b)/\kappa$. The parameter r_{eff} is called the effective range of the scattering potential:

$$r_{eff} = b\left(1 - \frac{b}{(\kappa b)^2 a_s} - \frac{b^2}{3a_s^2}\right). \tag{E.22}$$

If the scattering potential supports many bound states ($b\kappa \gg 1$) and if $a_s \gg b$ then $r_{eff} \approx b$, i.e. the effective range of the potential is approximately equal to the radius of the potential well.

Let us now compare these results with the scattering properties of the zero-range pseudo-potential (E.6). In this case the scattering phase is given by the relation:

$$k \cot \delta_0^{\mathrm{ps}}(k) = -\frac{1}{a_s}. \tag{E.23}$$

Comparing this with Eqs. (E.19) and (E.21) we find that the pseudo-potential yields the same scattering phase as the well potential given that the following condition is fulfilled:

$$(ka_s)(kr_{eff}) \ll 1. \tag{E.24}$$

Rather than comparing scattering phases it might be more important to compare scattering amplitudes. In general, the s-wave scattering amplitude f_0 can be deduced from the scattering phase via the following relation:

$$f_0(k) = \frac{\tan \delta_0(k)}{k} \frac{1}{1 - i \tan \delta_0(k)}. \tag{E.25}$$

In the case of a central well potential we can insert Eqs. (E.19) and (E.21) for $\delta_0(k)$ to obtain the scattering amplitude in the effective range approximation[1]:

$$f_0(k) = \frac{-a_s}{1 + ika_s - \frac{1}{2}\, k^2 a_s r_{eff}}. \tag{E.26}$$

For the pseudo-potential one finds the expression:

$$f_0^{\mathrm{ps}}(k) = \frac{-a_s}{1 + ika_s}. \tag{E.27}$$

Comparison of Eqs. (E.26) and (E.27) yields the condition

$$k\ r_{eff} \ll 1 \tag{E.28}$$

for the validity of the pseudo-potential. This condition is less stringent than (E.24), which was obtained by comparing scattering phases. In particular, it shows that the pseudo-potential can reproduce the scattering amplitude of the true potential even in the case of a diverging scattering length $a_s \to \infty$.

---

[1] This result holds not only for a central well, but generally for isotropic scattering potentials vanishing for long distances as $1/r^n$ with $n > 5$ [151].

This discussion of the scattering problem in free space will become very useful when we now turn to our true problem: the validity of the pseudo-potential approximation in the presence of a tight harmonic trap. This problem is conceptually different from the previous one, because we will now have to compare eigenenergies rather than scattering amplitudes in order to validate the substitution of the well potential by the pseudo-potential. As before we will only consider states with zero relative angular momentum. Moreover we will restrict the discussion to experimentally relevant setups, where the range of the scattering potential is much shorter than the trap size. In the special case of the well potential this implies $b \ll \ell$ with $\ell = \sqrt{\hbar/(m\omega)}$ being the characteristic length of the harmonic trap[2]. Under this assumption the influence of the trapping potential within the central well ($r \leq b$) is negligible and the relative motion is governed by the same Schrödinger equation as in free space (E.16). This allows us to express the boundary condition for the inner solution u_{I} in terms of the scattering length $a_s(k)$:

$$\frac{1}{\ell}\frac{u_{\mathrm{I}}}{u_I'}\bigg|_{r=b} = \frac{\tan(k_1 b)}{\ell k_1} \approx \frac{-\frac{a_s(k)}{\ell}+\frac{b}{\ell}}{1+b\ a_s(k)\ k^2}. \tag{E.29}$$

Here we have used Eqs. (E.19), (E.20) and the approximation $kb \ll 1$.

Outside the well ($r > b$) the radial part of the Schrödinger equation takes the usual harmonic oscillator form:

$$u_{\mathrm{II}}'' + \left(k^2 - \frac{r^2}{4\ell^4}\right) u_{\mathrm{II}} = 0. \tag{E.30}$$

The solution of this equation can expressed in terms of normalizable confluent hypergeometric functions [145]: $u_{\mathrm{II}}(r) \propto rU(-\nu, 3/2, r^2/2\ell^2)\ e^{-r^2/4\ell^2}$ with $\nu = E/(2\hbar\omega) - 3/4$. Since $b \ll \ell$ we can simplify this solution at the boundary $r = b$ by Taylor expanding $U(-\nu, 3/2, x)$ around $x = 0$:

$$\frac{-xU(-\nu,3/2,x)}{\sqrt{\pi}} = -\frac{1}{\Gamma(-\nu)} + \frac{2}{\Gamma(-\nu-1/2)}\,x + \frac{1+2\nu}{\Gamma(-\nu)}\,x^2 + \mathcal{O}(x^3). \tag{E.31}$$

This yields the following boundary condition for the outer solution:

$$\frac{1}{\ell}\ \frac{u_{\mathrm{II}}}{u_{\mathrm{II}}'}\bigg|_{r=b} = \frac{-\frac{\Gamma(-\nu-1/2)}{\sqrt{2}\ \Gamma(-\nu)}+\frac{b}{\ell}}{1+\frac{\Gamma(-\nu-1/2)}{\sqrt{2}\ \Gamma(-\nu)}\ k^2\ b\ \ell}. \tag{E.32}$$

---

[2] For ^{87}Rb we have $\beta_6 \simeq 8$ nm [150] and the typical on-site trap width in a deep optical lattice is given by $\ell \simeq 64$ nm [24].

Setting Eqs. (E.32) and (E.29) equal to each other we can cast the quantization rule for the eigenenergies in a rather simple form:

$$\frac{\Gamma(-\nu - 1/2)}{\sqrt{2}\,\Gamma(-\nu)} \simeq \frac{\ell}{a_s(k)}. \tag{E.33}$$

This result can now very easily be compared to the quantization rule (E.10) obtained from the pseudo-potential calculation. Using the effective range approximation of $a_s(k)$ (E.21) one finds that the pseudo-potential yields the correct eigenenergies if the following condition is fulfilled:

$$(ka_s)(kr_{eff}) \ll 1 \tag{E.34}$$

Note that this coincides with the validity condition (E.24) in free space, when demanding that the pseudo-potential produces also the correct scattering phase. Note that so far we have only made the assumptions $kb \ll 1$, $b \ll \ell$ and $k^2 \ll \kappa^2$. For ground state energies $k \approx 1/\ell$ and in the limit $r_{eff} \approx b$ the condition (E.34) can be further simplified to: $a_s b \ll \ell^2$. This shows that the pseudo-potential can also be applied in the limit of a_s being much larger than the trap size ℓ, given that the range of the scattering potential b is small enough.

We believe that our result (E.34), which has been derived for a central well potential, also holds for quite general shapes of both the trapping or scattering potential, given that the following two requirements are fulfilled: (i) the range of the scattering potential (e.g. given by β_6) is much smaller than the characteristic size of the trap. (ii) the scattering potential vanishes for large distances as $1/r^n$ with $n > 5$ so that the effective range approximation (E.21) applies.

Then the energy quantization rule depends only linearly on the energy dependent scattering length $a_s(k)$ as demonstrated in Eq. E.33. Checking the validity of the pseudo-potential then reduces to comparing $a_s(k)$ with a_s. Exploiting the effective range approximation (E.21) leads to the validity condition (E.34), with a_s and r_{eff} containing the information about the exact scattering potential and the quantized momenta k containing the information about the trapping potential. This argumentation also implies that the range of validity of the pseudo-potential can be greatly enhanced by replacing $a_s \rightarrow a_s(k)$ in the definition of the coupling-constant g (E.6).

Our findings are confirmed by numerical studies of the eigenenergies of different pairs of alkali atoms in a harmonic trap interacting through a realistic $a^3 \sum_u^+$ potential [150, 152]. In [152] it has been shown for ^{23}Na atoms that the eigenvalues are very well approximated by the relation (E.33), even for energies at which $a_s(k)$ is diverging. The authors of [150] studied the regime of large scattering lengths a_s. Using $a_s(k)$ in the definition of the pseudo-potential the correct eigenenergies could be reproduced up to a regime where $\beta_6 \sim \ell$. They also compared their numerical calculation of the ground state energy for the realistic potential with the result (E.11) for the energy-independent pseudo-potential. Their findings for the validity of the pseudo-potential approximation are consistent with condition (E.34).

Bibliography

[1] C. H. Bennett, G. Brassard, C. Crépeau, R. Jozsa, A. Peres, and W. K. Wootters, Phys. Rev. Lett. **70**, 1895 (1993).

[2] A. K. Ekert, Phys. Rev. Lett. **67**, 661 (1991).

[3] M. A. Nielson and I. L. Chuang, *Quantum Computation and Quantum Information* (Cambridge University Press, Cambridge, 2000).

[4] H. Häffner, W. Hänsel, C. F. Roos, J. Benhelm, D. Chek-al-kar, M. Chwalla, T. Körber, U. D. Rapol, M. Riebe, P. O. Schmidt, C. Becher, O. Gühne, W. Dür, and R. Blatt, Nature **438**, 643 (2005).

[5] D. Leibfried, E. Knill, S. Seidelin, J. Britton, R. B. Blakestad, J. Chiaverini, D. B. Hume, W. M. Itano, J. D. Jost, C. Langer, R. Ozeri, R. Reichle, and D. J. Wineland, Nature **438**, 639 (2005).

[6] Z. Zhao, Y.-A. Chen, A.-N. Zhang, T. Yang, H. J. Briegel, and J.-W. Pan, Nature **430**, 54 (2004).

[7] H. J. Briegel and R. Raussendorf, Phys. Rev. Lett. **86**, 910 (2001).

[8] R. Raussendorf and H. J. Briegel, Phys. Rev. Lett. **86**, 5188 (2001).

[9] E. Jané, G. Vidal, W. Dür, P. Zoller, and J. I. Cirac, Quant. Inf. Comp. **3**, 15 (2003).

[10] A. Y. Kitaev, arXiv:quant-ph/9707021.

[11] C. H. Bennett, D. P. DiVincenzo, J. A. Smolin, and W. K. Wooters, Phys. Rev. A **54**, 3824 (1996).

[12] C. H. Bennett, G. Brassard, S. Popescu, B. Schumacher, J. A. Smolin, and W. K. Wooters, Phys. Rev. Lett. **76**, 722 (1996).

[13] A. Osterloh, L. Amico, G. Falci, and R. Fazio, Nature **416**, 608 (2002).

[14] T. J. Osborne and M. A. Nielsen, Phys. Rev. A **66**, 032110 (2002).

[15] G. Vidal, J. I. Latorre, E. Rico, and A. Kitaev, Phys. Rev. Lett. **90**, 227902 (2003).

[16] J. L. Latorre, E. Rico, and G. Vidal, Quant. Inf. Comp. **4 (1)**, 48 (2004).

[17] H.-J. Briegel, W. Dür, J. I. Cirac, and P. Zoller, Phys. Rev. Lett. **81**, 5932 (1998).

[18] S. Sachdev, *Quantum Phase Transitions* (Cambridge University Press, Cambridge, 1999).

[19] C. A. Regal, M. Greiner, and D. S. Jin, Phys. Rev. Lett. **92**, 040403 (2004).

[20] M. W. Zwierlein, C. A. Stan, C. H. Schunck, S. M. F. Raupach, A. J. Kerman, and W. Ketterle, Phys. Rev. Lett. **92**, 120403 (2004).

[21] M. Bartenstein, A. Altmeyer, S. Riedl, S. Jochim, C. Chin, J. H. Denschlag, and R. Grimm, Phys. Rev. Lett. **92**, 120401 (2004).

[22] T. Bourdel, L. Khaykovich, J. Cubizolles, J. Zhang, F. Chevy, M. Teichmann, L. Tarruell, S. J. J. M. F. Kokkelmans, and C. Salomon, Phys. Rev. Lett. **93**, 050401 (2004).

[23] J. Kinast, S. L. Hemmer, M. E. Gehm, A. Turlapov, and J. E. Thomas, Phys. Rev. Lett. **92**, 150402 (2004).

[24] M. Greiner, O. Mandel, T. Esslinger, T. W. Hänsch, and I. Bloch, Nature **415**, 39 (2002).

[25] B. Paredes, A. Widera, V. Murg, O. Mandel, S. Fölling, I. Cirac, G. V. Shlyapnikov, T. W. Hänsch, and I. Bloch, Nature **429**, 277 (2004).

[26] H. Moritz, T. Stöferle, M. Köhl, and T. Esslinger, Phys. Rev. Lett. **91**, 250402 (2003).

[27] T. Stöferle, H. Moritz, C. Schori, M. Köhl, and T. Esslinger, Phys. Rev. Lett. **92**, 130403 (2004).

[28] M. Köhl, H. Moritz, T. Stöferle, K. Günter, and T. Esslinger, Phys. Rev. Lett. **94**, 080403 (2005).

[29] B. Laburthe Tolra, K. M. O'Hara, J. H. Huckans, W. D. Phillips, S. L. Rolston, and J. V. Porto, Phys. Rev. Lett. **92**, 190401 (2004).

[30] K. Xu, Y. Liu, J. R. Abo-Shaeer, T. Mukaiyama, J. K. Chin, D. E. Miller, W. Ketterle, K. M. Jones, and E. Tiesinga, Phys. Rev. A **72**, 043604 (2005).

[31] C. Ryu, X. Du, E. Yesilada, A. M. Dudarev, S. Wan, Q. Niu, and D. Heinzen, arXiv:cond-mat/0508201.

[32] G. Thalhammer, K. Winkler, F. Lang, S. Schmid, R. Grimm, and J. H. Denschlag, Phys. Rev. Lett. **96**, 050402 (2006).

[33] J. I. Cirac and P. Zoller, Science **301**, 176 (2003).

[34] J. I. Cirac and P. Zoller, Phys. Today **57**, 38 (2004).

[35] W. Hofstetter, J. I. Cirac, P. Zoller, E. Demler, and M. Lukin, Phys. Rev. Lett. **89**, 220407 (2002).

[36] J. J. Garcia-Ripoll and J. I. Cirac, New J. Phys. **5**, 76 (2003).

[37] L.-M. Duan, E. Demler, and M. D. Lukin, Phys. Rev. Lett. **91**, 090402 (2003).

[38] J. J. Garcia-Ripoll, M. A. Martin-Delgado, and J. I. Cirac, Phys. Rev. Lett. **93**, 250405 (2004).

[39] L. Santos, M. A. Baranov, J. I. Cirac, H.-U. Everts, H. Fehrmann, and M. Lewenstein, Phys. Rev. Lett. **93**, 030601 (2004).

[40] H. P. Büchler, M. Hermele, S. D. Huber, M. P. A. Fisher, and P. Zoller, Phys. Rev. Lett. **95**, 040402 (2005).

[41] A. Micheli, G. K. Brennen, and P. Zoller, arXiv:quant-ph/0512222.

[42] R. Barnett, D. Petrov, M. Lukin, and E. Demler, arXiv:cond-mat/0601302.

[43] A. Reischl, K. P. Schmidt, and G. S. Uhrig, Phys. Rev. A **72**, 063609 (2005).

[44] K. G. H. Vollbrecht, E. Solano, and J. I. Cirac, Phys. Rev. Lett. **93**, 220502 (2004).

[45] P. Rabl, A. J. Daley, P. O. Fedichev, J. I. Cirac, and P. Zoller, Phys. Rev. Lett. **91**, 110403 (2003).

[46] D. Jaksch, H.-J. Briegel, J. I. Cirac, C. W. Gardiner, and P. Zoller, Phys. Rev. Lett. **82**, 1975 (1999).

[47] O. Mandel, M. Greiner, A. Widera, T. Rom, T. W. Hänsch, and I. Bloch, Nature **425**, 937 (2003).

[48] T. Chakraborty and P. Pietiläinen, *The Quantum Hall Effects: Fractional and Integral* (Springer, Berlin, 1995).

[49] R. B. Laughlin, Phys. Rev. Lett. **50**, 1395 (1983).

[50] N. K. Wilkin and J. M. F. Gunn, Phys. Rev. Lett. **84**, 6 (2000).

[51] N. K. Wilkin and J. M. F. Gunn, Phys. Rev. Lett. **87**, 120405 (2001).

[52] J. Sinova, C. B. Hanna, and A. H. MacDonald, Phys. Rev. Lett. **89**, 030403 (2002).

[53] T.-L. Ho and E. Mueller, Phys. Rev. Lett. **89**, 050401 (2002).

[54] N. Regnault and T. Jolicoeur, Phys. Rev. Lett. **91**, 030402 (2003).

[55] T. Ghosh and G. Baskaran, Phys. Rev. A **69**, 023603 (2004).

[56] M. A. Baranov, K. Osterloh, and M. Lewenstein, Phys. Rev. Lett. **94**, 070404 (2005).

[57] B. Paredes, P. Fedichev, J. I. Cirac, and P. Zoller, Phys. Rev. Lett. **87**, 010402 (2001).

[58] B. Paredes, P. Zoller, and J. I. Cirac, Phys. Rev. A **66**, 033609 (2002).

[59] F. Verstraete, M. Popp, and J. I. Cirac, Phys. Rev. Lett. **92**, 027901 (2004).

[60] M. Popp, B. Paredes, and J. I. Cirac, Phys. Rev. A **70**, 053612 (2004).

[61] M. Popp, F. Verstraete, M. A. Martin-Delgado, and J. I. Cirac, Phys. Rev. A **71**, 042306 (2005).

[62] M. Popp, F. Verstraete, M. A. Martin-Delgado, and J. I. Cirac, Applied Physics B **82**, 225 (2006).

[63] M. Popp, F. Verstraete, M. A. Martin-Delgado, and J. I. Cirac, in *Quantum Information Processing: From Theory to Experiment*, Vol. 199 of *NATO Science Series: Computer and Systems Sciences*, edited by D. Angelakis, M. Christandl, A. Ekert, A. Kay, and S. Kulik (IOS Press, Amsterdam, 2006), pp. 191–217.

[64] M. Popp, J. J. Garcia-Ripoll, K. G. H. Vollbrecht, and J. I. Cirac, Phys. Rev. A **74**, 013622 (2006).

[65] M. Popp, K. G. H. Vollbrecht, and J. I. Cirac, Fortschr. Phys. **54**, 686 (2006).

[66] M. Popp, J. J. Garcia-Ripoll, K. G. H. Vollbrecht, and J. I. Cirac, New J. Phys. **8**, 164 (2006).

[67] J. Preskill, J. Mod. Opt. **47**, 127 (2000).

[68] P. Zanardi and X. Wang, J. Phys. A **35**, 7947 (2002).

[69] D. Gunlycke, V. M. Kendon, V. Vedral, and S. Bose, Phys. Rev. A **64**, 042302 (2001).

[70] R. Somma, G. Ortiz, H. Barnum, E. Knill, and L. Viola, Phys. Rev. A **70**, 042311 (2004).

[71] T. Roscilde, P. Verrucchi, A. Fubini, S. Haas, and V. Tognetti, Phys. Rev. Lett. **93**, 167203 (2004).

[72] W. Dür, H.-J. Briegel, J. I. Cirac, and P. Zoller, Phys. Rev. A **59**, 169 (1999).

[73] D. M. Greenberger, M. Horne, and A. Zeilinger, in *Bell's Theorem, Quantum Theory, and Conceptions of the Universe*, edited by M. Kafatos (Kluwer, Dordrecht, 1989).

[74] F. Verstraete, M. A. Martin-Delgado, and J. I. Cirac, Phys. Rev. Lett. **92**, 087201 (2004).

[75] M. Fannes, B. Nachtergaele, and R. Werner, Comm. Math. Phys. **144**, 443 (1992).

[76] S. Ostlund and S. Rommer, Phys. Rev. Lett. **75**, 3537 (1995).

[77] N. Metropolis, A. W. Rosensbluth, M. N. Rosensbluth, A. H. Teller, and E. Teller, J. Chem. Phys. **21**, 1087 (1953).

[78] I. Affleck, T. Kennedy, E. H. Lieb, and H. Tasaki, Comm. Math. Phys. **115**, 477 (1988).

[79] B.-Q. Jin and V. E. Korepin, Phys. Rev. A **69**, 062314 (2004).

[80] J. K. Pachos and M. B. Plenio, Phys. Rev. Lett. **93**, 056402 (2004).

[81] O. F. Syljuasen, Phys. Lett. A **322**, 25 (2004).

[82] W. Dür, L. Hartmann, M. Hein, M. Lewenstein, and H.-J. Briegel, Phys. Rev. Lett. **94**, 097203 (2005).

[83] R. Raussendorf, S. Bravyi, and J. Harrington, Phys. Rev. A **71**, 062313 (2005).

[84] C. H. Bennett, H. J. Bernstein, S. Popescu, and B. Schumacher, Phys. Rev. A. **53**, 2046 (1996).

[85] W. K. Wootters, Phys. Rev. Lett. **80**, 2245 (1998).

[86] G. Vidal and R. F. Werner, Phys. Rev. A **65**, 032314 (2002).

[87] M. Horodecki, P. Horodecki, and R. Horodecki, Phys. Lett. A **223**, 1 (1996).

[88] A. Peres, Phys. Rev. Lett. **77**, 1413 (1996).

[89] M. Horodecki, P. Horodecki, and R. Horodecki, Phys. Rev. Lett. **80**, 5239 (1998).

[90] P. Horodecki, M. Horodecki, and R. Horodecki, Phys. Rev. Lett. **82**, 1056 (1999).

[91] T. Laustsen, F. Verstraete, and S. J. van Enk, Quant. Inf. Comp. **3**, 64 (2003).

[92] D. Aharonov, Phys. Rev. A **62**, 062311 (2000).

[93] J. I. Cirac, P. Zoller, H. J. Kimble, and H. Mabuchi, Phys. Rev. Lett. **78**, 3221 (1997).

[94] S. J. van Enk, J. I. Cirac, and P. Zoller, Science **279**, 205 (1998).

[95] B. Kraus and J. I. Cirac, Phys. Rev. Lett. **92**, 013602 (2004).

[96] D. P. DiVincenzo, C. A. Fuchs, H. Mabuchi, J. A. Smolin, A. Thapliyal, and A. Uhlmann, arXiv:quant-ph/9803033.

[97] J. Dukelsky, M. A. Martin-Delgado, T. Nishino, and G. Sierra, Europhys. Lett. **43**, 457 (1997).

[98] S. R. White, Phys. Rev. Lett. **69**, 2863 (1992).

[99] L. C. Venuti and M. Roncaglia, Phys. Rev. Lett. **94**, 207207 (2005).

[100] F. Verstraete, D. Porras, and J. I. Cirac, Phys. Rev. Lett. **93**, 227205 (2004).

[101] G. Vidal, Phys. Rev. Lett. **93**, 040502 (2004).

[102] F. Verstraete, J. J. Garcia-Ripoll, and J. I. Cirac, Phys. Rev. Lett. **93**, 207204 (2004).

[103] D. Porras, F. Verstraete, and J. I. Cirac, Phys. Rev. B **73**, 014410 (2006).

[104] M. Zwolak and G. Vidal, Phys. Rev. Lett. **93**, 207205 (2004).

[105] G. Vidal, Phys. Rev. Lett. **91**, 147902 (2003).

[106] P. Pfeuty, Ann. Phys. **57**, 79 (1970).

[107] V. Murg and J. I. Cirac, Phys. Rev. A **69**, 042320 (2004).

[108] U. Wolff, Phys. Rev. Lett. **62**, 361 (1989).

[109] M. Takahashi, *Thermodynamics of One-Dimensional Solvable Models* (Cambridge University Press, Cambridge, 1999).

[110] H. A. Bethe, Z. Physik **71**, 205 (1931).

[111] C. N. Yang and C. P. Yang, Phys. Rev. **150**, 321 (1966).

[112] S.-J. Gu, H.-Q. Lin, and Y.-Q. Li, Phys. Rev. A **68**, 042330 (2003).

[113] O. F. Syljusen, Phys. Rev. A **68**, 060301 (2003).

[114] F. D. M. Haldane, Phys. Lett. **93A**, 464 (1983).

[115] M. den Nijs and K. Rommelse, Phys. Rev. B **40**, 4709 (1989).

[116] T. Kennedy, J. Phys. Condens. Matter **2**, 5737 (1990).

[117] N. D. Mermin and H. Wagner, Phys. Rev. Lett. **17**, 1133 (1966).

[118] J. Mompart, K. Eckert, W. Ertmer, G. Birkl, and M. Lewenstein, Phys. Rev. Lett. **90**, 147901 (2003).

[119] G. K. Brennen, I. H. Deutsch, and C. J. Williams, Phys. Rev. A **65**, 022313 (2002).

[120] H. G. Katzgraber, A. Esposito, and M. Troyer, arXiv:cond-mat/0510194.

[121] M. Köhl, arXiv:cond-mat/0510567.

[122] T. Stöferle, H. Moritz, K. Günter, M. Köhl, and T. Esslinger, Phys. Rev. Lett. **96**, 030401 (2006).

[123] T. Gericke, F. Gerbier, A. Widera, S. Fölling, O. Mandel, and I. Bloch, arXiv:cond-mat/0603590.

[124] A. J. Daley, P. O. Fedichev, and P. Zoller, Phys. Rev. A **69**, 022306 (2004).

[125] F. Gerbier, A. Widera, S. Fölling, O. Mandel, T. Gericke, and I. Bloch, arXiv:cond-mat/0601151.

[126] D. Jaksch, C. Bruder, J. I. Cirac, C. W. Gardiner, and P. Zoller, Phys. Rev. Lett. **81**, 3108 (1998).

[127] L. Viverit, C. Menotti, T. Calarco, and A. Smerzi, Phys. Rev. Lett. **93**, 110401 (2004).

[128] V. Murg, private communication.

[129] A. Widera, O. Mandel, M. Greiner, S. Kreim, T. W. Hänsch, and I. Bloch, Phys. Rev. Lett. **92**, 160406 (2004).

[130] G. K. Brennen, C. M. Caves, P. S. Jessen, and I. H. Deutsch, Phys. Rev. Lett. **82**, 1060 (1999).

[131] S. Peil, J. V. Porto, B. Laburthe Tolra, J. M. Obrecht, B. E. King, M. Subbotin, S. L. Rolston, and W. D. Phillips, Phys. Rev. A **67**, 051603 (2003).

[132] A. Polkovnikov, E. Altman, E. Demler, B. Halperin, and M. D. Lukin, Phys. Rev. A **71**, 063613 (2005).

[133] P. Billingsley, *Probability and Measure* (Wiley, New York, 1995).

[134] D. Schrader, I. Dotsenko, M. Khudaverdyan, Y. Miroshnychenko, A. Rauschenbeutel, and D. Meschede, Phys. Rev. Lett. **93**, 150501 (2004).

[135] T. Calarco, E. A. Hinds, D. Jaksch, J. Schmiedmayer, J. I. Cirac, and P. Zoller, Phys. Rev. A **61**, 022304 (2000).

[136] J. Sebby-Strabley, M. Anderlini, P. S. Jessen, and J. V. Porto, arXiv:cond-mat/0602103.

[137] A. H. MacDonald, arXiv: cond-mat/9410047.

[138] M. Greiner and I. Bloch, private communication.

[139] G. Moore and N. Read, Nucl. Phys. B **360**, 362 (1991).

[140] V. Schweikhard, I. Coddington, P. Engels, V. P. Mogendorff, and E. A. Cornell, Phys. Rev. Lett. **92**, 040404 (2004).

[141] V. Bretin, S. Stock, Y. Seurin, and J. Dalibard, Phys. Rev. Lett. **92**, 050403 (2004).

[142] N. Read and N. R. Cooper, Phys. Rev. A **68**, 035601 (2003).

[143] J. Stenger, S. Inouye, M. R. Andrews, H.-J. Miesner, D. M. Stamper-Kurn, and W. Ketterle, Phys. Rev. Lett. **82**, 2422 (1999).

[144] R. A. Horn and C. R. Johnson, *Matrix Analysis* (Cambridge University Press, Cambridge, 1985).

[145] A. Galindo and P. Pascual, *Quantum Mechanics I* (Springer, Berlin Heidelberg, 1990).

[146] T. Busch, B. Englert, K. Rzazewski, and M. Wilkens, Found. of Phys. **28**, 549 (1998).

[147] E. Fermi, Ricerca Sci. **7**, 13 (1936).

[148] K. Huang, *Statistical Mechanics* (John Wiley & Sons, New York, 1963).

[149] E. Tiesinga, C. J. Williams, F. H. Mies, and P. S. Julienne, Phys. Rev. A **61**, 063416 (2000).

[150] D. Blume and C. H. Greene, Phys. Rev. A **65**, 043613 (2002).

[151] Y. Castin, "Les Houches summer school 2000" lecture notes: "Bose-Einstein condensates in atomic gases: simple theoretical results".

[152] E. L. Bolda, E. Tiesinga, and P. S. Julienne, Phys. Rev. A **66**, 013403 (2002).

Acknowledgements

First and foremost I would like to thank my thesis supervisor Ignacio Cirac for the guidance and support he has provided throughout the course of this work. I am especially grateful for many inspiring and instructive discussions that have widened my fundamental understanding of physics.

I am deeply thankful to Belén Paredes, Frank Verstraete, Juan José García-Ripoll, Karl Gerd Vollbrecht and Miguel Angel Martín-Delgado for their fruitful and constructive collaboration on important parts of this thesis.

I also thank Michael Wolf, Barbara Kraus and Géza Giedke for their valuable advice concerning questions in quantum information theory.

My regards extend to all my colleagues and friends at the Max-Planck Institute, especially to Henning Christ, Christian Schön, Oliver Buerschaper, Klemens Hammerer, Toby Cubitt, Tassilo Keilmann, Norbert Schuch, Valentin Murg and Enrique Solano, for their support and many stimulating discussions about physics and other subjects.

Finally, I wish to thank my wife Michaela and my family for the encouragement and love I have received throughout my time at the MPQ.

I gratefully acknowledge funding by the Max-Planck Society and the ”Kompetenznetzwerk Quanteninformationsverarbeitung der Bayerischen Staatsregierung”.